THE UNIVERSITY *of* EDINBURGH

Imaging intra-cellular wear debris with coherent anti-Stokes Raman scattering spectroscopy

Martin Lee

A thesis submitted for the degree of Doctor of Philosophy

The University of Edinburgh

2013

Declaration of Authorship

I, Martin Lee, declare that this thesis has been completed by me and consists of work entirely of my own undertaking. When I have consulted the published works of others, it is clearly attributed. This work has not been submitted for any other degree or professional qualification.

Signed: _____

Date: _____

Table of Contents

Figures

Acknowledgements

I am indebted to the friendship and aid of many people over the course of my studies and would like to thank all of those that I have crossed paths with during my time in Edinburgh.

I would like to say thank you to Dr. Alistair Elfick for giving me this opportunity, as well as guidance throughout this longest of journeys. Thank you to my colleagues, past and present, in the Elfick group: Andy, Alan, Bryony, Rabah, Ruby, Grigore, Christian, Alastair, Vlastimil, Meropi and Kim. Finally, thank you to all those who have contributed their specialist knowledge, expertise and time, especially: Dr Andy Downes, Dr Rabah Mouras, Dr Jochen Arlt, Mr Stephen Mitchell, Mr Greg Anderson, Professor Ian Dransfield and all the staff at QMRI.

Finally I would like to say a special thank you for the love and support of my family, Mum, Dad, Jennifer, David and William and most of all to Jovana.

Abstract

Aseptic loosening of artificial joints is caused by an osteolytic reaction to wear debris mediated by macrophages and other cells. Imaging these wear particles within cells can be a key process in understanding particle-cell interactions. However, the compounds used in surgical implants are not easily visualised as no tagging molecule can be added without altering the properties of the material. We were interested in using a label free optical technique known as coherent anti-Stokes Raman scattering spectroscopy (CARS) to image these particles in cells.

In this thesis we studied how to use CARS to image physiologically relevant wear particles within cells. We characterised the responses from our CARS system and found them to be in good agreement to the Raman spectra we obtained for the same materials. We showed that the forward scattered CARS signal was consistently larger than the backwards scattered signal for the same size particles, and also generated a larger contrast, especially between sub-micron sized particles and the non-resonant background.

Wear particles of polyethylene isolated from a pin-on-plate wear simulator were shown to be in a similar size range to those retrieved from revision tissue. When incubated in our model macrophage cells we were able to image areas of CARS signal that indicated the location of these particles in the cell. Furthermore, using multiple CARS images taken at different Raman resonances we were able to distinguish between three different polymeric compounds added to cells, showing the specificity of the technique. The inherent 3D sectioning capabilities of multiphoton microscopy were used to generate projected images of the cells and contents, as well as estimating the particle loads within cells.

These results show that CARS could be an important tool in imaging intra-cellular polyethylene and characterising the interactions of wear particles with cells and the surrounding tissue.

Abbreviations

BSA	bovine serum albumin
CARS	coherent anti-Stokes Raman scattering spectroscopy
DM	dichroic mirror
DMEM	Dulbecco's modified Eagle's medium
DPPC	1,2-dipalmitoylphosphatidylcholine
E-CARS	backwards scattered CARS
ECD	equivalent circular diameter
F-CARS	forward scattered CARS
FBS	foetal calf serum/foetal bovine serum
FDTD	finite difference time domain
FEG-SEM	field emission gun scanning electron microscopy
FWHM	full width at half maximum
GM-CSF	granulocyte macrophage colony-stimulating factor
HEK 293	human embryonic kidney cell line
HL-60	human promyelocytic leukemia cell line
HuH7	hepato cellular carcinoma cells
IgG	immunoglobulin G
IL-1a	interleukin 1a
IMEM	Iscove's modified Eagle's medium
MCF-7	human breast adenocarcinoma cell line
M-CSF	macrophage colony-stimulating factor
MDA 231	human breast adenocarcinoma cell line
MSC	mesenchymal stem cell

NA	numerical aperture
Nd:YVO4	neodymium doped yttrium vanadate orthovanadate
NIH 3T3	mouse embryonic fibroblast cells
OPO	optical parametric oscillator
PBS	phosphate buffered saline
PE	Polyethylene
PGE2	prostaglandin E2
PMMA	polymethylmethacrylate
PMT	photomultiplier tube
PTFE	polytetrafluorethylene
RANK	receptor activator of nuclear factor kappa-B
RANKL	receptor activator of nuclear factor kappa-B ligand
RAW 264.7	mouse leukaemic monocyte macrophage cell line
RPMI 1640	Roswell Park Memorial Institute 1640 medium
SEM	scanning electron microscopy
SHG	second harmonic generation
SRS	stimulated Raman scattering
TEM	transmission electron microscopy
TNF-α	tumour necrosis factor-alpha
TPA	phorbol 12-myristate 13-acetate
TPEF	Two photon excited fluorescence
UHMWPE	ultra high molecular weight polyethylene

1 Introduction

Total hip arthoplasty is a surgical intervention providing a long-term solution for worn or damaged hip joints which can cause severe pain and loss of mobility. At least 70,000 hip procedures are carried out annually in the UK. Although the typical hip replacement often outlives its intended use, many patients require revision surgery when an existing hip replacement has become worn or the supporting tissues have become weakened.

A leading requirement for revision surgery is due to aseptic loosening around the implant. It is currently thought that wear debris generated from the motion of the articulating joint enters the periprosthetic space where it is phagocytosed by macrophages. These macrophages then release pro-inflammatory cytokines and other mediators of osteolysis, leading to the eventual loosening of the implant.

Previous examination of post-operative tissue has been limited by the inertness of the materials involved. Characterisation of the wear debris from retrieved tissue usually involves liquefaction of the tissue and analysing the remaining portion of wear debris by SEM. Immunohistochemical staining of ultrathin sections of tissue reveals information about the type of cells and the presence of pro-inflammatory cytokines but is unable to identify much of the wear debris involved.

Multiphoton microscopy techniques such two-photon excitation fluorescence (TPEF), second harmonic generation (SHG) and coherent anti-Stokes Raman scattering (CARS) spectroscopy provide new ways imaging cells and tissue in three-dimensions. These techniques are capable of imaging cells and tissues without the use of added chemical labels, relying on the endogenous structural and chemical properties of molecules in the cell. The use of near infrared light also allows for deeper tissue imaging than more conventional techniques as higher wavelength photons exhibit less scattering in tissue. Achievable signals from depths of up to 0.5mm being reported.[1]

This thesis explores how CARS microscopy can be used to study particles within cells. The CARS setup used in this thesis was custom designed at The University of Edinburgh and as such its functionality was largely unknown. We characterised our

CARS system and assessed its suitability in studying physiologically relevant wear particles.

Key objectives that are explored in this thesis are:

1. The use of Raman spectroscopy to record spectra of a variety of biological samples as well as materials used in prosthetic hips. This will help identify vibrational resonances that are present in these samples and could be a target for imaging with our CARS system. Raman mapping will also be used as a label free imaging technique to compare with CARS microscopy.
2. Characterisation of wear debris from a pin-on-plate wear simulator will show that the wear particles produced are in the same physiological size range as particles retrieved from wear tissue.
3. We will validate our CARS system showing that images produced are a result of four-wave mixing and that there is a vibrational enhancement of this process at Raman resonances.
4. Model particles will be used to assess the abilities of our CARS system to image micron and sub micron sized particles. The effects of the detection geometry will also be examined to show the differences between forward or backwards scattered CARS signals.
5. We will identify a suitable cell system that is both phagocytic and easy to manipulate to act as a model system to image particles within.
6. We will image physiologically relevant particles within cells using CARS microscopy and use the inherent optical sectioning properties to show the particle location in 3D.

2 Literature review

2.1 The hip joint

The coxofemoral joint, (see Figure 1) or hip joint is a ball and joint socket consisting of the concave acetabulum of the os coxae bone (pelvis) as the socket to the spherical head of the femur (thigh bone).

Figure 1 Radiograph of the coxofemoral joint. (Wikipedia)[*]

The head of the femur is a ball like surface, covered in hyaline cartilage that articulates against a horseshoe shaped area of the acetabulum called the lunate surface that is also covered in cartilage. The joint itself is deepened by the presence of the acetabular labrum, a ring of cartilaginous material that helps to stabilise the joint, and provides a seal to enhance the lubrication of the joint.[2] The head of the femur is attached by a ligament at the fovea, a small pit on the head of the femur. This is attached to the acetabulum notch, a deep notch found at the base of the lunate surface. This connection is not thought to play a significant role in stabilising the joint,[3] especially when compared to the hip joint capsule, a dense fibrous structure attaching the femoral head and neck to the periphery of the acetabulum. The hip joint capsule is made up of three ligaments: the iliofemoral and pubofemoral anterior ligaments, and the ischiofemoral posterior ligament (see Figure 2). These ligaments constrain the range of motion of the joint preventing hyperextension and subsequent dislocation of the joint.[4,5]

[*] http://en.wikipedia.org/wiki/File:Hueftgelenk-gesund.jpg

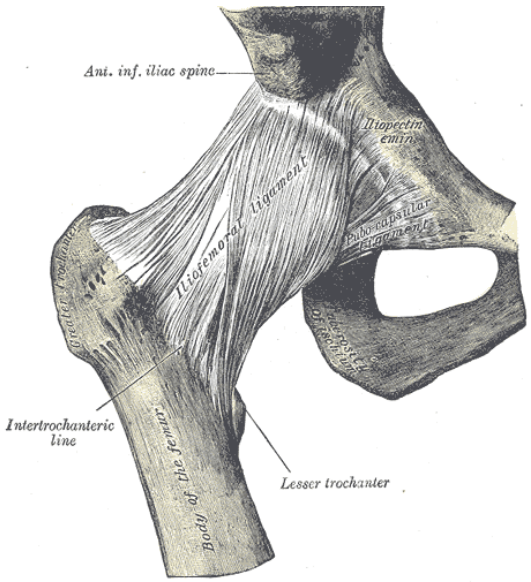

Figure 2 Diagram of the major ligaments of the hip joint which help hold the hip joint together. (Gray's Anatomy)[†]

The hip joint is a major load bearing joint in the human body. Whilst walking, the load through the hip joint can be more than five times body weight, and much larger still for athletic activities such as running.[6]

2.1.1 Disease and damage

Due to the constant high load through the hip joint, it is particularly susceptible to wear and tear and failure of weakened components. The more common aetiologies are discussed.

2.1.1.1 Osteoarthritis

Osteoarthritis presents itself clinically as pain and discomfort in the joints, often preventing full range of motion. In the UK almost 5% of the population over 60 years of age is affected severely enough to require surgical intervention.[7] A number of risk factors including genetic predisposition, obesity, joint misalignment, trauma and immobilization are thought to lead to cartilage breakdown.[8] As the cartilage is degraded, the bone surfaces can be exposed and damaged, causing pain and inflammation, leading to decreased movement of the joint and muscle atrophy. Although a number of promising treatments are in development, a major problem is

[†] Reproduced from Gray's Anatomy 1912

that the disease is often asymptomatic for decades, at which point the joint is already damaged and no existing treatment aside from total arthroplasty is effective.[8] Currently, osteoarthritis is the causative diagnosis leading to hip replacement in over 93% of all hip replacement operations in the UK.[9,10]

2.1.1.2 Fracture

Hip fractures are typically associated with the elderly with the lifetime risk to women over 50 as high as 15%. The cost to treat hip fractures in the UK alone is estimated at around two billion pounds.[11] Hip fractures, due to their debilitating nature, often require extended hospital based treatment and further health and social care once patients are released from hospital.[12] There is also a higher rate of morbidity associated with hip fractures in the population.[13] The number of people suffering such a fate is expected to increase as the demographics of populations change to encompass more elderly people. Fractures typically occur in weaker spots in the bone, particularly around the femoral neck. Bone density loss due to aging is thought to play a role in the heightened risk,[14] but the key injury factor is usually some kind of trauma, an accidental stumble or fall, for example.[15] Overall, fractures are only responsible for a small number of the total number of primary joint replacements.[9,10]

2.1.2 Total hip arthroplasty

Total hip arthoplasty is one of the most successful surgical interventions developed, providing long term pain relief coupled with a joint survivorship of more than 80% at 20 years post surgery.[16] It can be used to treat a wide variety of diseases and trauma including, but not limited to: osteoarthritis, rheumatoid arthritis, developmental dysplasia, osteonecrosis, acute fracture, non-union of a fracture and post traumatic degenerative disease. Artificial joint replacement has advanced considerably since the use of ivory components by Gluck in the 19th century[17] with most modern hip replacements based on the work of the late Sir John Charnley who pioneered many of the surgical techniques, designs and materials currently used in modern hip replacements.[18]

A replacement joint usually consists of a femoral component, a stem and head made of metal, (stainless steel, cobalt-chromium or titanium alloys are popular choices) articulating against a polymeric acetabulum component (see Figure 3). The

acetabular cup is usually made from ultra high molecular weight polyethylene (UHMWPE) to help maintain durability, although ceramics or metallic components can sometimes be used. The components are held in place by polymethylmethacrylate (PMMA), a bone cement, although uncemented hip replacements are also performed.

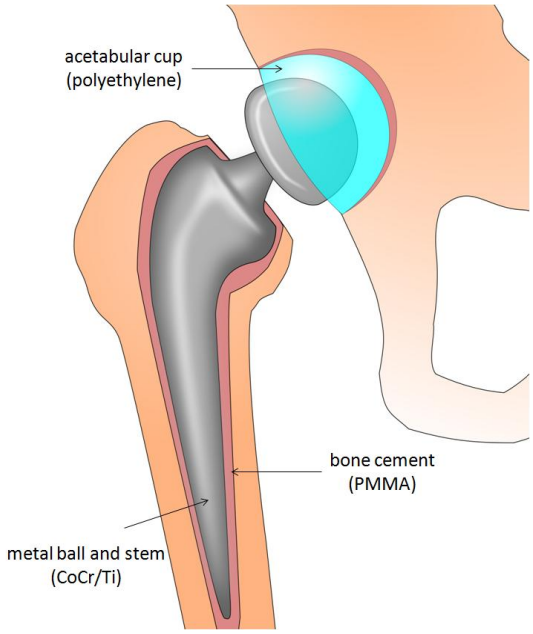

Figure 3 Diagram of an artificial joint.

However, as total hip replacements are performed on increasingly younger patients the rate of joint survival decreases greatly. Patients younger than 50 years can expect to achieve only an 80% rate of joint survival after 10 years regardless of fixation technique and bearing combination.[19] This has led to a resurgence of interest in alternative bearings and implant techniques, the most noticeable of these have been using cementless fixations with porous coated stems to allow bone ingrowths with early follow-up studies showing good results.[20,21] Other studies into alternative articulations, metal-on-metal and ceramic-on-ceramic and cross-linked polyethylene have sometimes demonstrated lower *in vivo* wear rates than conventional metal-on-polyethylene replacements though continued follow-up is required to demonstrate the individual benefits and risks associated with each fixture.[19] A recent report published in The Lancet has suggested that high failure rates occur more commonly in metal on metal implants, with metal on polyethylene associated with the lowest risk of

revision.[22] Metal on polyethylene remains the most commonly used materials in hip implants in the United Kingdom.[23]

2.1.3 Hip replacements and revision

In England and Wales, a reported 76,759 hip replacements were carried out in 2010,[10] whilst in the United States, where there is no national registry, the number is thought to be over 200,000.[24] Although many hip replacements will outlast their recipients, the number of hip revision procedures (a procedure where part or the entire existing artificial hip is replaced) has been growing annually. In England and Wales 7,852 revision procedures were carried out in 2010[10] whilst in the United States the number is thought to be around 36,000.[24] This places a considerable toll on the health services.

Only a small proportion of artificial joints that fail do so because of a direct component failure. These are often documented in case review papers as they may indicate a flaw in the product itself which should be closely scrutinised. Failure of the femoral head[25] or neck[26] can occur through poor design or material choice which leads to fatigue fractures. Examining these failures has helped to improve design and material choice and now component failure is found to be the cause of less than 2% of all hip revisions, and many of these may still be due to incorrect installation rather than a direct failure of the device.[10]

Infection of the implant during or after surgery is a serious problem and is estimated to be responsible for around 13 to 14% of all revision operations, and the majority of two-stage revisions (revisions in which both parts of the artificial joint are replaced).[10,24] Infection is thought to occur in approximately 1 in every 300 operations. The implant surface itself can be colonised by the bacteria, where it forms a biofilm to protect itself against the host's immune system and administered antibiotics. If an infection advances to this stage, it can only be cleared by removal of the implant.[27]

Surgical technique plays a large role in the survivability of the implant and the rate of revision has improved considerably since the adoption of techniques such as careful cleaning of the bone bed, compression and vacuum-mixing of the cement to improve its strength.[28] Any implant that is installed misaligned may also need to be revised

due to instability in the joint. 6% of the joint revision surgeries in the UK were due to misalignment whilst a small number revisions (<1%) were due to the incorrect head or socket being fitted.[10]

The most common cause for requiring revision surgery is aseptic loosening, which is listed as the cause of revision surgery in 45% of revisions of the UK, although lysis (14% of all revisions) is a more localised form and shares the same aetiology.[10] Aseptic loosening is caused by an immune reaction to the implant material, leading to the eventual loosening of the implant and is the main cause of revision surgery of long lasting implants. Aseptic loosening was the cause of only 18% of revisions at less than 2 years but was involved in over 90% of revisions where the artificial joint was 10 years old or older.[29]

2.2 The causes of aseptic loosening

The need to choose a biocompatible material, capable of withstanding the stresses of weight bearing was clear from the outset of hip replacement design. The late 1800s and early 1900s saw experiments with many different materials in an attempt to identify a hard wearing and biologically inert material.[30] The early work of John Charnley, the father of modern hip design, floundered with the choice of polytetrafluorethylene (PTFE) as a synthetic articular cartilage. The PTFE underwent both excessive wear within two years (in contrast to laboratory predictions[31]) as well as the generation of wear particles that induced intense foreign body reactions.[32] The move to UHWMPE, a hard wearing and biologically inert material helped to usher in the modern era of hip replacement design, a material that is still used almost 6 decades later.[33]

Aseptic loosening is typically characterised as bone resorption without infection that leads to the loosening of the implant. It is currently the main indication of hip revision surgery for implants older than 10 years.[29] The causes of aseptic loosening may in fact be multi-factorial, with many different elements from genetics, to mechanical wear being involved to some degree.[34] But most reviews highlight the importance of osteolysis, with wear debris as a major contributing factor to the problem.[34-39]

Osteolysis is the loss of bone material, and may occur in general around the implant, or localised in particular areas. Bone growth, and bone destruction is mediated by osteoblasts and osteoclasts respectively. Osteoclasts can be formed from macrophage cells as well as other cells from the monocyte lineage. Osteoclast formation is thought to be caused by the release of soluble factors including receptor activator of nuclear κ beta ligand (RANKL) in conjunction with other factors such as macrophage colony stimulating factor (M-CSF), interleukin 1 α (IL-1α) and tumour necrosis factor α (TNF-α).[40,41] Osteoblasts express RANKL and TNF-α that stimulate osteoclast formation, whilst osteoclasts are thought to recruit osteoblasts though sphingosine 1-phosphate and other chemokines.[42] In normal conditions, bone that is resorbed by osteoclasts, is in turn replaced by osteoblasts in a finely controlled fashion. Upsetting this balance can lead to an increase in bone resorption.

Implant material, including the polyethylene liner, undergoes many repeated articulation cycles over its life-span,[43] this causes small particles to be worn away from the surfaces. These particles have been retrieved from tissues (see chapter 2.3 for more details) around the prosthetic joint but can also be found more widely disseminated in other areas of the body.[44] It has been demonstrated *in vitro* that adding wear particles to cultures of macrophages can induce the release of a number of pro-inflammatory, and pro-osteolytic cytokines[45] including: TNF-α, IL-1α, IL-6, granulocyte macrophage colony-stimulating factor (GM-CSF) and prostaglandin E2, (PGE2).[36,38,46-53] Phagocytosis of particles has also been shown to trigger bone resorption in macrophages.[54] *In vivo* assays have demonstrated that UHMWPE particles increase RANK, RANKL,[55] IL-1α and TNF-α expression,[56,57] as well as tartrate-resistant acid phosphatise staining (a marker for osteoclasts).[57] This upset of the normal balance of cellular signalling is thought to lead to increased osteoclast recruitment and localised osteolysis near the joint.[35]

2.3 Wear particles, retrieval and analysis

2.3.1 Imaging in tissues

The exact nature and location of wear particles generated from prosthetic joints has long been a topic of study, hampered by the difficulty in identifying polyethylene particles within tissues due to the lack of specificity in adding tag molecules to aid

identification. Histological examination of retrieved revision tissue allows for the gross examination of affected tissues by both normal and polarised light microscopy. Polyethylene particles show a bright birefringence under polarised light, which serves as one method for their examination in tissue.[58] Lee *et al*. [59] used polarised light and an apparent magnification of 320× to investigate the size of polyethylene particles in failed, non-infected, cemented, total hip replacements. They showed a mean size of polyethylene debris to be 2-4 μm in the short dimension and 8-13 μm in the long dimension. Pazzaglia *et al*.,[60] reported that in aseptically loosened cemented hip revisions polyethylene particles were never less than 3 μm with the smallest particles phagocytosed by mononuclear cells but larger particles were engulfed by multinucleated giant cells or surrounded by a fibrous tissue capsule. They noted that small polyethylene particles did not exhibit any definite relation with the cytoplasmic membrane. Bos[61] studied 128 revisions performed after an implant duration of between three months and 19.5 years as well as 40 autopsy specimens. Polyethylene particles were found to vary in diameter from 0.5 μm to more than 1 mm with those of over 30 μm surrounded by multinucleated giant cells. Wear debris was visible in revision samples where the implant was only 3 months old. Bos also noted that polyethylene wear appeared to be concentrated in the interface membranes of the acetabulum, with even distributions in all other localizations examined. Marowietz *et al*., [62] looked at revision samples from 370 total joint arthoplasties (218 hip, 56 knee and 96 with no location attached). They found that polyethylene particles exceeding an area of 5 μm^2 were frequently found in multinucleated giant cells with smaller polyethylene particles of around 2 μm^2 found in macrophages. Larger particles of up to several mm were inferred by void spaces due to their removal during the sectioning of tissue into slices thin enough to examine with light microscopy.

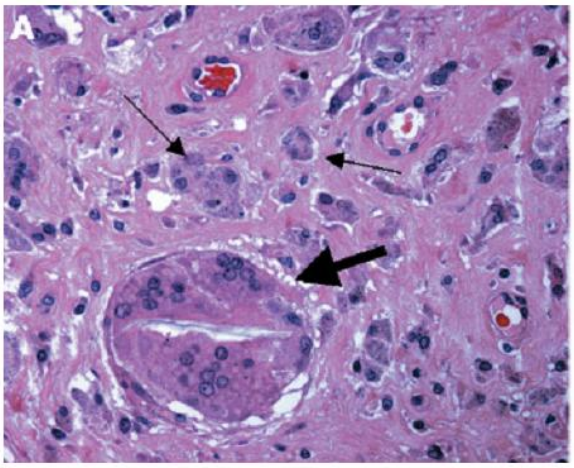

Figure 4 Light microscope image of a haematoxylin and eosin (H&E) stained section of revision tissue. Broad arrow shows a multinucleated giant cell containing large polyethylene particle found together with macrophages (small arrow). Original magnification: 400×. Adapted from a figure in reference 62.

Oil red is a potential stain for polyethylene as well as polymethylmethacrylate[58] but has also seen use as a lipid stain.[63] Hansen *et al*.,[58] examined revision tissue from 9 samples of failed uncemented total hip replacements. They found that due to the non-specificity of the oil red staining it was unclear whether staining of parts of the cell were due to small polyethylene particles or just lipids. However, when examined by transmission electron microscopy (TEM) it was found that many cells contained membrane bound vesicles containing heteromorphous particles. Urban *et al*,.[44] similarly used oil red to identify polyethylene particles in the lymph nodes of post mortem samples from cadavers with total joint replacement. Polarised light revealed particles varying in size from 1 μm to 30 μm with the use of thermal analysis and a Fourier transform infrared microprobe spectrometer confirming that their characteristics were consistent with those of polyethylene. Oil red staining was consistent with polarised light detection but staining was also present in control samples, suggesting that other long-chain hydrocarbons could be responsible.

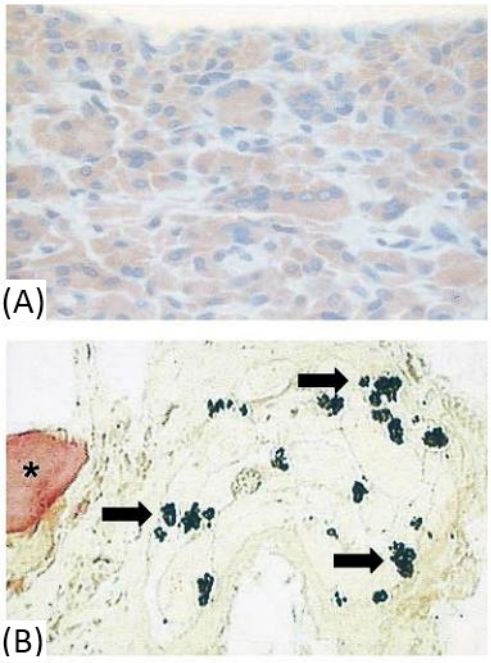

Figure 5 Light microscope images from revision tissue stained with oil red. A. Serial section of the tissue stained with H&E showing numerous oil red positive cells. Magnification 400×. B. Mulberry-like tissue area containing a few black particles that are not stained with oil red, whereas large extracellular PE debris (marked by asterisk) are strongly stained by oil red. Original magnification: 300×. Adapted from a figure in reference 58.

It is clear from the variety of sizes and distributions of particles found that light microscopy may not be the ideal method to accurately image particles within cells due to the subjective nature of particle identification. In particular smaller particles, such as those less than 0.5 μm appear to be difficult to resolve with any accuracy as they are close to the diffraction limit of an optical microscope. The inability to specifically stain polyethylene may also lead to other particles (such as those from bone cement) being misidentified as polyethylene.

TEM has also been used on clinical specimens to help provide much greater magnification levels than light microscopy.[59] This is often carried out in addition to secondary detection methods such as x-ray analysis to help confirm the particle's nature. This is most useful when examining electron dense materials such as metals. Polyethylene fibres with their low atomic numbers give rise to a poor back scattered electron signal in SEM and appear as electron transparent areas in TEM.[60] Hansen *et al.*,[58] observed membrane bound vesicles that varied in size containing

heteromorphous particles occasionally showing lamellar patterns. They attributed these particles to submicron polyethylene particles. Zaloudek *et al*.,[64] similarly observed many birefringent particles when viewed under polarised light from 5-10 μm in length down to the limit of microscopic resolution. Under electron microscopy the histiocytes were shown to contain innumerable cytoplasmic membrane bounded inclusions filled with lamellated dark-staining materials. These were interpreted as lysosomes containing phagocytosed fragments of polyethylene, as well as larger angular or needle like inclusions.

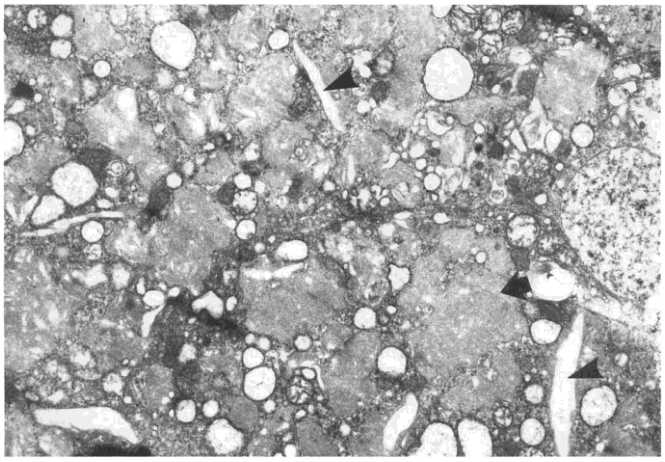

Figure 6 Histiocytes studied by electron microscopy, showing numerous membrane bounded cytoplasmic inclusions compatible with lysosomes (arrow). These had a lamellar internal structure and contained numerous needle like inclusions of variable size (arrowheads). The lysosomal contents most likely represent phagocytosed polyethylene. Original magnification: 12,000× magnification. Adapted from a figure in reference 64.

TEM offers a far superior level of spatial resolution to light microscopy, however, positive identification of particles as polyethylene is still a challenge as there is no specific staining of the particles. Sample preparation techniques such as dehydration, sectioning and staining can all alter the location of particles within the cells.

2.3.2 Wear retrieval

Retrieval of wear debris from revision tissue offers another method of examining the volume, size and morphology of wear particles produced from *in vivo* wear. Methods of extraction from tissue typically involve chloroform/methanol lipid extraction followed by whole tissue dissolution in sodium hydroxide[65] or potassium hydroxide.[66,67] Particles can then be isolated using ultracentrifugation through layers

of known densities or gradients and then filtered through polycarbonate membranes for further analysis.[65,67,68] Visentin *et al*.,[69] used a different technique designed to minimise the loss of any debris. Sections of removed tissue were placed on to a polycarbonate membrane and then the tissue was dissolved with sodium hypo chlorite before flushing through with previously filtered water.

Separating the particles allows for chemical characterisation of the recovered wear debris. Energy dispersive X-ray analysis helps to eliminate non-polyethylene particles, but polyethylene itself cannot be positively identified in this fashion.[67,68] Micro-Raman spectroscopy and Fourier transformed infrared spectra allow for more detailed chemical characterisation and positive identification of the polyethylene particles.[44,68,69]

Analysing the size and distributions of retrieved wear particles can be achieved in a number of ways. One approach is to use SEM to visualise particles on a polycarbonate membrane.[67-71] Using field emission gun-scanning electron microscopy (FEG-SEM) allows characterisation of particles down to a few tens of nanometres. Although detailed characterisation of area, perimeter and aspect ratio are possible, any measurement of volume will be an estimation.[67,69] Low angle laser light scattering allows for an entire sample to be measured non-destructively and avoids any artefacts associated with filtering, drying and agglomeration of debris but is not able to give a detailed morphological look at each particle.[72]

Retrieval studies of polyethylene from periprosthetic tissue have demonstrated that the majority of wear particles found are under 0.5 μm in size, with many particles found in the nanometre size domain.[65,67,73] Figure 7 shows an example result from Zolotarevova et al., who studied four patients using a number of different centrifugation speeds. Particle size was assessed using SEM and the purity, the contamination from other retrieved particles, was measured using IR spectra.

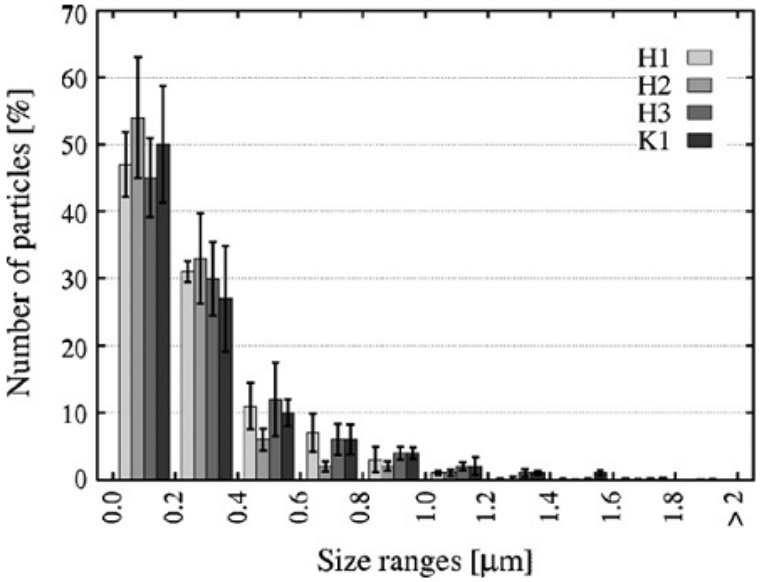

Figure 7 Particle size distributions for four studied patients. Error bars are calculated as estimated standard deviations of the corresponding average. Adapted from a figure in reference 73.

Particle size has been shown to play a significant role in the response elicited from cells. It has been reported that particles over 10 µm in size elicit less severe responses than those under 10 µm, and that those under 1 µm generate the greatest response in *in vitro* studies.[52,74,75] It has also been reported that particles of smaller sizes 0.15 and 0.21 µm either generated more benign or non-significant responses[75,76] although other reports have disagreed with this, possibly due to the different particle sources and cells used.[77] The shape of the particle has also been suggested as a factor for different cellular responses.[76,78,79] This should be an important consideration given the multitude of differences in particle shapes found *in vivo,*[65,67] simulated wear debris and in commercial powder preperations.[80]

2.4 Raman spectroscopy

Raman spectroscopy relies on the inelastic scattering of light from molecules to gather information about the chemical bonds in the sample. When light interacts with a molecule it can be scattered either elastically, as shown in Figure 8 A, or it can be scattered inelastically - where some energy is gained or lost in the process, as shown in Figure 8 B and C.

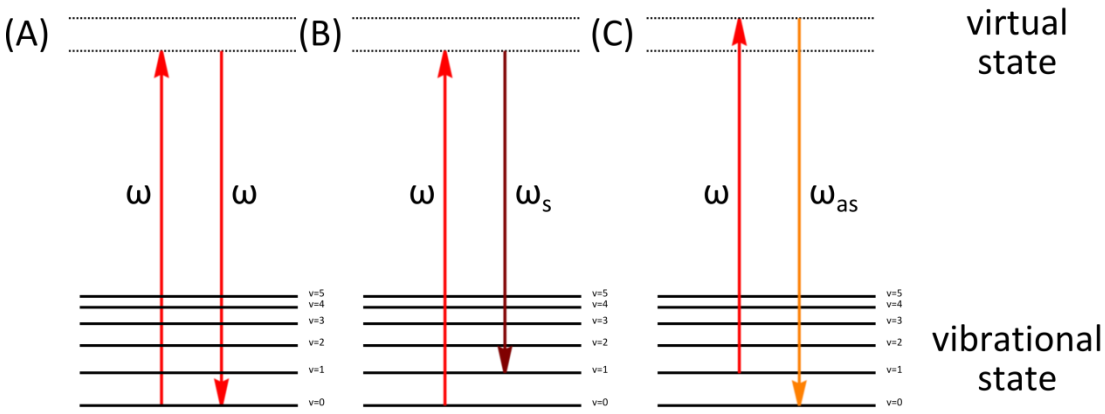

Figure 8 Energy diagrams of light scattering A. Elastic scattering B. Inelastic scattering with a Stokes shift. C. Inelastic scattering with an anti-Stokes shift.

Every bond has a set of vibrations with different energy levels associated with it. These depend on the atoms involved, as well as the environment in which they are found in. Figure 9 shows the fundamental vibrations that occur in a CH_2 group which include: stretching, wagging, rocking, twisting and scissoring, each of which have their own associated energy levels. When a photon is inelastically scattered, some of this energy is transferred into increasing a vibrational energy level in the molecule.

A Raman spectrum of a molecule can be taken by shining a monochromatic laser source at the sample and then measuring the energies of the scattered photons to provide a spectrum. Each of these vibrations shows as a peak in the spectrum, although sometimes there is an overlap and mixing which may broaden or hide some peaks. As each set of vibrations are unique to not just the bond and the atoms involved, but also to the environment they find themselves in, it is possible to identify many compounds from a generated Raman spectrum.

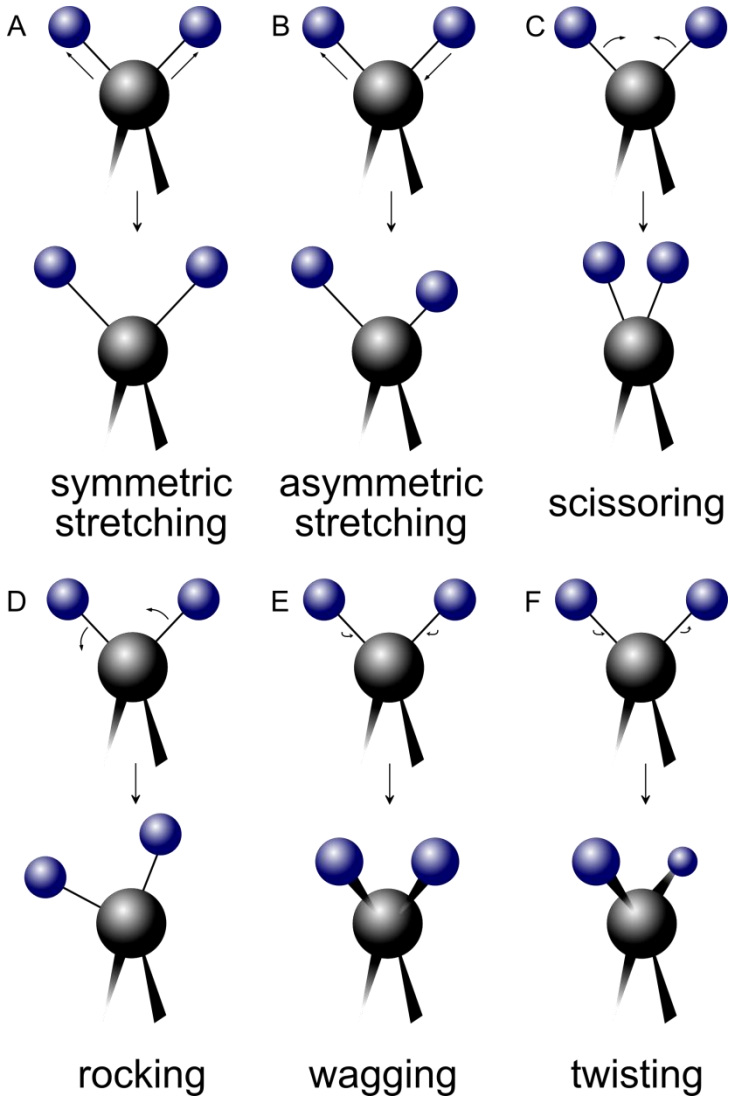

Figure 9 Raman active vibrations of a CH_2 group. A-D show the in plane stretching modes whilst E and F show the out of plane stretches.

As Raman spectroscopy depends on light, and the chemical bonds in the substance, it is said to be a label-free technique as no exogenous tag molecule is required to generate a signal for the Raman spectra. Light is also is able to penetrate cells and tissues which means that very little sample processing is necessary to prepare a sample for Raman spectroscopy.

Standard Raman spectroscopy takes a single spectrum from a sample which provides chemical information, but no spatial information from the sample (see Figure 18 for an example spectrum). Confocal Raman aims to generate this spatial information using confocal detection of the Raman active photons to build an image of the cell.

Confocal Raman (using a pinhole to remove out of focus scattered light) has been used to study the storage and degradation of lipids within macrophages,[81] lipid bodies associated with latex bead containing phagosomes,[82] as well the delivery and degradation of polymeric micro and nanoparticles.[83,84]

The drawback with Raman is that for biological samples, it can take upwards of 5 minutes to obtain usable data. Only a small proportion of scattering photons are involved in a Raman active collision, requiring slow scan rates. Confocal Raman systems can need up to 1 s or longer pixel dwell time to generate enough data for an image[83] which usually leads to low resolution images as well as the use of fixatives to prevent the sample from moving.

2.5 Multiphoton spectroscopy – two photon excited fluorescence and second harmonic generation

Multiphoton imaging is emerging as a new tool for viewing biological processes.[85] Two photon excited fluorescence (TPEF) is the most widely used multiphoton technique with many advantages over standard confocal fluorescence. Two lower energy photons are absorbed near simultaneously to produce the same effect as a single photon of higher energy. The use of lower energy, longer wavelength photons allows for better depth penetration than standard fluorescence as the degree of light scattering is inversely proportional to the fourth power of the light wavelength. Only where the excitation beam is tightly focused are the conditions optimal for the two photon absorption. Two photon excitation helps in a number of different ways: reducing background fluorescence, photobleaching and photodamage, as well as providing sub micrometer resolution with excellent three-dimensional sectioning. A limitation of TPEF is its reliance on an endogenous or introduced fluorophore to generate contrast, something which is not always available.

Many biological materials are ordered, polarisable, noncentrosymmetric structures which allows them to generate second harmonic light. This second harmonic generation (SHG) differs from TPEF in that it does not involve an excited state but a coherent hyper Rayleigh scattering. No energy is lost and the generated light is exactly twice the energy of the incident photons. As a result of this, there is no

photobleaching effect as there are no excited states to depopulate. SHG's nonlinear nature allows it to share TPEF's optical sectioning capabilities. Protein arrays such as collagen, actomyosin and tubulin all exhibit observable SHG signals giving information about the sub-micrometer and micrometer scale assemblies.[86]

2.6 Optical Resolution

The ability of a microscope to separate small objects is often known as the resolving power or angular resolution. It is usually defined through the Rayleigh criterion, which states that two objects of the same intensity should be considered resolved when the first maxima of one object coincides with the first minimum of the other. [87] It is dependent on a number factors but its absolute limit is governed by the wavelength of the light used in the system. German physicist Ernst Abbe calculated that the smallest spot that light can be focused into is calculated by:[88]

$$d = \frac{\lambda}{2(n \sin \theta)}$$

Where d is the diameter, λ the wavelength of light, and *n* is the refractive index. *n* sin Θ is often referred to as the numerical aperture (NA).

This gives us a means of calculating where the first minima of the resulting diffraction pattern will occur: [87]

$$r_0 = \frac{0.61 \times \lambda}{NA}$$

$$z_0 = \frac{2 \times n \times \lambda}{(NA)^2}$$

Where r_0 and z_0 are the lateral and axial limits respectively and give the theoretical limit for a system. For simplicity, the full-widith-at-half-maximum (FWHM) is used as an approximation for these factors instead to determine the resolution of a system.

2.7 Multiphoton microscopy - CARS spectroscopy

2.7.1 Theory and simulation

Coherent anti-Stokes Raman scattering spectroscopy (CARS) is a type of multiphoton microscopy that relies on a four wave mixing process. This 3rd order non-linear optical process involves the interaction of three photons to produce a fourth at the anti-Stokes frequency.

Incident laser beams at frequencies designated ω_p and ω_s (pump and Stokes) interact through the third-order nonlinear susceptibility tensor ($\chi^{(3)}$) to generate a polarization component which produces coherent radiation at frequency $2\omega_p$-ω_s, (ω_{CARS} or ω_{as}) (see Figure 11). The coherent nature allows molecules to constructively interfere with each other when generating CARS signals, creating a much larger signal than standard Raman spectroscopy. This process requires that the incident laser beams are properly phase matched.

Several different beam geometries are able to resolve the conditions to allow the correct phase matching (a condition where the amplitude contributions from the different sources are all in phase) to occur and more common examples are shown in Figure 10.

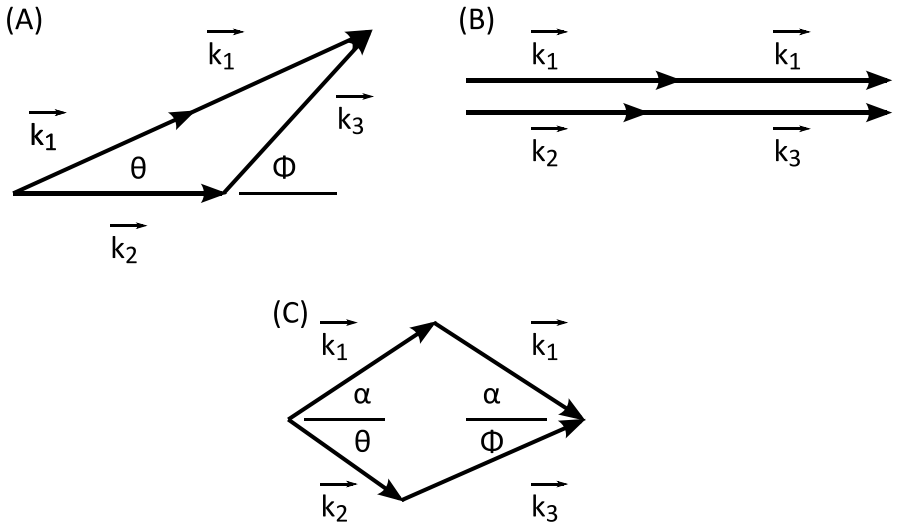

Figure 10 Some CARS phase matching approaches. A. General. B. Collinear. C. Crossed beam or BOXCARS. Adapted from a similar figure in reference 89.

For CARS microscopy the use of a lens with a high numerical aperture allows a tight focusing of the beams, relaxing the phase matching conditions. This is due to the large cone of wave vectors and short interaction length. The small excited volume at the laser foci also leads to efficient background signal rejection.[90]

If the phase matching conditions are met, the CARS intensity is a squared modulus of the induced non-linear polarization:[91]

$$P^{(3)} = \chi^{(3)} E_p^2 E_s$$

where E_p^2 is the combined pump field $E_p(\omega_p)$ and probe field $E'_p(\omega'_p)$, E_s is the Stokes field and $\chi^{(3)}$ is the third order susceptibility tensor.[92] The third order susceptibility tensor, $\chi^{(3)}$, can be given as a generalised expression:[91]

$$\chi^{(3)} = \frac{A_R}{\Omega - (\omega_p - \omega_s) - i\Gamma_R} + \eta_{NR}^{(3)} + \frac{A_t}{\omega_t - 2\omega_p - i\Gamma_t}$$

where Ω is the resonant Raman vibrational frequency, A_R and $i\Gamma_R$ are the strengths and the dampening factors (Raman scattering cross-section and half width at half maximum) respectively, of the vibrationally resonant contribution (Figure 11 A). $\eta_{NR}^{(3)}$ represents the non-resonant contribution (Figure 11 B). ω_t is the frequency of the two photon electronic transition where A_t and $i\Gamma_t$ are the strengths and dampening factors respectively (Figure 11 C).[91-93]

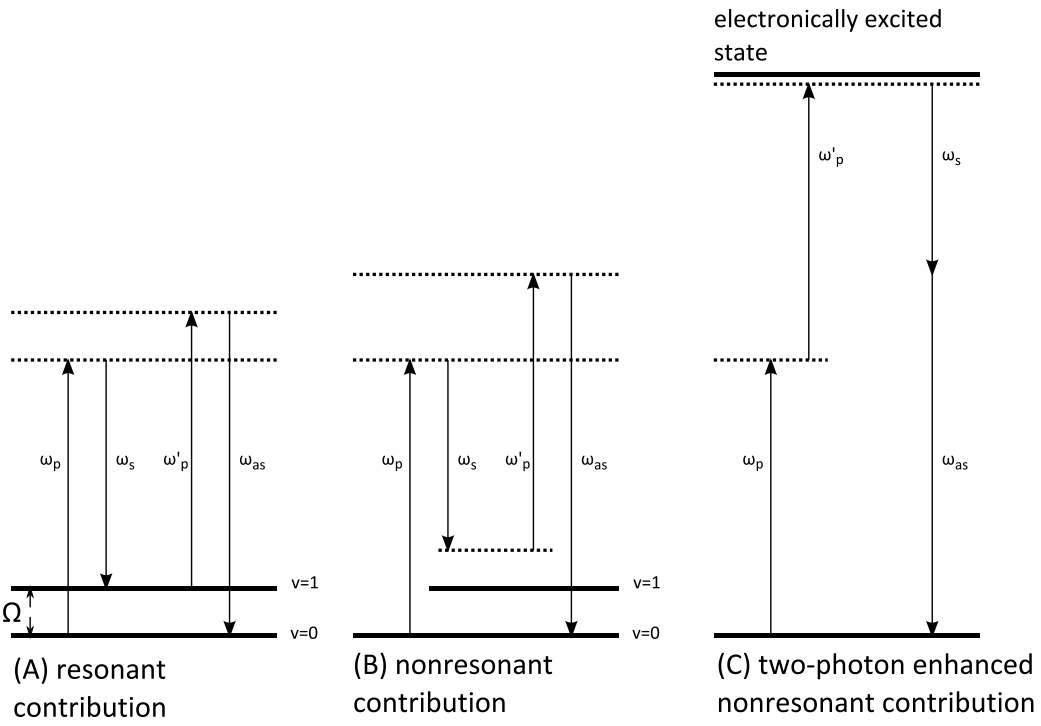

Figure 11 Energy diagrams showing: A. Resonant contribution, B. Non-resonant contribution, C. The two-photon enhanced non-resonant contribution.

Note that for simplicity the many different two photon ($\omega_p+\omega_s$, $2\omega_s$ etc) and one photon electronic transitions are not included. $\eta_{NR}^{(3)}$ and the two photon enhanced non-resonance contributions can be combined into a real number, $\chi_{NR}^{(3)}$, whilst the resonant contribution can be shown as $\chi_R^{(3)}$ giving:

$$\chi^{(3)} = \chi_R^{(3)} + \chi_{NR}^{(3)}$$

The mixing between the resonant and non-resonant terms also contributes to the CARS spectrum. The mixing term is negative when $\omega_p-\omega_s > \Omega$ and positive when $\omega_p-\omega_s > \Omega$. This creates a red shift of the maxima in the CARS spectra compared to the Raman spectrum as well as negative dip in the blue. The detuned spectrum and components are shown in Figure 12. This makes direct comparison with existing information in the literature on Raman more difficult. Spectral interference between two or more resonances may also result in distorted line shapes leading to unpredictable CARS spectra in crowded regions.[94]

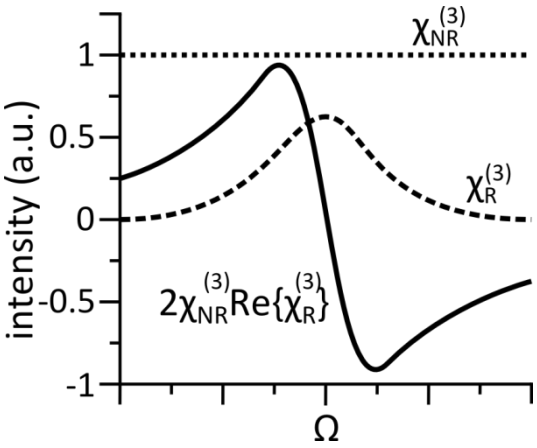

Figure 12 Three components of the CARS signal plotted as a function of detuning. Shown are the resonant term (dashed), the non-resonant background (dotted) and the mixing term (solid). Adapted from a similar figure 95.

The advantage of CARS over spontaneous Raman can be quickly attributed to the higher conversion efficiencies for similar incident laser powers. CARS signals were shown to be over 5 orders of magnitude higher and the use of near infrared frequencies allows considerable discrimination against a background fluorescence signal.[96]

The varying contributions of the resonant and non-resonant components of the CARS signal are highly dependent on the spectral pulse widths of the incident pump and Stokes beams. Assuming Gaussian spectral profiles, the pump and Stokes fields can be represented as:[97]

$$E_i = \frac{A_i}{\Delta_i^{\frac{1}{2}}} \exp\left[\frac{-2(\omega-\omega_i)^2 \ln 2}{\Delta_i^{\,2}}\right]$$

where E_i is the pump or Stokes field, Δ_i is the full widths at half-maximum of the pump or Stokes fields and A_i is a constant relating to the peak intensities. The prefactors keep the pulse energies the same when changing the spectral width. As Figure 13 shows, the dependence of both the resonant and non-resonant CARS signals increase with the pulse spectral width. Whilst the non-resonant signal shows a quadratic dependence, the resonant signal is saturated at high spectral widths.[97]

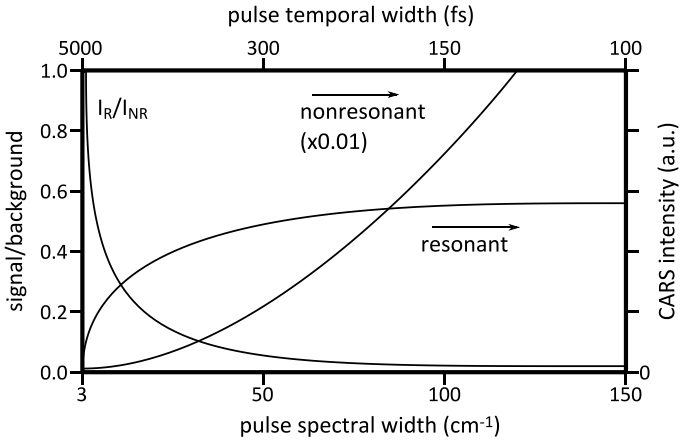

Figure 13 Intensities of the resonant and non-resonant signals as a function of the spectral widths of transform-limited pump and Stokes pulses with constant energies. Adapted from a similar figure in reference 97.

Raman line widths are typically condensed, usually much narrower than that of a femtosecond pulse. As only specific spectral components where the frequency differences lie within the Raman spectral profile can add to the CARS signal generation it is more desirable to use picosecond pulses which more closely match Raman line widths; this will add to the spectral resolution and sensitivity.

The use of near infrared lasers allows a significant improvement in signal to background ratio in CARS detection, due to the reduced scattering compared to lower wavelength light, but still contains significant amounts of non-resonant signals from the surroundings that can overwhelm the resonant CARS signals. This is particularly important with small objects when collecting the forward generated CARS signal (forward CARS, or F-CARS).[90] To further reduce this non-resonant background the CARS signal can be collected in the backwards direction (epi-detected CARS, or E-CARS). A diagram of a CARS microscope setup that shows the illumination and detection paths of both F-CARS and E-CARS is shown in Figure 15.

The backward CARS signal is highly dependent on the size of the scattering object as shown in Figure 14.

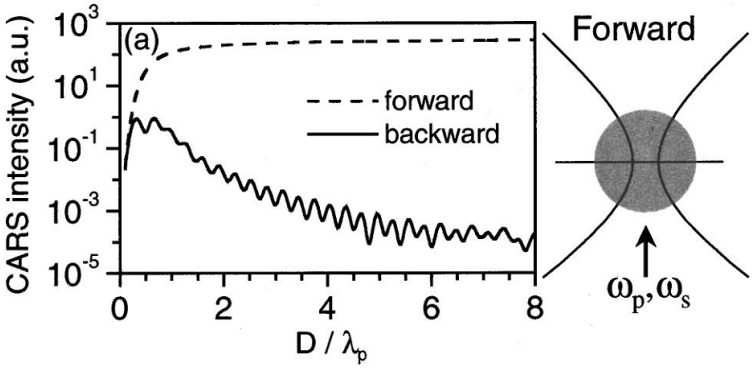

Figure 14 Forward and backward-detected signals as a function of the diameter of a spherical sample in a co-propagating beam geometry. Adapted from a similar figure in reference 91.

The backwards detected CARS signal has the same intensity as the forward signal when the scatterer diameter (D) is much smaller than the pump wavelength (λ_p). The first maxima is reached at D = 0.3 λ_p whilst at D = 8 λ_p the signal is 10^5 smaller than the equivalent forward detected signal. The oscillations in the backwards signal are due to the interference effects associated with the large wave vector mismatch in the backwards direction. The forward detected signal saturates at large diameters which leaves a large resonant and non-resonant contribution from the bulk medium that a sample is imaged in. The size discrimination of the backwards detected CARS signal effectively removes this unwanted background signal from the solvent that the scattering object is imaged in.[92,97,98]

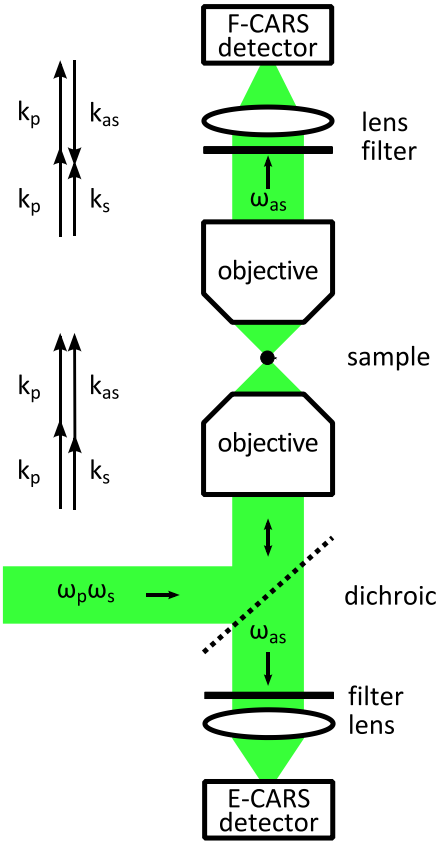

Figure 15 Schematic of the configurations for the F- and E-CARS microscopy with collinear pump and Stokes beams with confocal detection in the forward and backward directions. Adapted from a similar figure in reference 98.

CARS microscopy is also theoretically able to monitor changes in shape, or tumbling motions as the radiation pattern depends not only the size, but also on the shape of the scattering object. Figure 16 shows the radiation pattern from a rod, sphere and disk of the same volume.

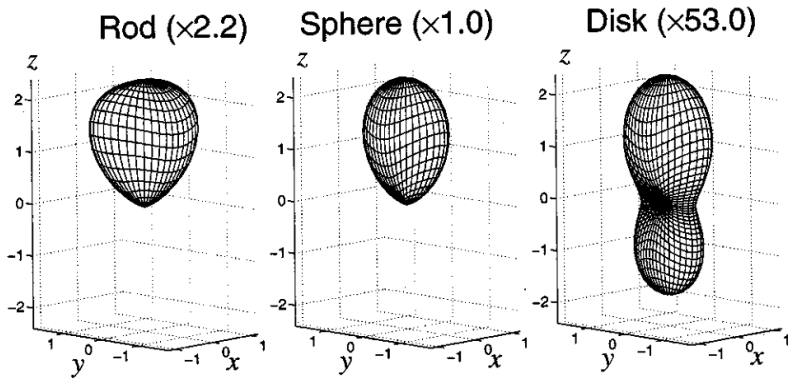

Figure 16 Far-field radiation patterns from scatterers centred at the focus with the same volume but with different shapes. The rod has a diameter of $0.2\lambda_p$ and an axial length of $2.0\lambda_p$. The sphere has a diameter of $0.78\lambda_p$. The disk has a diameter of $0.89\lambda_p$ and a thickness of $0.1\lambda_p$, Shown in parentheses are the intensity ratios between samples of different sizes and shapes. Adapted from a similar figure in reference 91.

The effect of the refractive index changes between the surrounding bulk media and the object being imaged is often, conveniently, omitted from theoretical calculations of CARS radiation patterns for simplicity, even though such situations will be rare experimentally.[91,92,97,98] Wave optics based simulations using a commercial finite-difference time-domain (FDTD) software show that with a high refractive index mismatch between solvent and scatterer, the excitation beam focal point becomes trapped within the scattering object as shown in Figure 17 A.

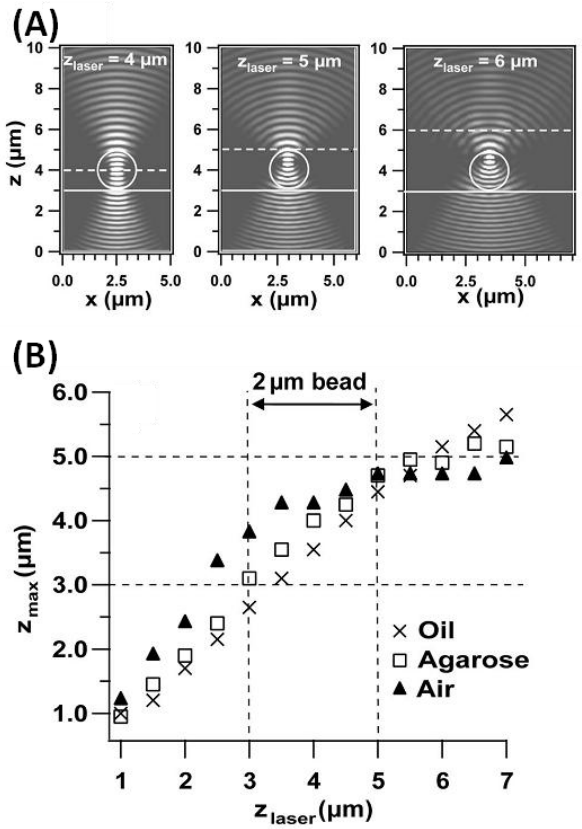

Figure 17 FDTD calculation in a 2µm polystyrene bead centred at z = 4µm. A. Excitation Poynting intensity mapping $I_{ex}(x,z)$ (λ = 800nm, waist 0.5µm) in the bead settled on a glass-air interface (z = 3µm, white line). In the absence of the bead the beam focuses at the z_{laser} = 4; 5 and 6µm (dashed lines). B. z_{max} versus z_{laser} for the bead embedded in various media (oil, agarose and air). Adapted from a similar figure in reference 99.

As the refractive index of the bulk medium (air, n = 1; agarose gel, n = 1.33; and oil, n = 1.45) diverges from that of the scattering bead (polystyrene, n = 1.6) the focal point of the beam remains confined within the bead (Figure 17 B), giving the effect of an elongated image in the z axis. The FDTD simulation also shows that 4.5% of the forward CARS emission is back reflected by the upper bead surface in air. Given the differences in detection efficiencies for forward and backward CARS signals this could be a major contributor to the epi-detected signal.[99]

2.7.2 Experimental characterization

The performance of the early CARS microscopes was dominated by the difficulties of the non-resonant background and the loss of signal at low molar concentrations probably due to the use of broad spectral pulses from femtosecond lasers. Imaging

biological tissue was particularly difficult due to the small concentrations of resonant chemical bonds within the cell sample. Soaking tissue in D_2O to image a resonance in a spectrally silent region or to remove any heating effects due to an H_20 absorption overtone was often required, and even then this produced images with poor resolution and contrast.[90,96]

Working with model particles such as polystyrene beads has proved to be a more useful tool in the characterisation of CARS microscopy systems. The Raman spectra of polystyrene (shown in Figure 18) includes a number of isotropic peaks within the fingerprint regions (1000-2000cm^{-1}) as well as characteristic CH_2 symmetric and asymmetric stretches in the 2800-3000cm^{-1} region. The C-H stretch region is of particular interest due to the large lipid contribution to cellular spectra from the alkyl chains of lipids.[100-103] Polystyrene beads are also available in commercially prepared suspensions at well defined sizes, as well as conjugated with a variety of fluorophores.

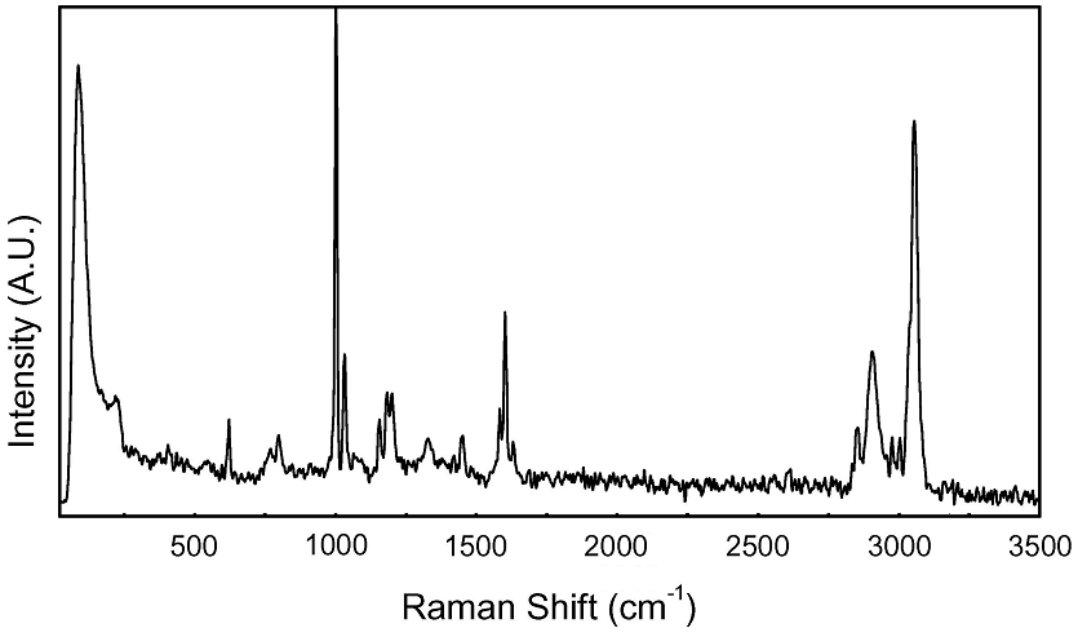

Figure 18 Raman spectra of polystyrene. Adapted from a similar figure in reference 102.

CARS spectra are difficult to obtain as each measurement requires the Stokes frequency to be tuned point-by-point. This usually limits measurements and comparisons to narrow portions of the Raman spectrum. Figure 19 shows a CARS spectrum obtained with a constant pump (ω_p = 854nm) and a variable Stokes (ω_s

tuned in 2nm steps from 1,120nm to 1,170nm). The repetition rate of the laser was 250 kHz. The spectral resolution was around 60cm^{-1} which reduces the ability to see sharp spectral features. The resonant CARS signal was normalized to the non-resonant background (<5% of the resonant signal) to compensate for intensity variations associated with wavelength changes of the Stokes beam.

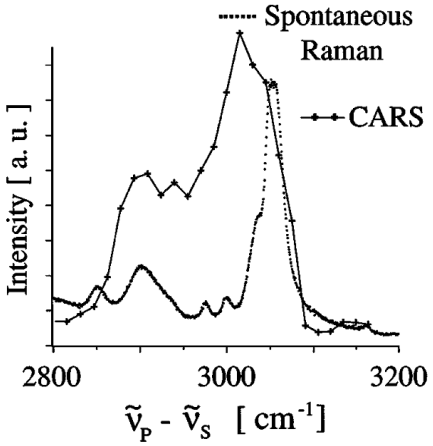

Figure 19 CARS spectrum (crosses with solid lines) of a 910 nm diameter polystyrene bead. Adapted from a similar figure in reference 90.

Peaks at 2851 and 2902cm^{-1} are assigned to C-H stretching vibrations in the polymer backbone (see Figure 20 B) whilst the peak at 3054cm^{-1} is due to the phenyl C-H stretching vibrations (see Figure 20 A).[90]

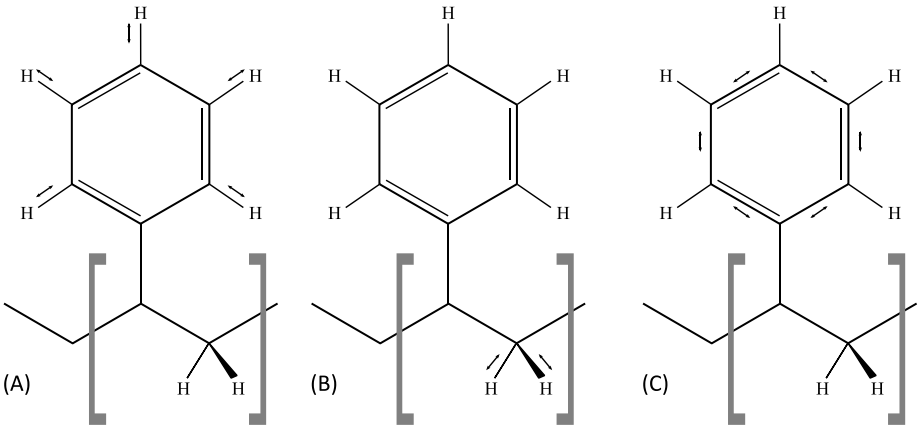

Figure 20 Common Raman active modes used in CARS spectroscopy. A. Phenyl group C-H in plane stretching (3010-3120cm^{-1}). B. Polymer chain C-H stretch (2800-3000cm^{-1}). C. Phenyl group C-C tangential stretch (1580-1630cm^{-1}).

Figure 21 shows a similar CARS spectrum to that shown in Figure 19, a polystyrene film coated on a cover slip was measured with a constant pump (ω_p = 712 nm, average power of 140 μW) with variable Stokes wavelength (average power around 65 μW). A pulse duration of 5 ps with a repetition rate of 80 MHz was used.[97] The spectrum is more detailed not only due to the increased number of samples taken but the finer spectral width of the lasers sources used.[92]

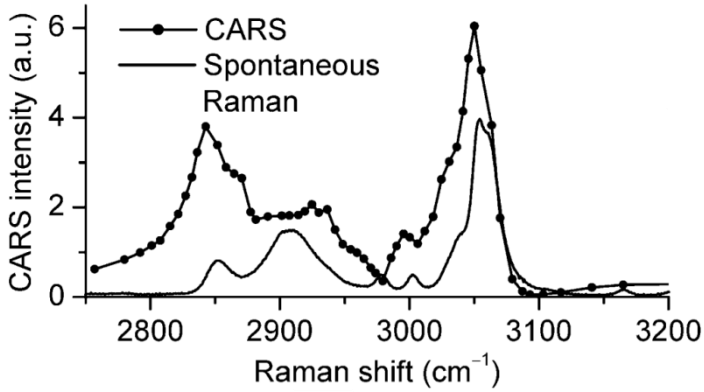

Figure 21 CARS spontaneous Raman spectra of a polystyrene film coated on a cover slip. Adapted from a similar figure in reference 92.

Figure 22 show similar spectra centred on the 1600 cm^{-1} Raman shift associated with C-C quadrant stretches in the phenyl ring of polystyrene (see Figure 20 C). Figure 22 A was taken with an average pump power of 780 μW and an average Stokes power of 390 μW with the pump frequency fixed at 13,325 cm^{-1}. A pulse duration of 5 ps with a repetition rate of 80 MHz was used.[97] Figure 22 B was taken with an average pump power of 100 μW and an average Stokes power of 50 μW with the pump frequency fixed at 13,505 cm^{-1}. A pulse duration of 5 ps with a repetition rate of 80 MHz was used.[97] Both curves exhibit a strong red shift in their peak positions compared to the spontaneous Raman spectra as well as a dip in the higher wave numbers similar to that shown in Figure 12.[91,97]

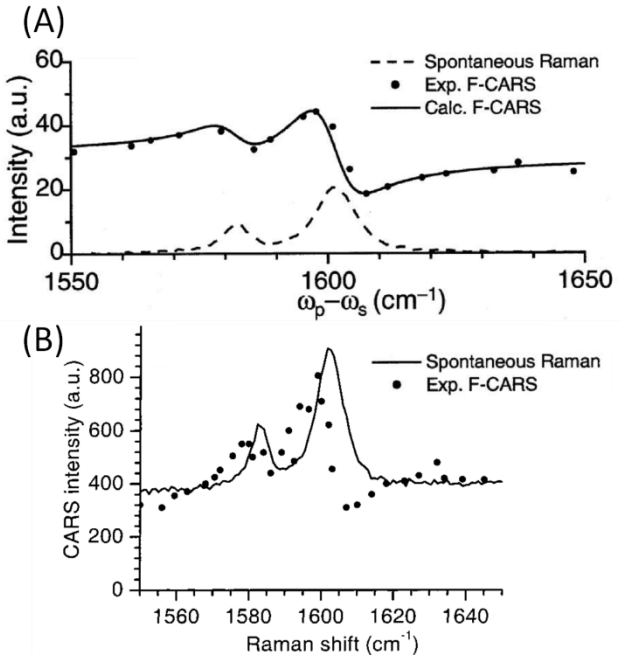

Figure 22 CARS spectra of polystyrene. A. F-CARS and spontaneous Raman spectra of a polystyrene film spin coated onto a cover slip. B. F-CARS spectrum of a single polystyrene bead of 1 μm diameter spin-coated on a cover slip. . Adapted from similar figures in references 91,97.

Figure 23 shows two and one dimensional scans of 6.2 μm polystyrene beads embedded in an aqueous solution with near matched refractive index and no interfering Raman peaks in the region imaged. The pump wavelength was fixed to 730.3 nm and the Stokes wavelength was scanned between 784.4 and 793.3 nm in order to probe the aromatic ring breathing. Single bead scans are along the equatorial plane with the intensity normalised to that of the aqueous solution.[104] In Figure 23 B and D there are clear dips in the CARS intensity at the interface between the bead and the surrounding medium. This effect has been shown to be more pronounced when the refractive index mismatch between the scattering object and the bulk medium is greater and has been attributed to destructive interference between the two anti-stokes fields produce by the differing mediums of bead and solvent.[98,104,105] The other point to note is the inverted image (Figure 23 C) that appears when the frequency scanned is around the spectral dip due to the negative value of the mixing term (see Figure 12 for details).

Figure 24 A shows an E-CARS image of 0.1 μm polystyrene beads in agarose gel. Unlike F-CARS signals, E-CARS images do not exhibit any dips in signals where

there are refractive index changes. This is most likely due to the effective rejection of the background signal. Additionally, the full width at half maximum (FWHM) of E-CARS images are better than those of F-CARS signals (see Figure 24 B and C) and were calculated to be better than the one photon confocal resolution.[98,105]

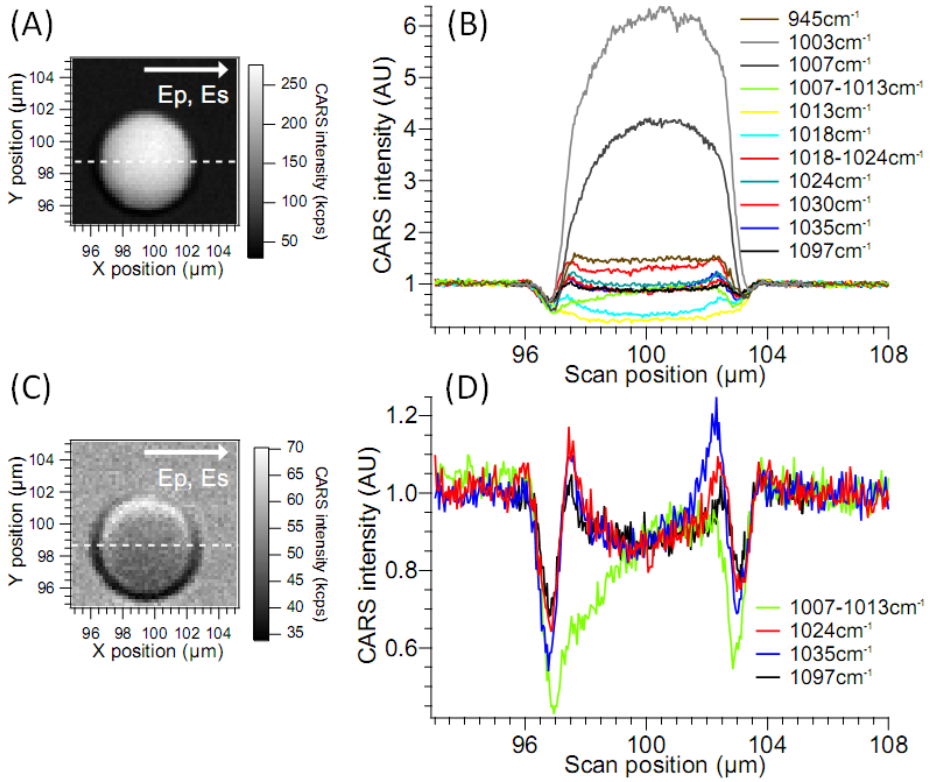

Figure 23 Two and one dimensional scans of a 6.2 µm polystyrene bead embedded in an aqueous solution around the 1003 cm^{-1} polystyrene resonance. The pump and Stokes powers are both equal at 500 µW with 76 MHz repetition rate and a 3 ps pulse duration. A. Bead image on resonance. B. One dimensional scans across dotted line for various Raman resonances. C. Bead image off resonance. D. One dimensional scans across dotted line for various Raman resonances. The pump and Stoke beams linear polarizations are indicated by the white arrows. Adapted from similar figures in reference 104.

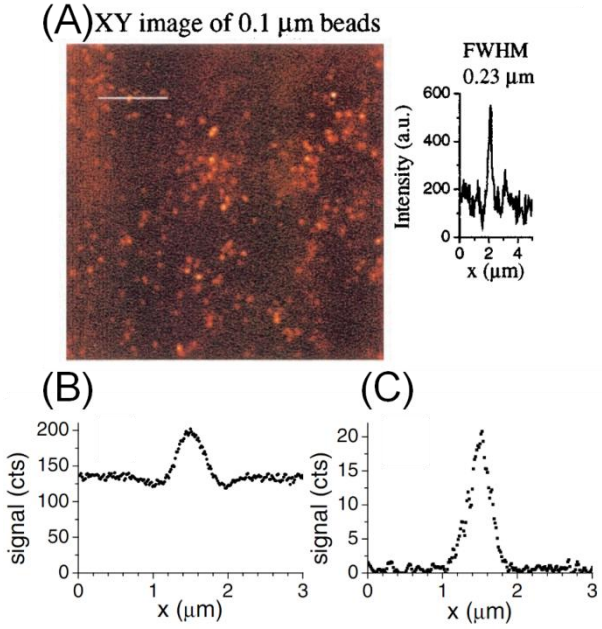

Figure 24 E-CARS and F-CARS images and scans of polystyrene beads. A. E-CARS lateral (*xy*) image of 0.1µm polystyrene beads embedded in agarose gel and inset E-CARS intensity profile. B. F-CARS and C. E-CARS intensity profiles of a polystyrene bead with 535 nm diameter on a glass cover slip and covered in water. Raman shift was centred at the 1600 cm^{-1} with average power of 50 and 25 µW for pump and Stokes lasers with a 250 kHz repetition rate and 110 fs pulse duration). Adapted from similar figures in references 98,105.

The ability of CARS to pick out different chemical compounds is shown in Figure 25 which contains both polystyrene and PMMA. Images were recorded with the pump wavelength at 752 nm with a power of 20 mW. The Stokes laser was quickly shifted to give ω_p-ω_s as 2845 or 3054 cm^{-1} by manually translating the OPO crystal mount which could be performed at sub-second rates. The laser generated a 1.2 ps pulse at 76 MHz repetition rate. This grants the ability to look at two different wavenumbers in the same sample and rapidly switch between then. The Stokes power was approximately 40 mW. Polystyrene contains both C-H aliphatic vibrations around 2845 cm^{-1} and C-H aromatic vibrations around 3055cm^{-1} whilst PMMA only contains C-H aliphatic vibrations. The picture captured at 2848cm^{-1} shows both the large polystyrene beads and smaller PMMA beads, whilst switching to 3035cm^{-1} leaves only the polystyrene beads visible.[106]

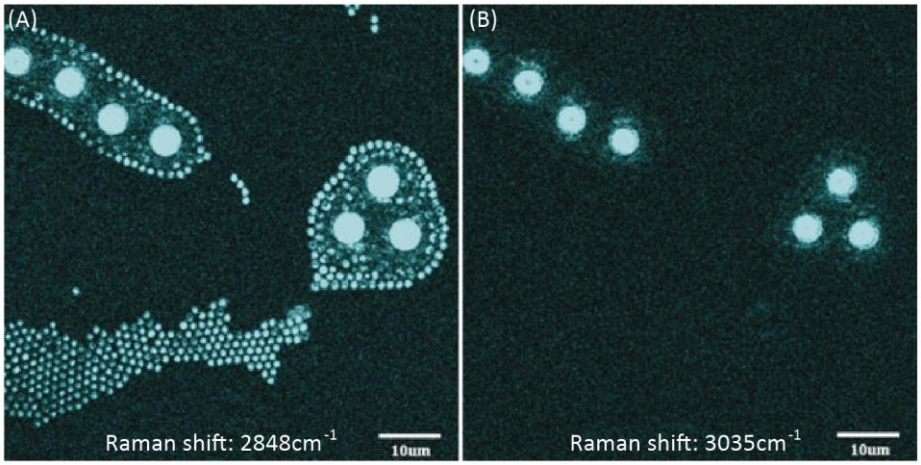

Figure 25 CARS images of a mixture of 10µM polystyrene beads and 1.4µM PMMA beads at Raman shifts of: A. 2848cm^{-1} and B. 3035cm^{-1}. Adapted from a similar figure in reference 106.

2.7.2.1 Backwards scattered CARS signals

The back scattered E-CARS signal has been shown to contain a significant contribution from a back reflected F-CARS signal. This contribution was examined using 2 µm latex beads on glass cover slips with a pump power of 0.2 mW and Stokes power of 0.1 mW. The laser had an 80 MHz repetition rate and 3 ps pulse duration. The lasers were tuned to image at the Raman shift centred around 1600 cm^{-1}. Figure 26 shows the F-CARS and E-CARS signals while scanning along the *z* axis at the centre of the bead on the *xy* plane. As the refractive index mismatch between the bulk solvent and the latex bead decreases, the back collected signal disappears. This suggests that a proportion of the back reflected signal is a backward-reflected F-CARS emission.[99]

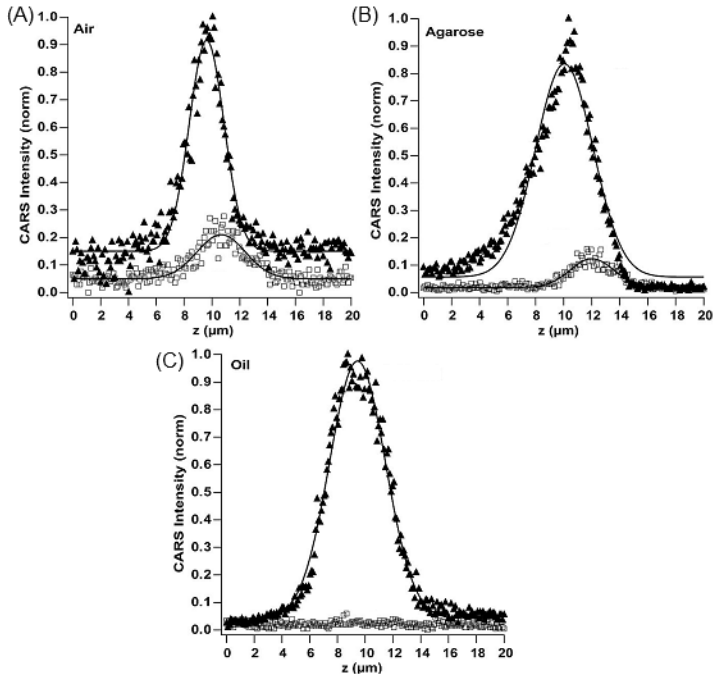

Figure 26 F-CARS (triangles) and E-CARS (squares) profiles along the z axis for 2μm beads embedded in different media of refractive index *n*. A. Air, *n* = 1; B. Agarose gel, *n* = 1.33; C. oil, *n* = 1.45. Adapted from a similar figure in reference 99.

The differences between F- and E-CARS collected signals can be seen in Figure 27. A-D were taken with a pump frequency of 12,242 cm^{-1} and power of 20 mW, and Stokes frequency of 9,398 cm^{-1} and power of 15 mW. The laser had a 76 MHz repetition rate and 6 ps pulse duration. E-F were taken with a pump frequency 14,170 cm^{-1} and power of 39 mW, and a Stokes frequency of 11,330 cm^{-1} and power of 17 mW. The repetition rate was 76 MHz and the pump and Stokes pulses were around 2 and 3 ps respectively. The CARS images from the adipocytes have the ω_p-ω_s tuned to the symmetric C-H_2 stretch found in lipids. The F-CARS images show the lipid droplets in the cell, whilst the E-CARS image is absent from most lipid drops instead showing a signal from the edge of some of the droplets. This has been be attributed to newly emerging lipid drops that exhibit strong E-CARS contrast due to the size-dependent nature of the E-CARS signal. Back reflection of the F-CARS signal may also be responsible for the occurrence of E-CARS signals collected at the centre of the larger lipid droplets.[107] Figure 27 E shows 1 μm melamine beads with the F-CARS signal shown in red and E-CARS shown in green. This data in some respects contradicts the previous example as the F-CARS signal can be seen arising

from the central region of the bead, whilst the E-CARS signal is present across the entire bead (see Figure 27 F for line traces).[108] These images are good examples of the complementary data that can be gathered from the two different methods of collecting the CARS signal.

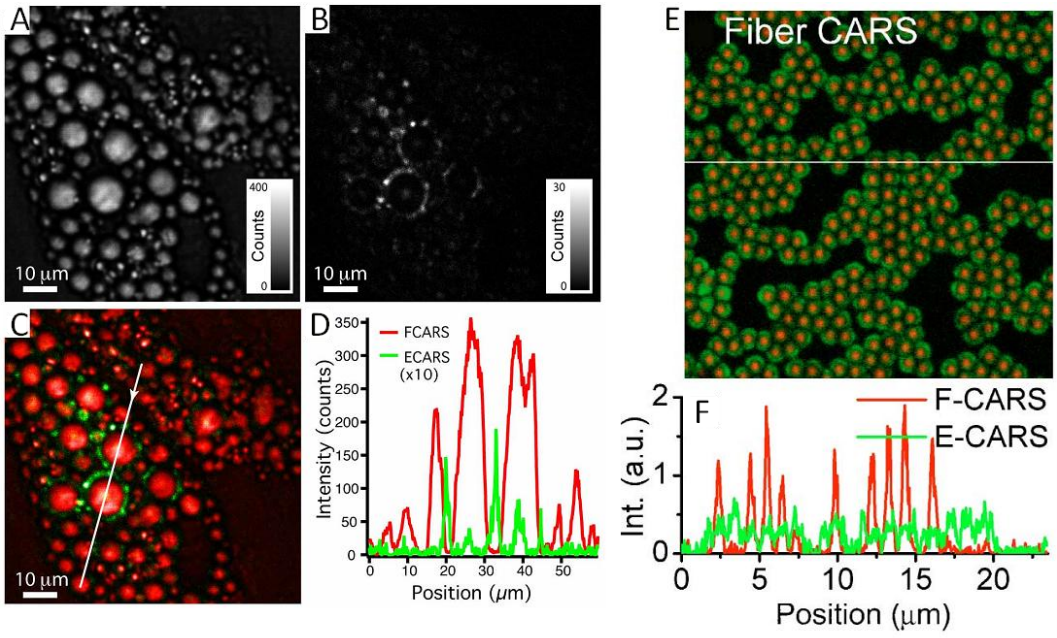

Figure 27 F and E-CARS images. A-C Time-gated CARS images of MSC-derived adipocytes. A. F-CARS, B. E-CARS, C. Overlay of the F- and E-CARS images, D. Line section of the CARS signals as indicated by the white line in C. E. CARS image of 1µm melamine beads with a fiber delivered laser source, F-CARS in red; E-CARS in green. F. Line section of the CARS signal indicated by the white line in E. Adapted from a similar figures in references 107,108.

2.7.3 CARS in biological systems

CARS instrumentation has long been developed with a goal for imaging cells and other biological material. A vibrational microscopy technique offers chemical selectivity without the need for exogenous labels or relying on a limited native fluorescent signal. This allows untreated live cells to be imaged, as well as tissue samples.

In biological samples the strongest signals are seen from lipids in the C-H stretching region, around 2800-3000 cm^{-1}, and much of the CARS literature is based around the use of CARS to view lipids in cells as they provide good contrast between the cell and its surroundings. Lipids also play an important role in many cellular functions:

they are the major constituent of cell membranes, they serve as an energy store and they are also used as cellular messengers.[109] Although lipids can be visualised using added fluorescent lipid molecules, introducing these molecules into a sample can be a challenge, and cells often require fixation to allow the tagged molecule to enter the cell. The newly introduced fluorescent lipid may also affect the structural and biological properties of the membrane it intercalates into due to the bulky fluorescent tag.

CARS' ability to image lipids label-free is particularly important when imaging lipids in living cells or organisms such as in *Caenorhabditis elegans*, a model organism used in exploring lipid interactions. Fluorescent tags can be introduced through adding fluorescently labelled lipids to the diet. However, the distribution of these lipids in the organism may not be perfectly even. Genetic defects, particularly those linked to lipid uptake and storage can alter how these lipids are incorporated across the organism.[110] As CARS images do not depend on an introduced tag molecule, it is free from artefacts that can be caused by differential staining of regions of interest.

CARS can also be useful in a clinical setting where introducing labels may be impractical. One example is in atherosclerotic lesions, which are caused by the accumulation of fatty materials in arteries. Early detection of these lesions are difficult as they are usually asymptomatic, and also difficult to detect and quantify using angiography.[111] Using CARS can help to identify lipid rich macrophage cells and lipoprotein aggregates and asses their risk of rupture.[112,113] The 3D sectioning capability can be used to reconstruct accurate models of a plaque (see Figure 28 for example), whilst changes in lipid morphologies can be measured due to the changes in vibrational peaks at different wavelengths.[114]

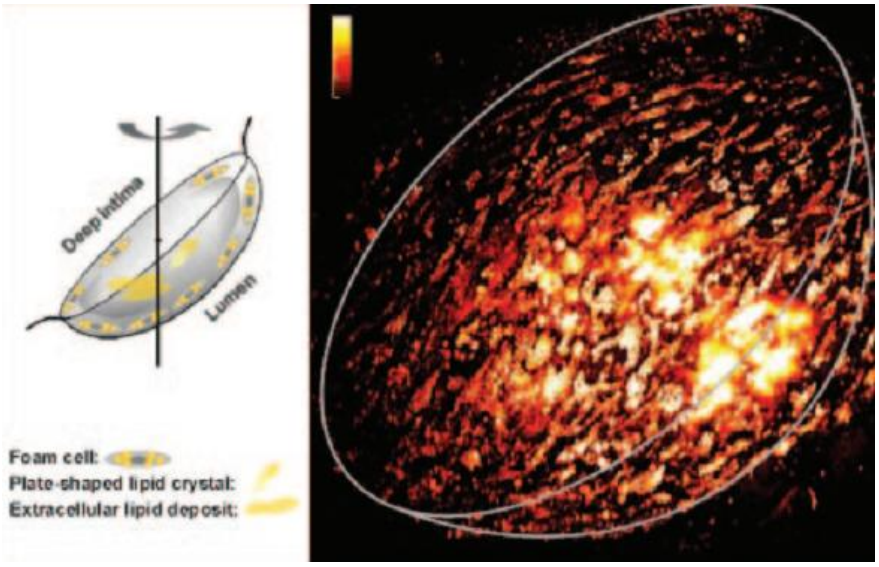

Figure 28 Consecutive en face CARS image slices of atherosclerotic lipids were 3D constructed. The left panel is the schematic diagram of 3D reconstruction of a single atherosclerotic plaque shown in the right panel. The Stokes laser had a repetition rate of 76 MHz and 7 ps pulse duration, whilst the pump laser had a 76 MHz repetition rate and 6 ps pulse duration. Total laser power on the sample was less than 40 mW. Adapted from a similar figures in reference 114.

When imaging individual cells, the contrast CARS provides when imaging at the lipid wavelength shows up the contents of the cell compared to the surrounding solvent. The nucleus can be picked out due to the lower overall CARS signal compared to the cytoplasm, whilst lipid droplets show up as bright, high intensity dots (see Figure 29 for example).[115] CARS can be used to track the movement of lipid droplets around the cell in real time without perturbing the cell.[116] Proteins also contain a strong peak in the C-H stretch region, typically with a peak around 2950 cm^{-1}; CARS has been used to image the changes in protein distribution as a cell undergoes apoptosis.[117]

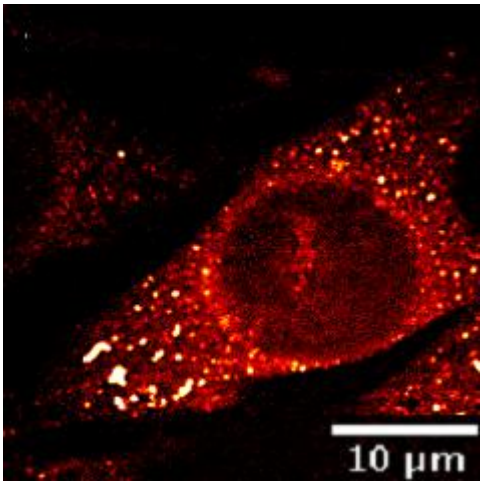

Figure 29 F-CARS image of a fibroblast cell. Image was taken using an 80 MHz repetition rate and 2 ps pulse duration. The laser power on the sample was estimated at 28 mW. Adapted from a similar figures in reference 115.

2.8 Imaging nanoparticles

One potential area of application for CARS has been the imaging of nanoparticles in cells and tissues. There are many different sources of nanoparticles, some of them engineered for specific applications such as the addition of TiO_2 and ZnO nanoparticles to cosmetics,[118] or antibacterial silver nanoparticles added to clothing.[119] Unwanted generation of nanoparticles in both manmade and natural processes including in volcanic activity,[120] exhaust fumes,[121] and industrial waste[122] also contribute to the environmental load.

The health effects of nanoparticles have been identified as an area for concern both by scientists and the general public,[123] and there is often little information on the toxicity of these products in humans or animals.[124] Inhalation,[125] dermal absorption,[118] ingestion[126] and systemic administration[127] have all been shown as routes of exposure to nanoparticles. Toxicity is often associated with inflammatory responses, as well as oxidative stress, and has been shown to result in DNA damage and apoptosis.[128,129] Imaging particles in cells can be a key process in the understanding the effects of nanoparticles on cells.

CARS has already been employed to view a number of micro and nano sized particles in biological systems. Particles studied typically tend to be metal oxide particles, including MRI contrast agents such as iron oxide, as these have large non-

linear susceptibilities. Images of these particles have been taken in both cells[130,131] and tissues[132] showing the versatility of CARS. Gold nanoshells and nanoparticles, which serve as potential drug carriers or contrast agents are also targets of interest due to the reduced photodamage and photo toxicity associated with multiphoton imaging.[133,134]

These studies typically take advantage of the two-photon enhanced electron contribution of metal oxide semiconductors which have a $\chi^{(3)}$ value that is far greater than those for biological materials.[131] This contribution is enhanced when the band gap transition absorption wavelength is close to the energy of a two photon absorption by the pump laser. The four-wave mixing results in a photon produced at the same wavelength of a CARS photon under the same pump and Stokes wavelengths. As this does not depend on any vibrational resonance, and the response is quite broad, ω_p-ω_s can be tuned away from any biologically relevant resonance to image the nanoparticles. Images at resonant and non-resonant wavelengths can then be recombined to show where the nanoparticles can be found in the sample, as well as the sample structure and composition, as shown in Figure 30.

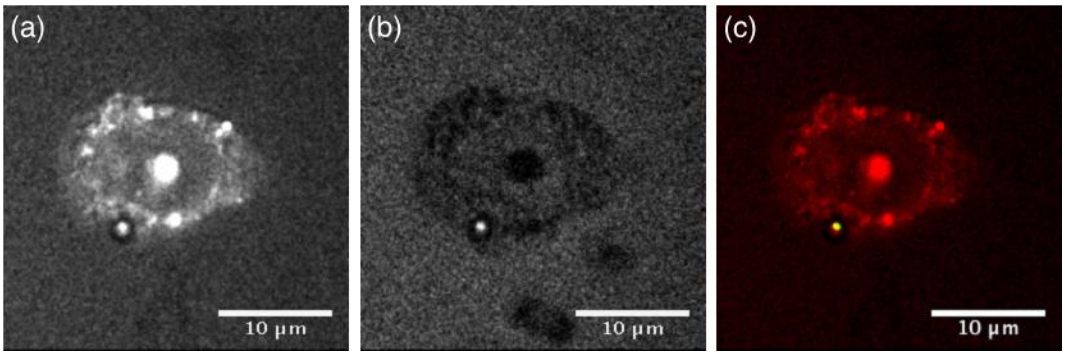

Figure 30 CARS images of a HuH7 cell (human epithelial like cell) incubated with FeO microparticles. A. C-H stretch on-resonance B. Off-resonance CARS images of a HuH7 cell (human epithelial like cell) C. Overlay image showing iron oxide particle in green. Adapted from figures in reference 130.

3 Materials and methods

3.1 Materials

3.1.1 Reagents

Adenine (A3159), Cytosine (C3506), Guanine (G11950), Thymine (T0376), Sodium Hydroxide (S5881), Isopropanol (I9516), Bovine Serum Albumin (BSA) (A2153), IgG ((I4506), Glutaraldehyde (G7651), Immersion Oil (56822), Phorbol 12-myristate 13-acetate (TPA) (P1585), Calcium Chloride (C2661), Percoll (P4937), Dextran (D4626) were purchased from Sigma Aldrich (Dorset, UK).

Dulbecco's modified Eagle's medium (DMEM) (21331020), Roswell Park Memorial Institute 1640 medium (RPMI 1640) + Glutamax (61870010), Iscove's modified Eagle's medium (IMEM) (A1048801), phosphate buffered saline (D-PBS, or PBS) 1× (10010015), D-PBS 10× (AM9624), Trypsin 10× (15400054), Penicillin-Streptomycin (15070-063) were purchased from Invitrogen (Paisley, UK).

HyClone Fetal Bovine Serum (SH30070.03) was purchased from Thermo-Fisher (Leicestershire, UK)

3.1.2 Particles

Fluorescent yellow-green polystyrene microspheres, 0.03 μm in size (L5155); Polystyrene beads, 0.1μm (LB3), 1.1μm (LB11), 5μm (79633); Polymethylmethacrylate microparticles, 1μm (90875); TiO2 nanoparticles (718467) were purchased from Sigma Aldrich (Dorset, UK). Polybead polystyrene sampler kit containing: 0.5 μm, 0.75 μm, 0.1 μm, 0.2 μm and 0.3 μm beads (19822), were purchased from Park Scientific (Northampton, UK).

Ceridust 3610 micronized high density polyethylene wax, mean size 5 μm, was purchased from Clariant (Muttenz, SwitzerlanD).

3.1.3 Wear particles

UHMWPE debris were isolated from a pin-on-plate wear simulator.[135] 10 M of NaOH was added to 60 ml of lubricant collected from the simulator, and incubated for 24 hours. It was then centrifuged using a Beckman SW41Ti rotor and L70 ultracentrifuge at 104,000 g for 3 hours. The pellicle was removed and suspended in filtered water before an isopropanol gradient was layered on top of the debris

solution (two layers, densities 0.96 and 0.90 g cm^{-3}) and then centrifuged for 1 hour at a speed of 207,000 g. The purified UHMWPE particles were then harvested from the interface of the two isopropanol layers.

3.2 Methods

3.2.1 Filtration

An All-Glass Filtration Holder (50 mm) from Sartorius-Stedim (Surrey, UK) and Polycarbonate Filters, 0.1 μm (7060-4701), 0.2 μm (7060-4701), 8 μm (7060-4714) and 10 mm (7060-4714) purchased from Whatman International (Maidstone, UK) were used to filter isolated UHMWPE particles. Polystyrene particles were either filtered on 8 μm and 0.2 μm polycarbonate membranes (Whatman International Ltd, Maidstone, UK) using a syringe driven filter or, polyethylene particles were added to triple filtered water and then filtered through 10 μm and 0.1 μm membranes placed in a glass vacuum filter (Sartorius Stedim UK, Surrey, UK). Filtration took place in a class II laminar flow cabinet.

3.2.2 Electron microscopy

Polycarbonate filters were then placed on aluminium stubs with double sided carbon pads and sputter coated with 5 nm of gold/platinum. Samples were viewed in a Hitachi S4700FII field emission scanning electron microscope at up to 20,000× magnification. Digital images were recorded using Hitachi FE PCSEM (version 3.2) software (Hitachi High Technologies, Wokingham, UK).

Particles were masked from the background of filters either using thresholding or by selecting areas by hand. Water shedding or manual adjustment was used to split joined particles. Particle sizes were calculated using the 'analyze particles' function in ImageJ (National Institute of Health, Maryland, USA).

3.2.3 Cell culture

Monocyte derived macrophages were isolated from peripheral blood donated by healthy volunteers in agreement with the University of Edinburgh's ethics practices. 160 ml of blood was withdrawn and centrifuged at 300g for 20 minutes to separate the cellular component from the plasma. Autologous serum was generated by precipitation of platelets from the plasma with calcium chloride and gentle heating in a water bath. The cell pellet was mixed with 5% dextran in PBS and gravity

sedimentation was used to isolate the red blood cells. The remaining supernatant was then centrifuged at 300g for 5 minutes to pellet the leukocyte cells. These were then layered on a Percoll gradient (55%, 68% and 81%) and centrifuged at 720g for 20 minutes to separate monocytes from neutrophils. Monocytes were harvested between the 68% and 81% layers of Percoll and centrifuged twice in PBS at 230g for 5 minutes. The cells were then plated on glass bottomed dishes at a density of 1×10^6 cells/ml in IMEM supplemented with 10% autologous serum and penicillin/streptomycin (10,000 units/ml). Non-adherent cells were gently removed via pippetting whilst monocytes were left to mature for 7-10 days before use.

Human embryonic kidney (HEK 293), mouse embryonic fibroblast (NIH 3T3), human breast adenocarcinoma (MCF-7 and MDA-MB 231) cells were all grown with DMEM media with 10% foetal bovine serum and penicillin/streptomycin (10000 units/ml) at 37 °C with 5% CO_2 atmosphere. Cells from passages 5-50 were seeded on glass bottomed dishes at a density of 0.25×10^6 cells /ml for 24 hours.

Mouse leukaemic monocyte macrophage (RAW 264.7) cells were grown with RPMI1640 Glutamax with 10% foetal bovine serum and penicillin/streptomycin (10000 units/ml) in untreated cell culture plastic in standard growth conditions at 37 °C with 5% CO_2 atmosphere. Cells from passages 5-15 were seeded on glass bottomed dishes at a density of 0.5×10^6 cells/ml for 24 hours.

Human promyelocytic leukemia (HL-60) cells were grown in DMEM with 10% FBS and penicillin/streptomycin (10000 units/ml) in tissue culture plastic. Cells were seeded on glass bottomed dishes at a density of 1×10^6 cells/ml and differentiated with 1 nm TPA (phorbol 12-myristate 13-acetate) for 24 hours. Non-adherent cells were removed with gentle pippetting.

Cells were challenged with particles for 24 hours unless stated otherwise. After particle incubation the cells were washed either in media or in PBS, fixed in 1% glutaraldehyde in PBS for 5 minutes and then washed several times with PBS and then water before imaging.

3.2.4 Raman

Raman spectra were gathered from materials using a Renishaw InVia system (Gloucestershire, UK). A 785 nm laser was focused through either a 20× (0.4 NA) or

50× (0.75 NA) objective to excite the Raman bands. Exposure time ranged from 10 to 30 s with up to 6 repeats and cosmic ray removal selected. A 1200 l/mm diffraction grating was used in collection. The Raman spectra were calibrated using the 'Quick Calibration' function in the Wire 2.0 software (Renishaw) and a silicon sample. Samples were placed onto magnesium fluoride cover slips. Cells were plated at a density of 5×10^6 cells / ml on Magnesium Fluoride cover slips for 1 hour before the addition and mixing of either 4 µl per ml of 1.1 µm polystyrene particles or 10 µl per ml of Ceridust in media for 24 hours. Cells were fixed in glutaraldehyde and dried unless otherwise stated.

Raman data was analyzed using Wire2.0 software with a background from an empty magnesium fluoride cover slip and a base line subtracted from each spectrum.

3.3 Multiphoton microscope

The multiphoton microscope was designed and built at The University of Edinburgh by Downes, et al.[136] although the setup had been changed for the use in this thesis.

The illumination for our multiphoton microscope is shown in Figure 31 and consists of a mode-locked neodymium doped yttrium vanadate orthovanadate ($Nd:YVO_4$) laser source (PicoTrain, High-Q laser, Hohenems, Austria) which produces a Stokes pulse (7.5 ps FWHM, 1064 nm) used in the CARS process. The source also produces a 6 ps FWHM, frequency doubled 532 nm beam which is used to pump a picosecond optical parametric oscillator (OPO) (Levante Emerald, Berlin, Germany). The OPO delivers a signal tunable in the range 700-1000 nm (6 ps, FWHM), which is used as a pump in the CARS process or as the excitation beam for TPEF. One or two beams are combined using a dichroic mirror (DM) and focused into the input of a laser-scanning confocal optical microscope (Nikon BV C1, Amsterdam, Netherlands) which is shown in Figure 32. The pulses are synchronized by adjusting a micrometer-driven delay stage. These wavelengths are reflected towards a 60× oil immersion objective (Plan Apo VC, Nikon) with a 1.4 numerical aperture (NA) by a DM. The forward signal is collected by an air condenser (NA 0.72) and directed to a multimode fibre via mirror and tube lens. The fibre directs the signal to a DM and then onto two different photomultiplier tubes (Hamamatsu R3896, Shizouka, Japan).

A set of short pass filters and a band pass filter of appropriate wavelengths (Chroma, Rockingham, USA) were used before the fibre. The epi-detected signal is collected by the objective lens and passes through a dichroic mirror in the scan unit. The signal is then directed via a multimode fibre to the same detector setup as used in the forward signal. A set of appropriate short pass and band pass filters are used after the fibre. CARS signals were confirmed by blocking either the pump or Stokes laser, or by adjusting the delay stage which caused no signal to be collected.

The laser powers were measured after the objective by placing a S121B standard power sensor (Thorlabs, Cambridgeshire, UK) over the microscope objective and adjusting the position of the focus and sensor to give the maximum power reading. Although this method is likely to be an underestimation of the actual laser power as not all the incoming photons are collected by the sensor, the readings give internally comparable readings.

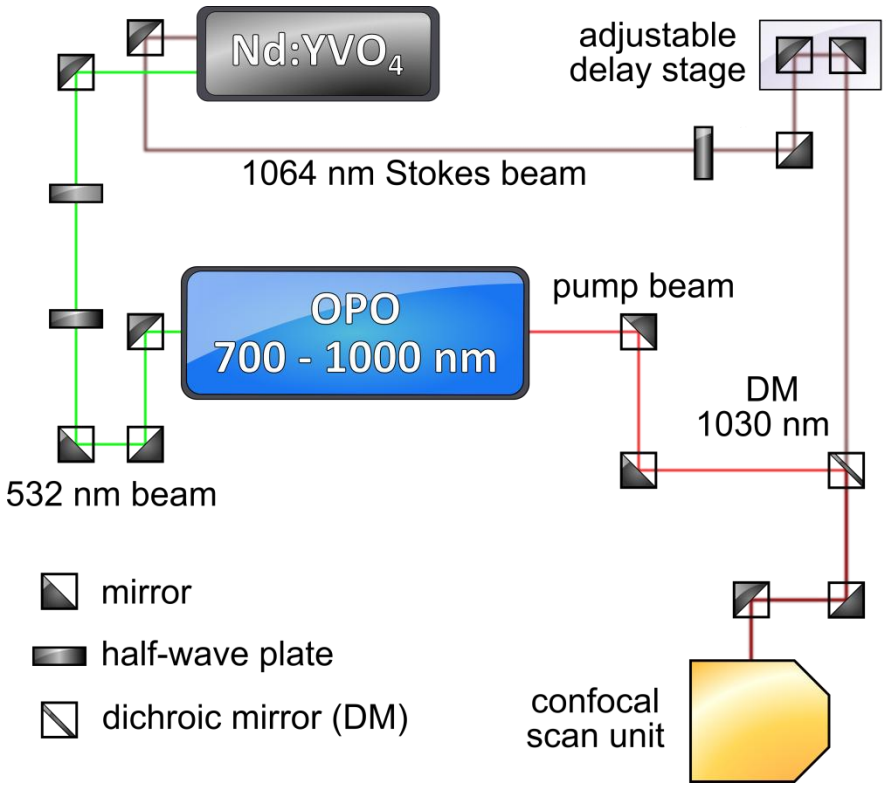

Figure 31 Schematic of illumination sources. The Nd:YVO_4 pump produces both the Stokes pulse (1064 nm, 7.5 ps FWHM) as well as a frequency doubled 532 nm, 6 ps FWHM beam used to drive an optical parametric oscillator (OPO). The OPO produces the pump beam which is tunable from 700 – 1000 nm (6 ps FWHM). Both the Stokes and pump beams are combined using a dichroic mirror and enter into a confocal scan unit of a Nikon C1 microscope.

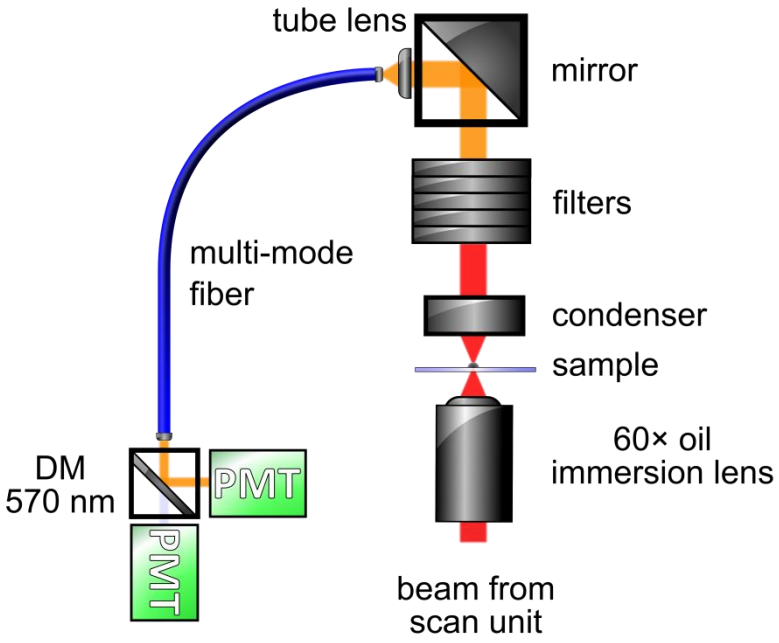

Figure 32 Schematic of CARS microscope and detection. A dichroic mirror in the scan unit reflects the wavelengths towards the objective lens where it is focused on the sample. The forward scattered light is collected by a condenser lens and passed through a series of filters before being focused into a multi-mode fibre via a mirror and tube lens. The fibre passes the signal into a detector unit where a final dichroic mirror sends the signal to one of two photomultiplier tubes (PMT).

3.3.1 CARS resolution

The lateral resolution of our CARS microscope was measure using images of TiO_2 particles and the 'fit multi-peaks' function in Origin 8.1 (OriginLab corporation, Massachusetts, USA). An *xy* line trace through the collected image is shown in Figure 33 as the black line. The mean FWHM was calculated as 0.30 μm. The axial resolution was calculated using 6 z-traces through 0.5 μm polystyrene beads. The data was fitted using the 'fit single peak' function in Origin 8.1. The mean FWHM was calculated as 0.91 μm

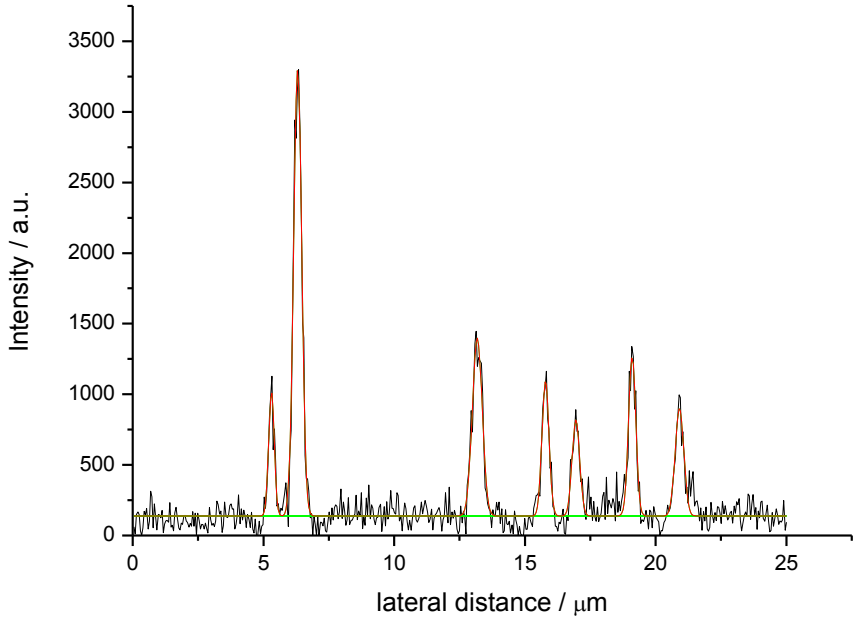

Figure 33 *xy* trace of TiO2 nanoparticles shown in black. Red line is the Gauss fit of the peaks whilst the green line is the calculated baseline.

3.3.2 Wavelength to wavenumbers

The wavelength of the pump and Stokes beams can be converted to wavenumbers for ease of comparison with the Raman shifts with the following formula:

$$wavenumber\ (cm^{-1}) = \frac{10^7}{wavelength\ (nm)}$$

4 Raman spectroscopy

Summary

Raman spectra were recorded for biological and chemical samples. These included polymers that will be used as experimental models, such as polystyrene, and those that are used in the construction of artificial joints or their fixation such as polyethylene and PMMA. Cellular constituents including lipids, proteins and nucleobases were measured, as well as whole cells. Cellular spectra were gathered mainly from fixed samples due to problems of keeping living cells under the laser beam for long enough time periods to record usable spectra. The spectrum of fixed cells was shown to be similar to to those of live cells.

Cells treated with polymeric particles showed differences in their Raman spectra with many peaks corresponding to the added particle being visible over control cell spectra. Raman mapping was also carried out on a sample cell containing phagocytosed particles illustrating the spatial information that can be obtained with Raman, however this technique took several hours to produce a low resolution map of a cell.

Peaks in the spectra obtained were identified by comparing with results published in the literature. Peaks were found to be within a couple of wavenumbers of these within the literature. Identifying these Raman active components will help us to identify Raman resonant frequencies to be imaged with our CARS setup and also help in interpretation of CARS images when tuned to these specific frequencies.

Although Raman can provide a wealth of information about a sample, the results show that the time factor to record this information is high, often ranging from minutes to hours for a single cell.

4.1 Raman spectra of materials

4.1.1 Ultrahigh molecular weight polyethylene

Polyethylene, as shown in Figure 34 A, is one of the simplest polymers, consisting of a repeating chain of CH_2 subunits. It appears much like a long-chained hydrocarbon and as such it contains a relatively simple Raman spectrum with sharp peaks as most bonds find themselves in similar environments.

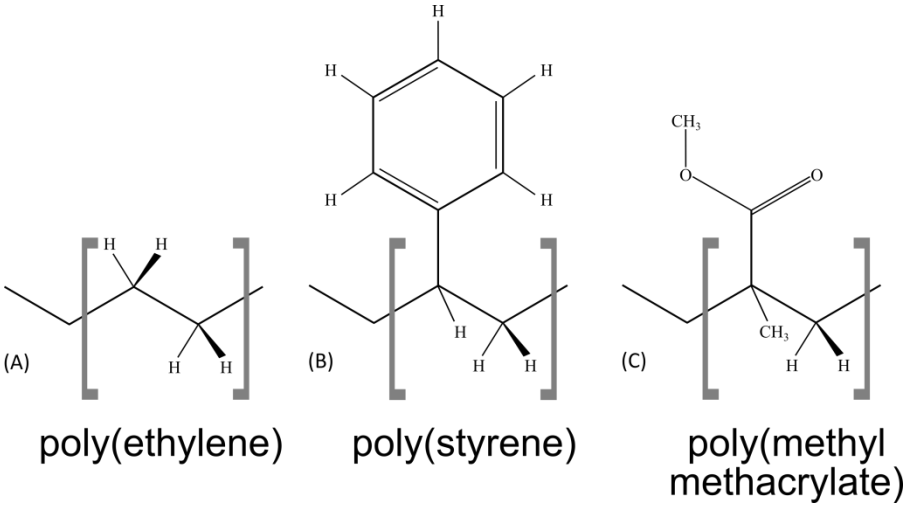

Figure 34 Polymers used in our investigation. A. Polyethylene is simply a long chain of repeating CH_2 subunits. B. In polystyrene one of the hydrogen atoms in the first CH_2 subunit has been replaced by a benzene ring. C. In PMMA both hydrogen atoms in the first CH_2 subunit have been replaced, a methyl group attached to one, and a methyl ester to the other.

The Raman spectrum of UHMWPE is shown in Figure 35. The spectrum contains several peaks both inside the fingerprint region and the C-H stretching region. The C-H stretching region is dominated by two fundamental vibrations: the symmetric and asymmetric C-H stretches which give peaks at 2847 and 2881 cm^{-1}. These peaks are superimposed on two second order peaks at 2886 and 2930 cm^{-1} that are highly dependent on the phase compositions (crystalline *vs* amorphous) as well as orientations of molecules in the material.[137] The small peak at 2722 cm-1 may be due to oxygen contamination.[138] The fingerprint region contains peaks at 1063, 1130, 1170, 1296, 1370, 1416, 1440 and 1463 cm^{-1}. The triplet of peaks at 1416, 1440 and 1460 cm^{-1} are caused by a combination of CH_2 scissoring and Fermi resonances. (Fermi resonances are due to the mixing of vibrational modes that share similar energy).[139] The 1370 cm^{-1} peak is due to CH_2 wagging whilst the 1170 cm^{-1} peak is

due to CH_2 twisting. The 1132 cm^{-1} and 1065 cm^{-1} peaks are due to the symmetric and asymmetric backbone C-C stretches respectively.[140,141]

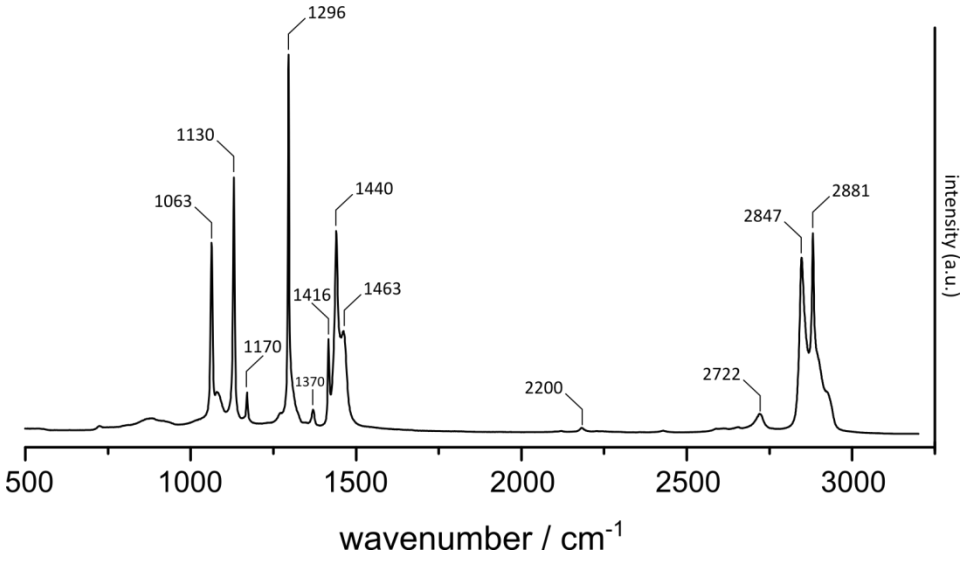

Figure 35 Raman spectrum of UHMWPE (GUR 1050 grade) showing the major vibrational peaks.

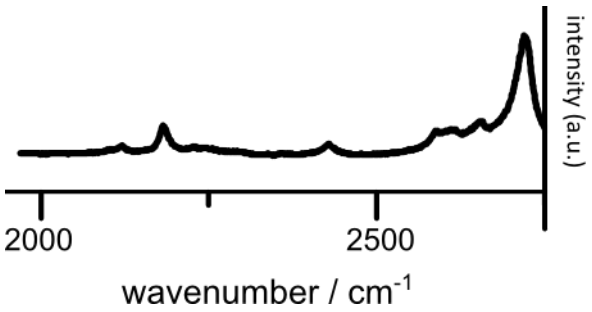

Figure 36 Zoomed in region of the 2000 – 2750 cm^{-1} region of Figure 35.

Figure 36 shows the Raman spectra in the silent region showing small peaks, which could be due to chain terminations and imperfections resulting in alkyne like peaks.[142]

4.1.2 Polystyrene

Polystyrene, shown in Figure 34 B, is superficially very similar to polyethylene with just one of the hydrogen atoms on the first CH_2 subunit replaced with a benzene ring. Because of the similarities the Raman spectra contains some shared features as shown in Figure 37. Peaks at 2847 and 2897 cm^{-1} are again due to the C-H stretches also found in UHMWPE. However, polystyrene also contains overlapped peaks at 3055 and 3067cm^{-1} due to the stretching of the C-H bonds on the benzene ring. The

backbone chain stretches are found in the 1100-1200 cm^{-1} region with the 1450cm^{-1} peak due to CH_2 scissoring.[143] These features are conformationally sensitive, depending on whether the benzene subunits are all aligned on one side, or are found on both sides of the molecule.[143] The benzene ring structure is responsible for a number of Raman modes, most notably is the large peak at 1004 cm^{-1} which is due to the deformation of the carbon ring structure. The nearby peak at 1032 cm^{-1} is due to in plane bending of the benzene C-H bonds. Another notable couplet is the peaks at 1583 and 1603 cm^{-1} which are again due to stretching in the benzene skeleton. Below 1000 cm^{-1} exists several peaks 541, 622, 758 and 906 cm^{-1} due to the various out of plane C-H bending modes. [143-145]

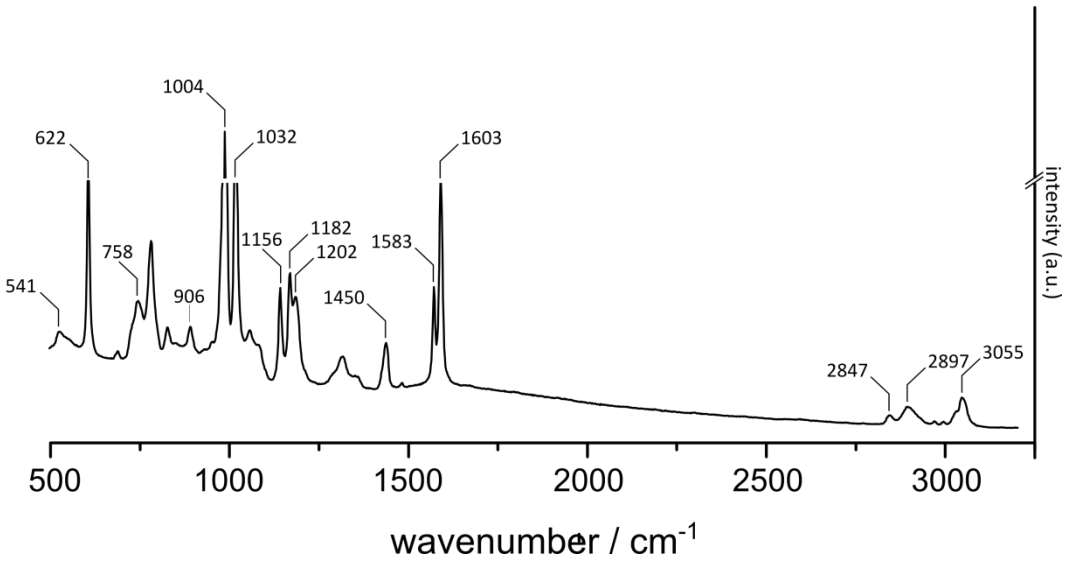

Figure 37 Raman spectrum of polystyrene showing the major vibrational peaks.

4.1.3 Polymethylmethacrylate

PMMA contains more alterations to the typical polyethylene structure than polystyrene does as both hydrogen atoms on the first CH_2 subunit have been replaced as shown in Figure 34 C. Figure 38 shows the spectrum obtained from PMMA. Both PMMA and polyethylene have peaks in the C-H stretch region which is perhaps the most easily comparable region. Compared to the C-H stretch region in polyethylene, the spectrum obtained from PMMA is complicated by Fermi resonances between C-H stretch fundamentals but can be broadly attributed to three peaks at 2843, 2953 and 3001 cm^{-1} which are due to symmetric and asymmetric stretching of the C-H bonds in the CH_2, O-CH_3 and C-CH_3 groups. The symmetric and asymmetric C-C

stretches of the backbone are found with peaks at the much lower 969 and 987 cm^{-1} and are joined by C-C deformations at 817, 1186 and 1247 cm^{-1}. The C=O stretching is responsible for the large peak at 1730 cm^{-1} and deformation of this bond is active at 843 cm^{-1}. The C-O stretching coupled with methyl rocking is found at 1123 and 1160 cm^{-1} whilst the O-C=O deformations are responsible for peaks at 559, 604 and 737 cm^{-1}.[146,147]

Figure 39 shows overlaid spectra from the three polymers for ease of comparison.

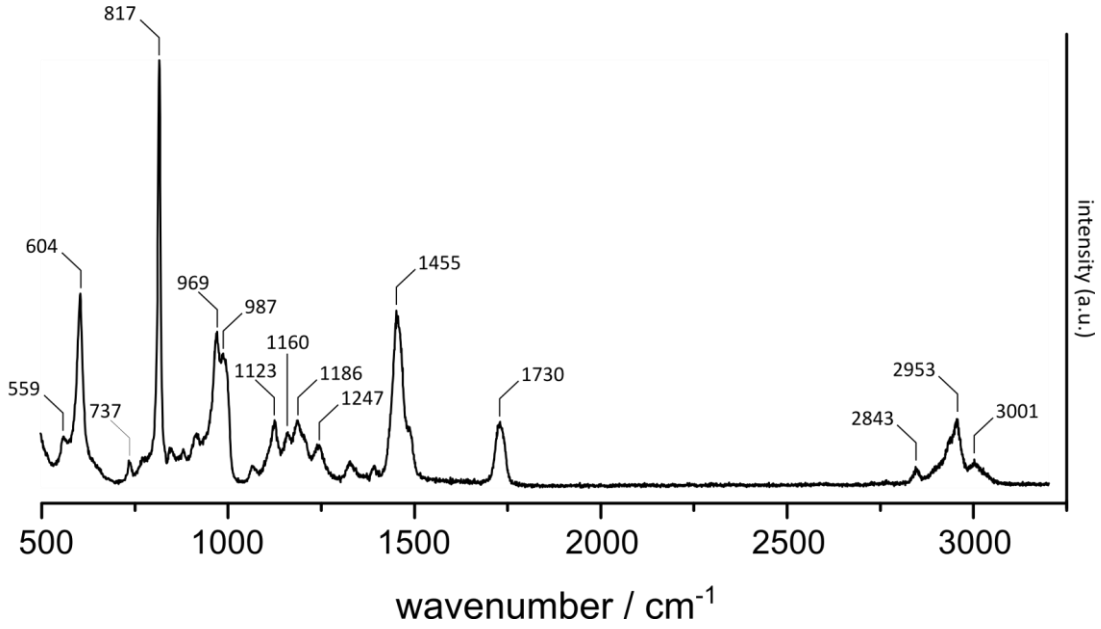

Figure 38 Raman spectrum of PMMA showing the major vibrational peaks.

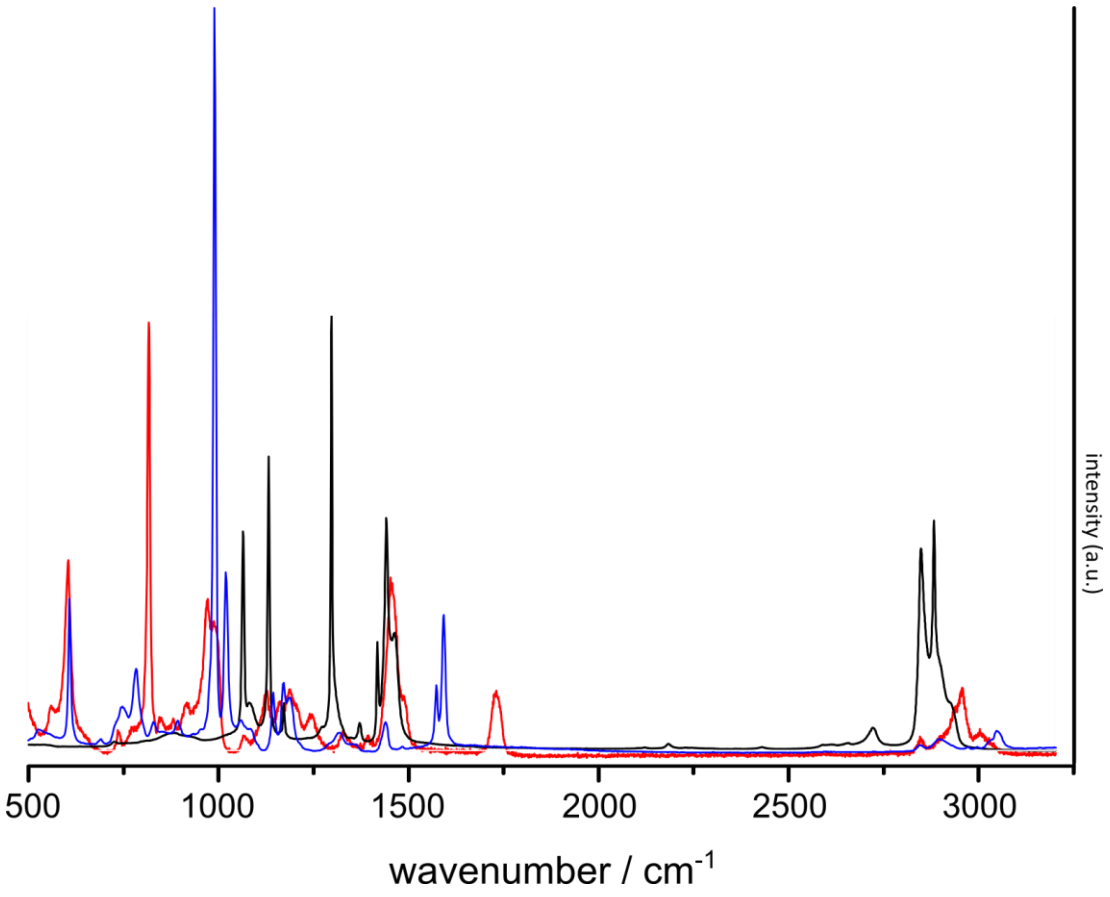

Figure 39 Overlaid Raman spectra of UHMWPE (black), polystyrene (blue) and PMMA (red).

4.2 Raman spectroscopy of biological molecules

4.2.1 Lipids

Lipids are a large group of biological molecules that are categorised by their hydrophobic nature, and include waxes, sterols, triglycerides and phospholipids. Figure 40 shows a diagram of a typical phospholipid, 1,2-dipalmitoylphosphatidylcholine (DPPC). The structure contains two long, fatty acids that mainly consist of saturated carbon chains attached to a phosphate head group by a glycerol chain.

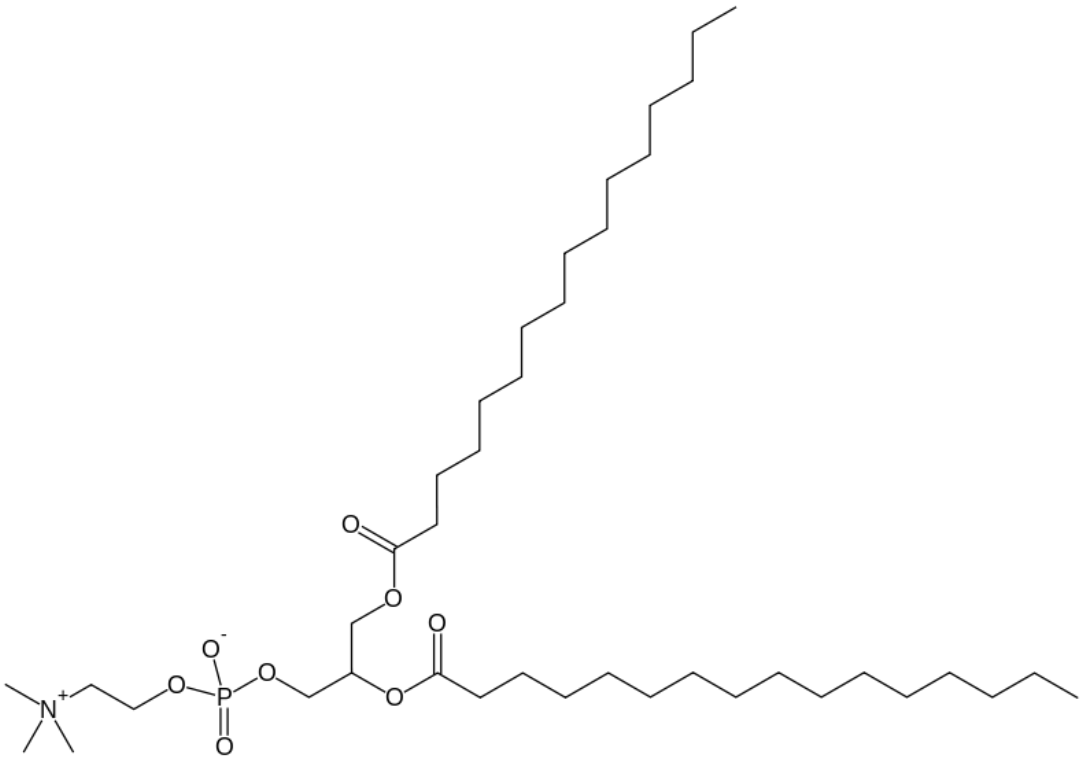

Figure 40 Diagram of DPPC.[‡]

Because of the similarity between the fatty acids and polyethylene we expect to see many similar peaks in the Raman spectra of lipids (shown in Figure 41) compared with polyethylene. In the C-H stretching region we see the two peaks for symmetric and asymmetric CH_2 stretches repeated at 2845 and 2880 cm^{-1}. In addition there appears a small shoulder, consisting of peaks at 2928 and 2972 cm^{-1} due to symmetric and asymmetric methyl stretches of the fatty acid chains. The CH_2 scissoring peaks are repeated at 1435 and 1456 cm^{-1} whilst the in plane CH_2 twisting is found at 1294 cm^{-1}. The C-C stretches are found as peaks at 1061, 1096 and 1127 cm^{-1}. Due to the additional bonds involved there are many unique peaks found in the DPPC spectrum including the C=O stretch which appears as a broad peak around 1730 cm^{-1}. The acyl stretching modes appear as peaks around 845 cm^{-1} and the C-N stretch is found at 715 cm^{-1}. The phosphate stretching peak is found mixed in with the carbon backbone stretches.[148-152]

[‡]http://en.wikipedia.org/wiki/File:Dipalmitoylphosphatidylcholine.svg

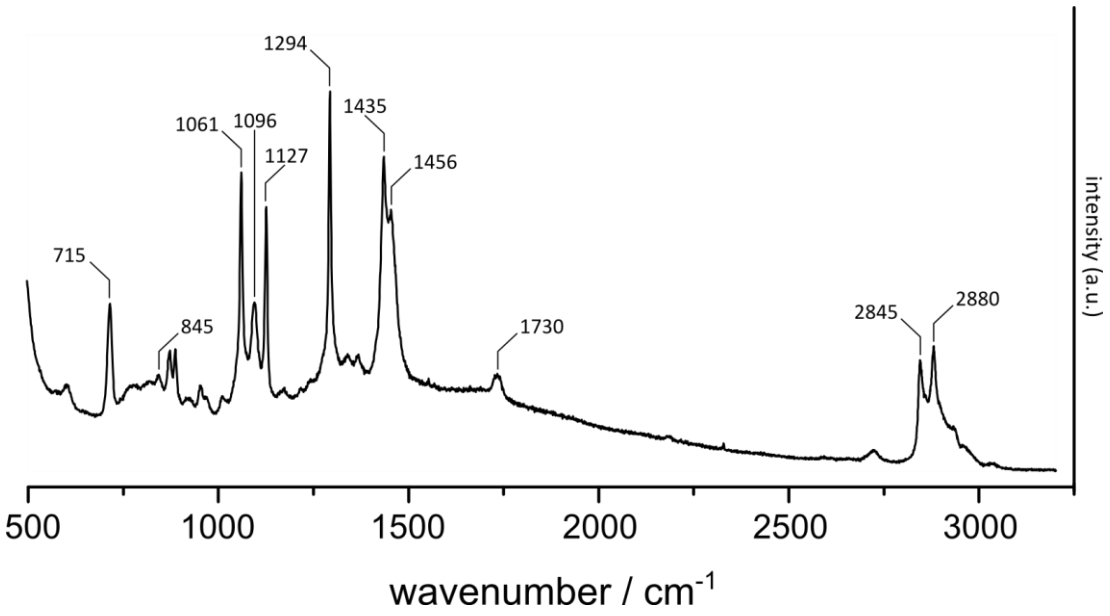

Figure 41 Spectrum of DPPC showing the major vibrational peaks.

4.2.2 Nucleobases

The spectra of the four different nucleobases offer a glimpse of the sensitivities of Raman vibrations on the surrounding chemistry. The in-plane ring stretching vibrations are highlighted in Figure 42 and can be found at shifted frequencies in each of the four compounds. In adenine and guanine, the two purines have the vibrational frequencies centred at 724 and 651 cm^{-1} respectively. The two pyramidines, cytosine and thymine, have theirs at 793 and 743 cm^{-1}. [153]

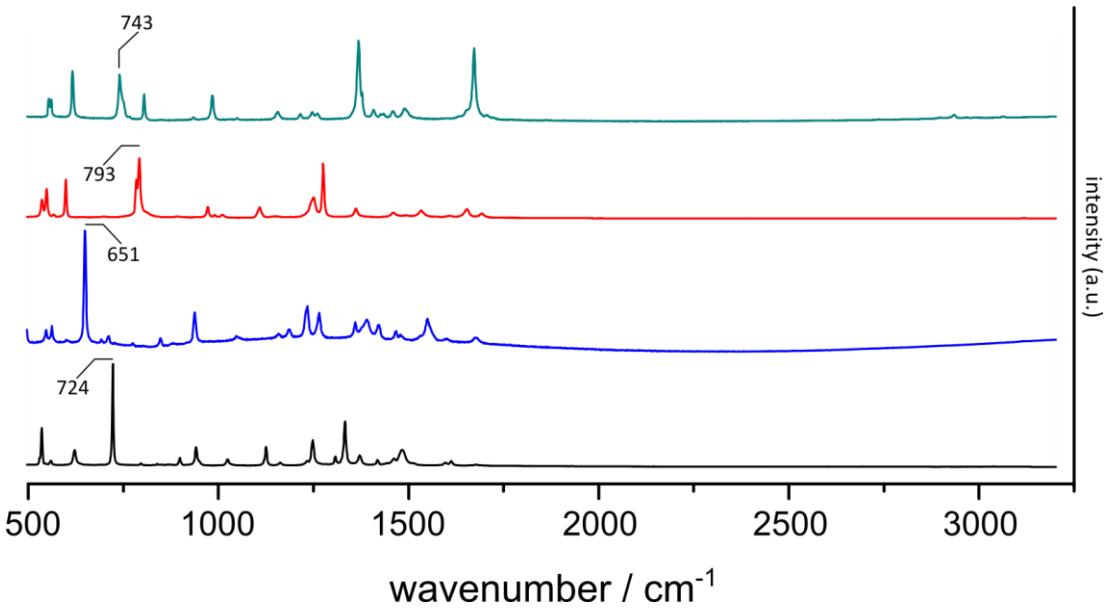

Figure 42 Raman spectra the four nucleobases: adenine (black), guanine (blue), cytosine (red) and thymine (teal) offset for ease of reading. The in-plane ring stretches are marked out and the spectra are offset for clarity.

4.2.3 Proteins

Proteins are made up of long chains of amino-acids linked together by amide bonds folded up into their own 3D shapes. In eukaryotes, up to 21 different amino acids are being used as building blocks, each with their own unique side chain. As such each protein contains many different chemical bonds in different abundances depending on its composition. Figure 43 shows the spectra of two different proteins, BSA and immunoglobulin G. A notable feature of the protein Raman spectrum is that many of the peaks are very broad instead of sharp as found in many of the polyethylene peaks. This is typically seen best in the amide I (C=O stretching vibrations) and amide III (mixture of C-N bond stretching and in-plane N-H bond bending) bands which appear as broad peaks around 1660 and 1250 cm^{-1} respectively. Differences in the primary structure as well as the secondary structure alter the energy required to excite these vibrational modes. A secondary structure dominated by β-sheets contains peaks at 1240 and 1650 cm^{-1} whilst those dominated by α-helices contain peaks at 1298 and 1653 cm^{-1}.[154,155] In our protein examples we can see the clear differences in the amide I peak, with immunoglobulin G containing a large peak at 1240 cm^{-1}

indicating that the structure is mainly β-sheets, which agrees with the x-ray crystallography data.[156,157]

The protein Raman spectrum also contains the typical features that we have come to expect, with the 2800 to 3000 cm^{-1} containing CH_2 and CH_3 stretching peaks as well as the 1420 and 1450 cm^{-1} CH_2 and CH_3 deformations. C-C stretching in the backbone and in the side chains are responsible for peaks at 902, 947, 1103 and 1127 cm^{-1}. The other notable feature of the protein Raman spectra is the peaks caused by aromatic side chains, particularly tyrosine and phenylalanine. Phenylalanine is responsible for the large peak at 1003 cm^{-1} as well as a smaller peak at 1604 cm^{-1} whilst tyrosine contributes towards peaks at 1210 and 1615 cm^{-1}. A small peak at 3060 cm^{-1} is due to the C-H stretching of the aromatic rings.[158,159]

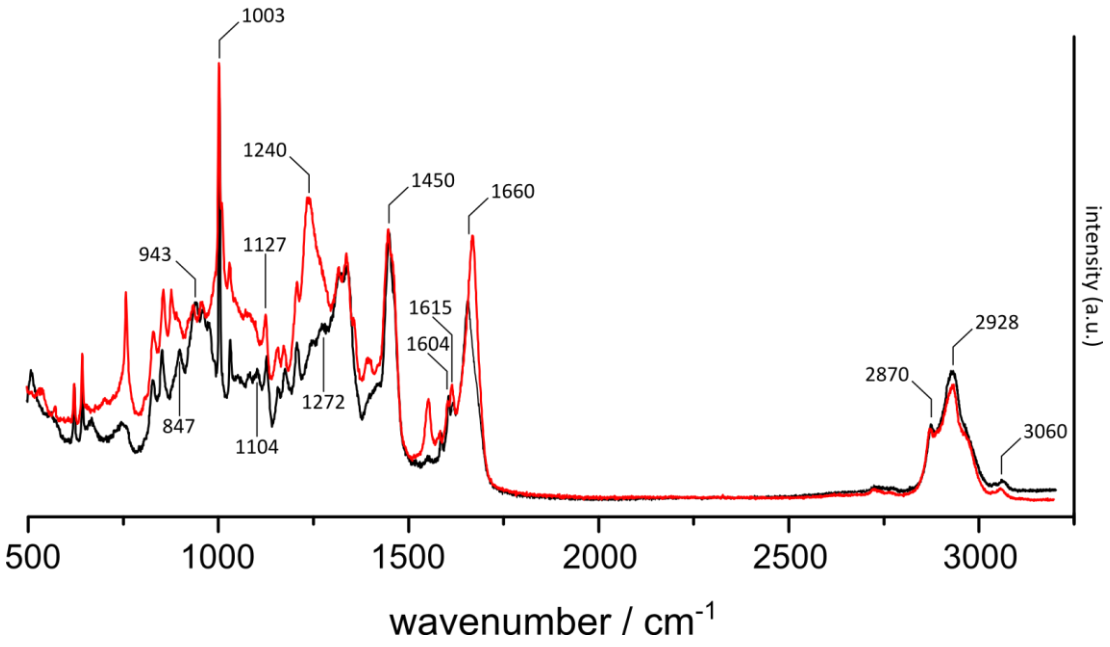

Figure 43 Raman spectra of protein samples, BSA (black) and immunoglobulin G (red) showing selected vibrational peaks.

4.2.4 Living and fixed cells

We found it necessary to examine whole cell samples for long time periods (10 minutes or more) to generate data that had a sufficient signal over background noise. This background noise can be due to thermal noise as well cosmic rays, and also spurious background light hitting the detector. However, we also found that long scan times with the laser would ablate the samples before scanning was completed. A

chemical fixative was added to the cells in an effort to improve the sample stability, preventing movement of the cell under the laser. This allowed more spectra to be collected as more samples 'survived' the process.

A five minute treatment with 0.1% solution of glutaraldehyde in PBS was used to fix cells. Glutaraldehyde is a small molecule, capable of diffusing throughout the cell in a matter of minutes. Each molecule contains two aldehyde groups that are capable of cross linking structures via condensation reactions which helps to preserve the cell structure whilst making it immobile.[160] A comparison of the Raman spectra of live and fixed cells are shown in Figure 44. In this example the spectra were recorded by a 20× objective and a 30 second scan time with multiple accumulations.

Although many of the following cell spectra are from the same type of cell, it should be noted that the macrophage cell is a catchall term for many different cells that carry out very different functions. Not only are there inter-population differences between macrophages collected from different sites, but intra-population differences exist as well.[161] These differences, along with cells being in different stages of the cell cycle may show up in Raman spectra.

In Figure 44 it can be seen that both spectra contain similar peaks found at the same wavenumbers. The cell spectra contain a much broader hump, possibly due to unwanted fluorescence by components of the culture medias that they are kept in. In both live and fixed cells it can be seen that the major peaks that had been previously observed for both proteins and lipids are again visible and there is little differences between the two spectra. The C-H stretch region from 2800 to 2900 cm^{-1} consists of a mixture of the sharp peaks, as seen in the lipid spectrum (Figure 41) and the broad peaks seen in the protein spectra (Figure 43). The amide I and III stretches at 1658 and 1265 cm^{-1} show up strongly, as does the CH_2 deformations around 1448 cm^{-1}. The ring breathing of phenylalanine appears as a sharp peak at 1004 cm^{-1}.

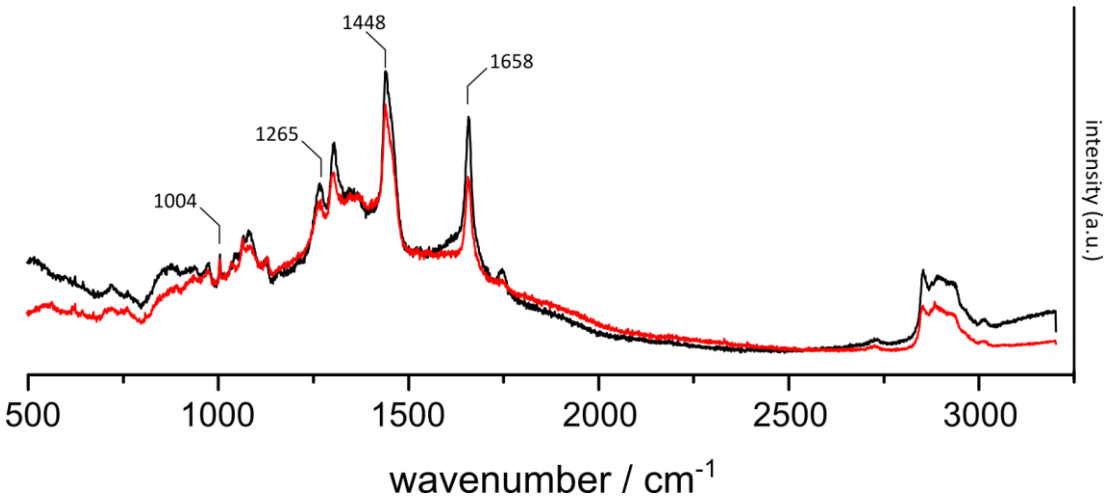

Figure 44 Raman spectra of fixed monocyte derived macrophage cells (black) and live cells (red) showing selected vibrational peaks.

4.2.5 Nucleus and cytoplasm measurements

Using a 50x objective it is possible to gather Raman spectra from targeted areas of the cell. Using fixed cells that had been dried, a 30 second exposure time and 6 accumulations with cosmic ray removal, we recorded spectra with the laser focused on different parts of the same cell. These could be visibly identified as the nucleus or cytoplasm and they are shown in Figure 45. The main differences in the Raman spectra are found in peaks relating to DNA. The nuclear spectrum contains particularly strong signals in the DNA backbone stretch at 830 cm^{-1} as well as larger peaks from the in-plane ring stretching vibrations at 670, 720, and 770 cm^{-1}.[162]

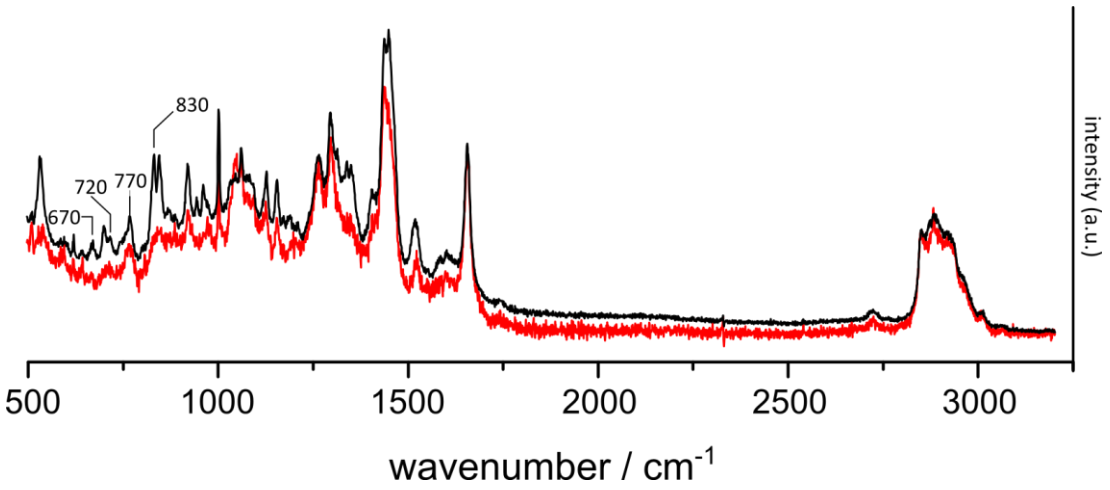

Figure 45 Raman spectra of the nuclear region (black) and cytoplasmic region (red) of a fixed macrophage cell. The main differences appear to be the bigger peaks that are typically associated with DNA.

4.2.6 Comparison of cell types

We compared the Raman spectra of three different cell types: monocyte derived macrophages, RAW 264.7 mouse macrophage and NIH 3T3 fibroblasts. These spectra are shown in Figure 46 and were recorded from glutaraldehyde fixed cells, using a 20× objective, a 30 second exposure with 6 accumulations. The notable difference is the stronger contribution of lipid-like peaks to the Raman spectra of the primary macrophage cell. Peaks that are typically associated with lipids 1170, 1295, 1460, 2850 and 2880 cm^{-1} all appear much stronger than in the two cell lines suggesting a much higher lipid content. Otherwise many of the core features such as the protein peaks are found to be similar in all three spectra.

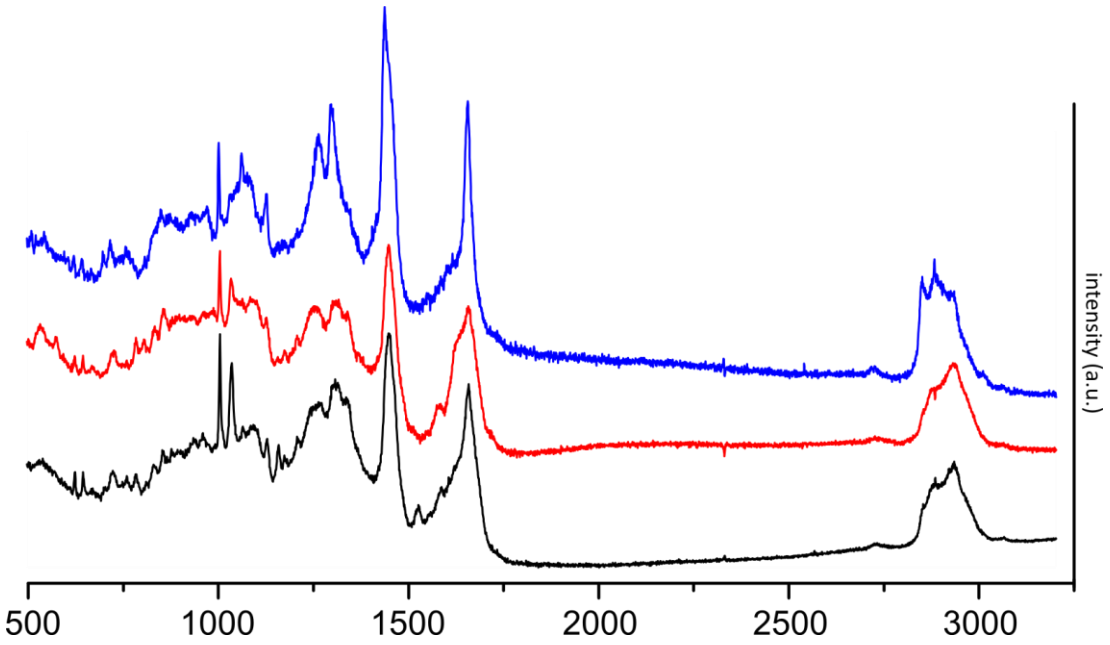

Figure 46 Raman spectra for NIH 3T3 fibroblasts (black), RAW 264.7 mouse macrophages (red) and human monocyte derived macrophages (blue). Spectra offset for clarity.

4.2.7 Cells with added polyethylene and polystyrene

We added commercial polyethylene particles (mean size 5 μm) and polystyrene particles (mean size 1.1 μm) to cultures of Raw 264.7 macrophage cells. After 24 hours the cells were fixed in glutaraldehyde and then washed in PBS and then water. Raman spectra were then recorded (shown in Figure 47) using a 20× objective, 30 second scan time with 6 accumulations. Cosmic ray removal was also carried out in the software.

With the cell pre-incubated with polystyrene, the Raman spectrum included peaks not founded in a control cell. The most obvious of these is the peak at 3060 cm^{-1} which represents the C-H stretch in the benzene ring. Although this stretch exists in some amino acids (phenylalanine and tyrosine) in proteins, they do not appear to be large enough concentration to generate a measurable signal in the cell spectra. The pair of peaks at 1580 and 1600 cm^{-1} that correspond to the benzene skeleton stretching also stand out on the shoulder of the amide I stretch. The phenylalanine ring peak is now dwarfed by the pair of peaks from the polystyrene ring breathing and in plane stretching at 1004 and 1032 cm^{-1}.

The Raman spectrum of a cell with added polyethylene contains many peaks corresponding to the polystyrene Raman spectrum. In the fingerprint region the 1060, 1129, 1294, 1416, 1441 and 1460 cm^{-1} peaks are clearly visible. In the C-H stretch region the polyethylene peaks of 2850 and 2880 cm^{-1} stand out on the broad peak coming from the cell.

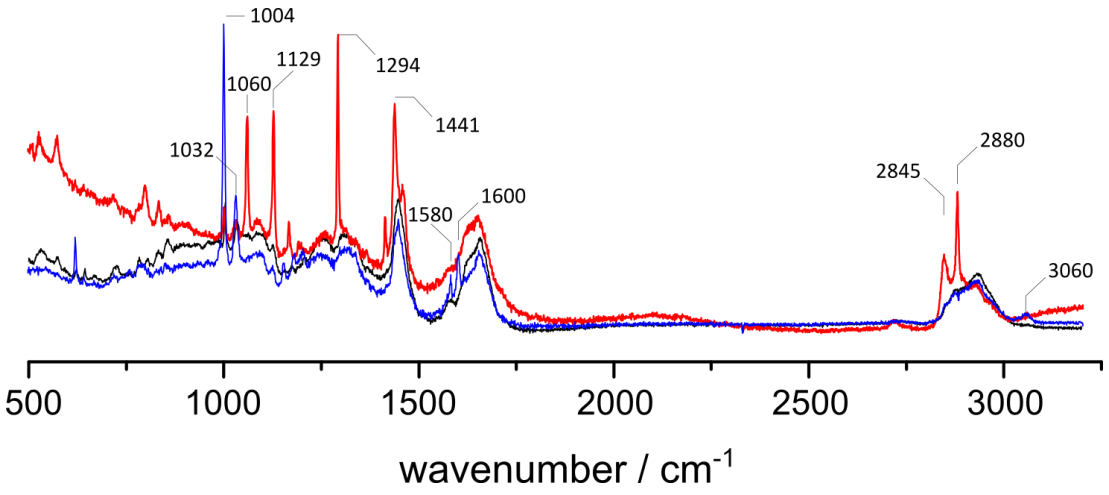

Figure 47 Raman spectra of RAW 264.7 cells. Control cell (black), cell with added polyethylene (red) and added polystyrene (blue). Peaks from the added materials are highlighted.

4.3 Raman mapping

With a high powered objective lens (50×) and the automated Raman software it is possible to take Raman spectra at many different points over the cell. Each data point on the cell corresponds to a complete Raman spectrum. Using a monocyte derived macrophage that had been treated with polystyrene microspheres (mean size 1.1 μm) we recorded mapped spectra at the points shown in Figure 48 A. This was a time consuming process given that each point took around 10 minutes to record and 55 data points were recorded across the cell surface of a cell fixed in glutaraldehyde. By taking the magnitude of the polystyrene ring C-H stretch at 3060 cm^{-1} from each of the data points we constructed a contour plot that is shown in Figure 48 B. The reconstruction shows an area of high signal coming from the lower left hand quadrant, indicating that one or more polystyrene beads are present. As the entire spectrum is recorded at each point, it would be possible to illustrate many other different features of the cell by tracking different peak sizes or ratios. Spectra from along the black line of Figure 48 B are shown in Figure 49 C. The presence of the

polystyrene peaks superimposed on the background of the cellular spectra can be easily seen.

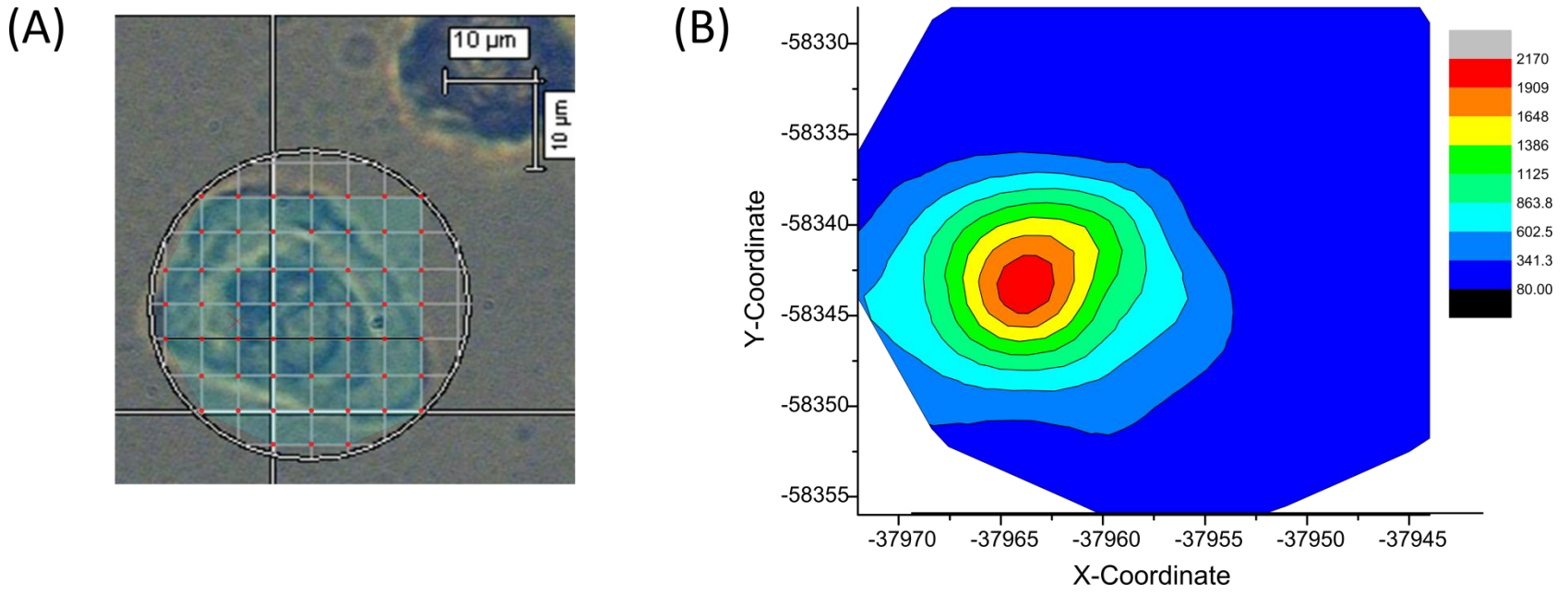

Figure 48 A Raman map of a cell is recorded. A. Light microscope image of the area, grid line intersections (marked by red dots) show the points at which spectra were recorded. B. Contour map showing the magnitude of the 3060 polystyrene ring C-H stretch. The red X in A. Marks the approximate location of the maximum location marked in B.

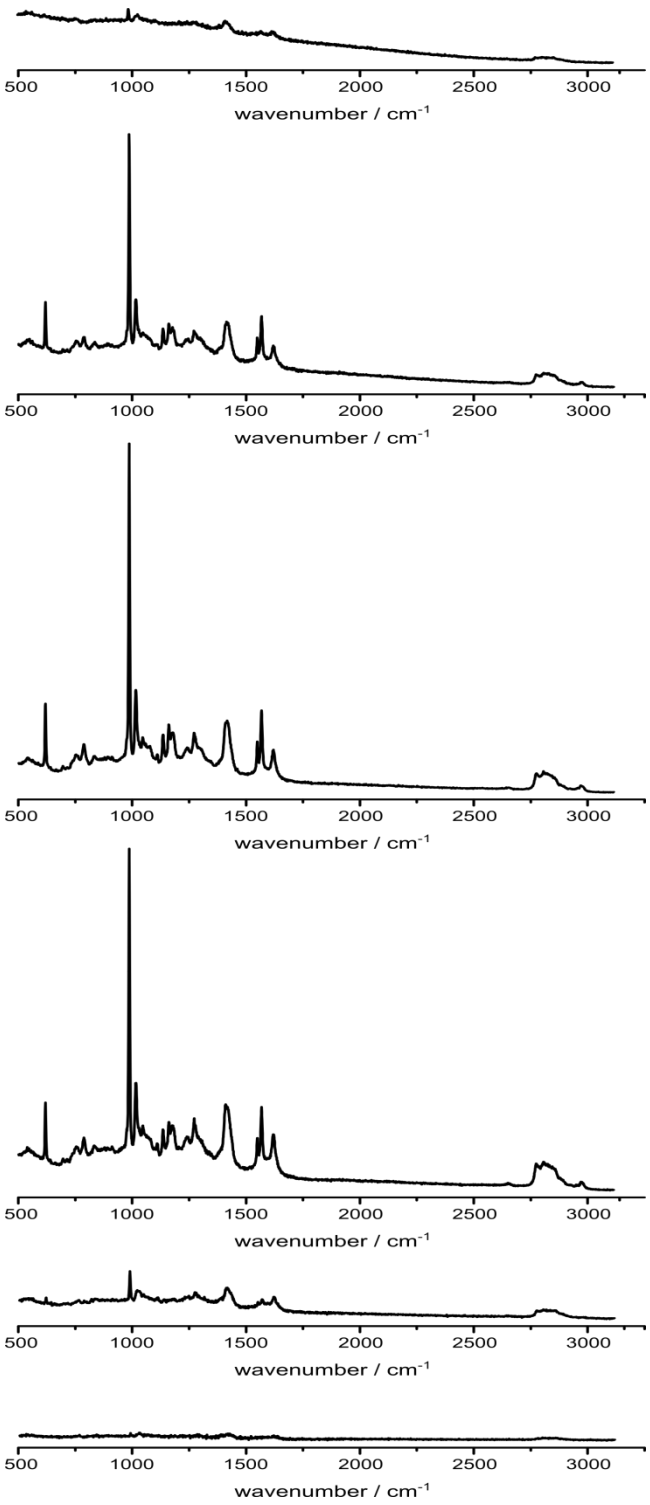

Figure 49 Raman spectra taken from left to right along the black line in Figure 48 shown top to bottom.

4.4 Conclusions

Raman spectroscopy is a powerful tool for studying the chemical composition of samples, with even closely related chemicals having very different spectra. However, as the chemical composition becomes more complicated, such as those of living cells, it can be difficult to understand how changes to single Raman spectra relate to changes in the cell composition. Although it is possible to use Raman to gain spatial information from a cell sample, this is a slow process, taking many hours and is clearly not suitable for studying living cells.

The Raman spectrum of polyethylene contains many of the same peaks as that of cell lipids, due to the similarity of polyethylene and saturated fats. This may present a challenge when imaging cells where CARS signals will be generated from both lipids and polyethylene when exciting the sample at known polyethylene bond resonances. However, our data also shows that polystyrene should prove to be a useful model particle to work with due to presence of Raman peaks at wavelengths not seen within the cell.

A possible solution to the similarity of the Raman spectra of lipids and polyethylene is to deuterate one of the compounds. Carbon-deuterium stretching vibrations show up in the 2000-2400 cm^{-1} region rather than the C-H stretching region at 2800-3000 cm^{-1} region.[163]

5 Particle sizing

Summary

Retrieval studies from tissues in the periprosthetic region have shown that the majority of particles found are under 0.5 μm in size. This coincides with the size range of particles that is thought to be the most biologically active. We were interested in the sizes of particles generated by our own wear tester, as well as our method of retrieval and set about analysing the particle size using FEG-SEM.

We demonstrated our method for sizing particles by first using commercial polystyrene particles before moving onto polyethylene particles. Our polyethylene particles came from a wear simulator that was capable of running with two different wear loading configurations. One pattern had the wear pins move in a linear motion with dynamic loading, whilst the other used an elliptical motion with dynamic loading. We found that particles generated by the elliptical loading pattern were more numerous and smaller than particles generated from the linear loading pattern. The particles generated by elliptical loading also resembled the particles retrieved from *in vivo* experiments more accurately than the linear wear particles.

5.1 Filtration

We used triple filtered water to test the level of contamination in our filtering. The water was filtered through polycarbonate filters and subsequently viewed using electron microscopy. The membrane filters appeared clear from contaminating particles at all magnifications tested as shown in Figure 50.

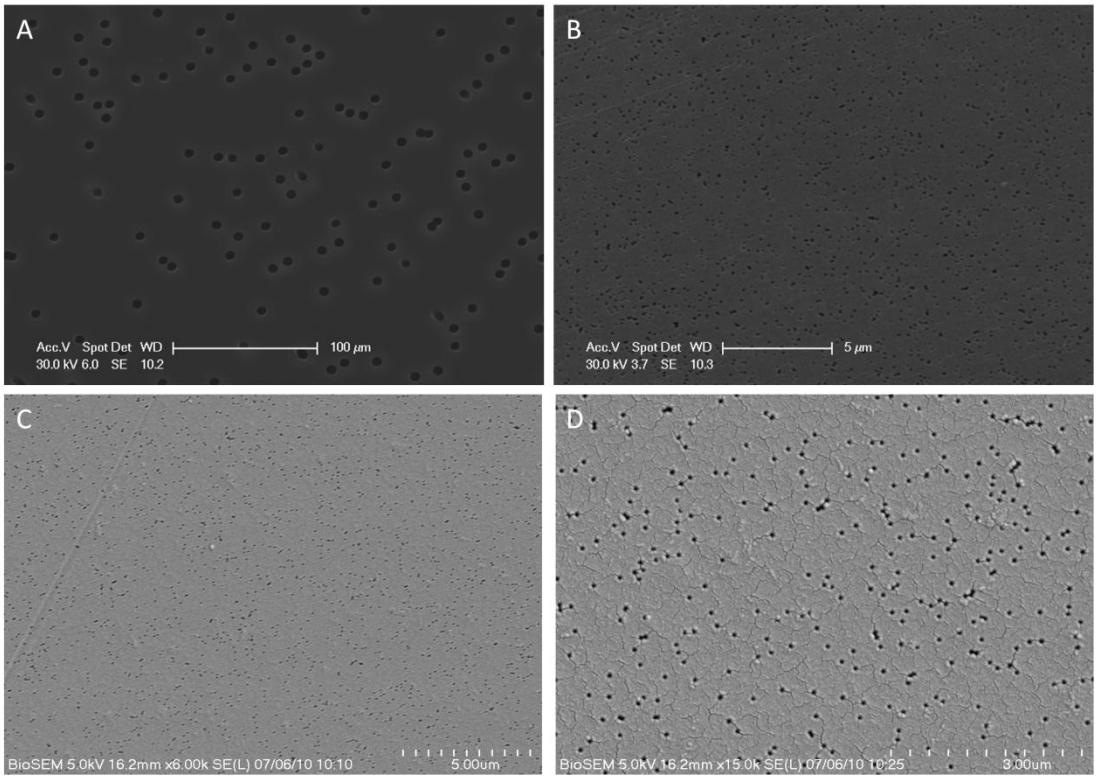

Figure 50 Triple filtered water was used as a negative control for the electron microscopy analysis. A. 8 µm polycarbonate and B. 0.2 µm polycarbonate filters under SEM. C. and D. 0.1 µm polycarbonate filters under FEG-SEM at 6,000× and 15,000× magnifications all appear clear from contaminating particles.

5.2 Polystyrene particles

Using commercially available polystyrene particles we are able to demonstrate and evaluate the techniques used for our particle sizing. We used a polyethylene suspension labeled as 1.1 µm particles that are described in the specification sheet as having a size range of 1.0 to 1.2 µm.[164] Figure 51 shows an electron microscope image of the polystyrene particles. The image shows that there are small variations in

the size of these spheres. The marked sphere measures 1.85 µm in diameter, which clearly in excess of the manufacturers stated size range.

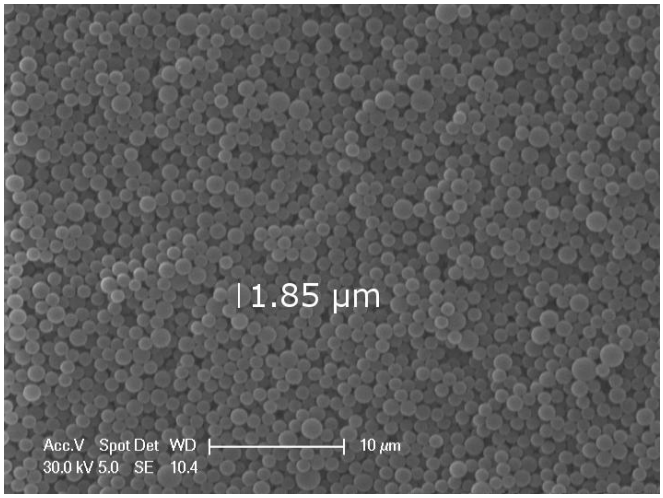

Figure 51 1.1 µm polystyrene spheres on a 0.2 µm polycarbonate filter. The size of the marked sphere is almost 54% larger than the manufacturers stated maximum size.

The process used to measure particles size on polystyrene particles is illustrated in Figure 52 and is as follows:

- Figure 52 A. The image taken from the electron microscope.
- Figure 52 B. The overlaid text from the SEM image is cropped out of the picture as it may obscure particles found underneath.
- Figure 52 C. A mask of the image is than created, highlighting the areas where particles are present. This can be done automatically by removing the darker coloured filter background (known as thresholding), but often the regions of interest must be manually highlighted if there is not sufficient contrast between particle and filter.
- Figure 52 D. The mask is then used to cut out only the particles of interest from the original SEM image.
- Figure 52 E. Although some of the particles are isolated, many of them are found touching one another. To calculate accurate single particle sizes they need to be separated. A watershed function (which attempts to separate the boundaries of two topographical regions) or manual line drawing help to separate particles from one another. It is also noted at this stage that some

particles are hidden underneath others and may be removed manually rather than leaving them in which may give erroneously small sizes.

Figure 52 F. Finally, the ‘analyze particles’ function is selected from within ImageJ. The separation of particles from one another can be checked using the image of the particle outlines where each particle is individually numbered. Particles on the edge of the screen are excluded as it would be unclear how much more of the particle is outside the field of view. The ‘analyze particles’ function returns a number of user selectable parameters. In our case we are interested in the equivalent circular diameter (ECD). These results are shown as a histogram in Figure 53.

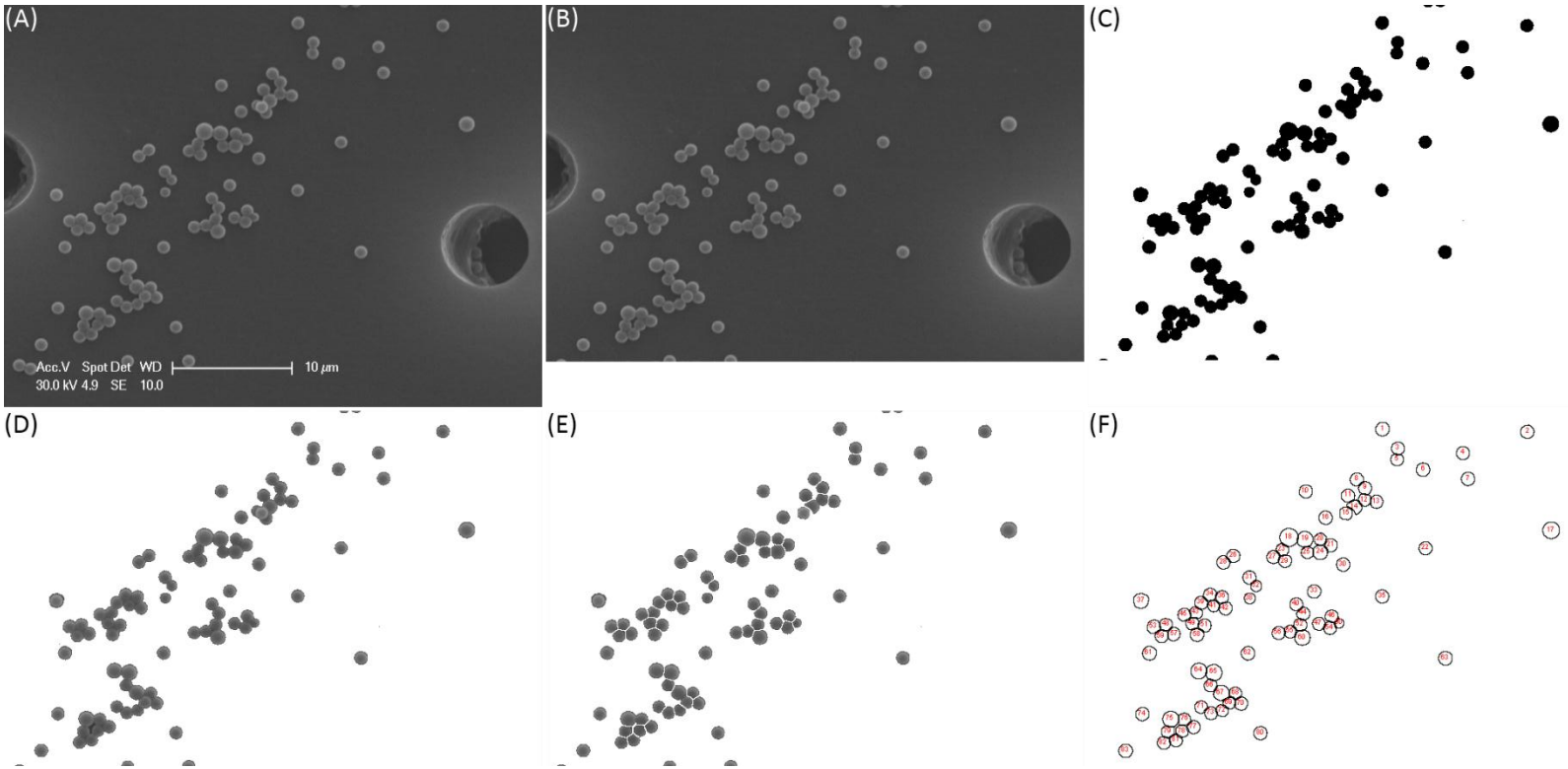

Figure 52 The imaging process to calculate the size of particles from SEM pictures. A. The SEM picture. B. The text from the bottom of the image is removed. C. A mask is created from a combination of computer thresholding and manual brush work highlighting the particles on the filter. D. The mask is used to isolate particles from the background of the image. E.A watershed function is applied and manually altered to separate touching particles. F. Finally the image is suitable for computer analysis, every particle is numbered, and the size and shape of each particle is recorded.

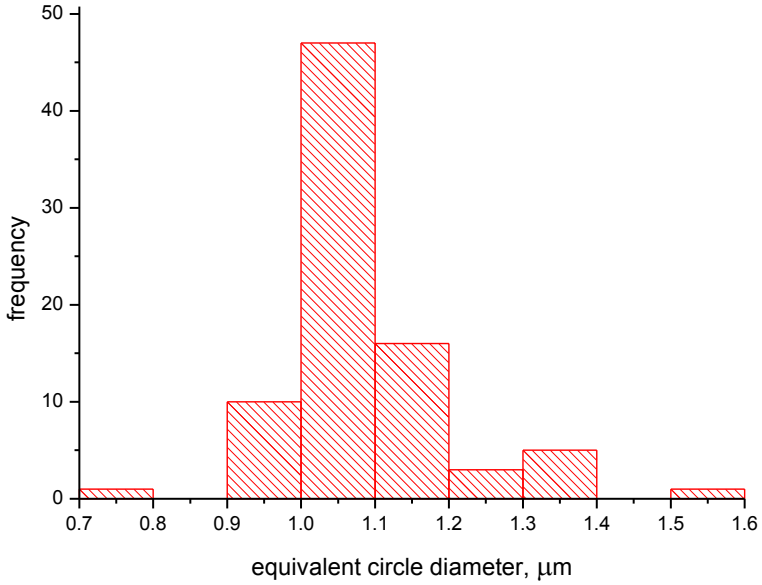

Figure 53 Histogram showing the particle size distribution of 1.1 µm latex spheres.

5.3 Ultra high molecular weight polyethylene

UHMWPE particles isolated from a pin-on-plate wear simulator using the protocol in Chapter 3.1.3. Wear particles produced using either a linear or elliptical pattern of motion[165] were analysed by SEM in a similar fashion to polyethylene. The polyethylene used was a 10 MRad crosslinked polyethylene. Elliptical debris was taken from serum extracted between 2.5 million and 2.75 million cycles whilst the linear debris was collected between 2.25 and 2.5 million cycles.

5.3.1 Linear wear debris

Particles were only found on the 10 µm filters after extensive searching. The particles found were mostly chunk like in nature, with sharp angles as shown in Figure 54 C and D. The largest size of particle that we recorded for the linear wear debris was 50 µm in length. However, so few particles were found that it would be hard to draw any definite conclusions about the nature of the larger wear particles apart from the fact that they were very infrequent compared to the smaller wear debris.

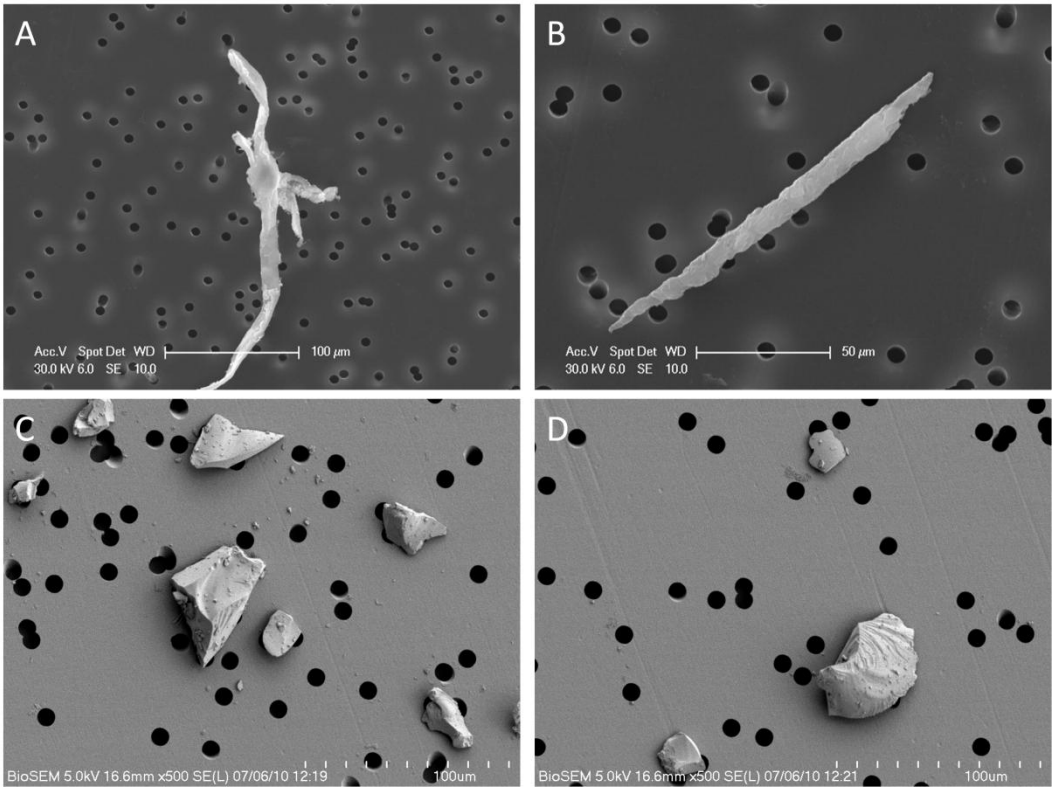

Figure 54 SEM images of UHMWPE particles found on 10 μm polycarbonate filters. A and B. show long, needle like particles found in the elliptical wear debris. C and D. show the angular blocks that were more commonly found in the linear wear debris.

Linear wear debris was found to be much more abundant on the smaller pore size filter. Four example fields of view captured by the electron microscope and used in our particle size analysis are shown in Figure 55. The debris found was dominated by flake like particles around one to two microns in length; smaller cubic particles were also seen on the filter. Eight fields of view at two different magnifications were found using random searches. Particle size data from these images were pooled together for the histogram in Figure 56. The linear particles were found distributed in a positively skewed normal distribution. The mean size of the particles measured was 0.995 μm ± 0.649 μm, much larger than the elliptical particles (c.f. a mean of 0.289 μm ± 0.211 μm in chapter 5.3.2). An average of 0.0336 particles were found per μm^2 on the filter, possibly indicating that the wear rate was greatly reduced compared to the elliptically generated wear debris (1.17 particles found per μm^2), which would agree with the gravimetric analysis performed on these samples.[165]

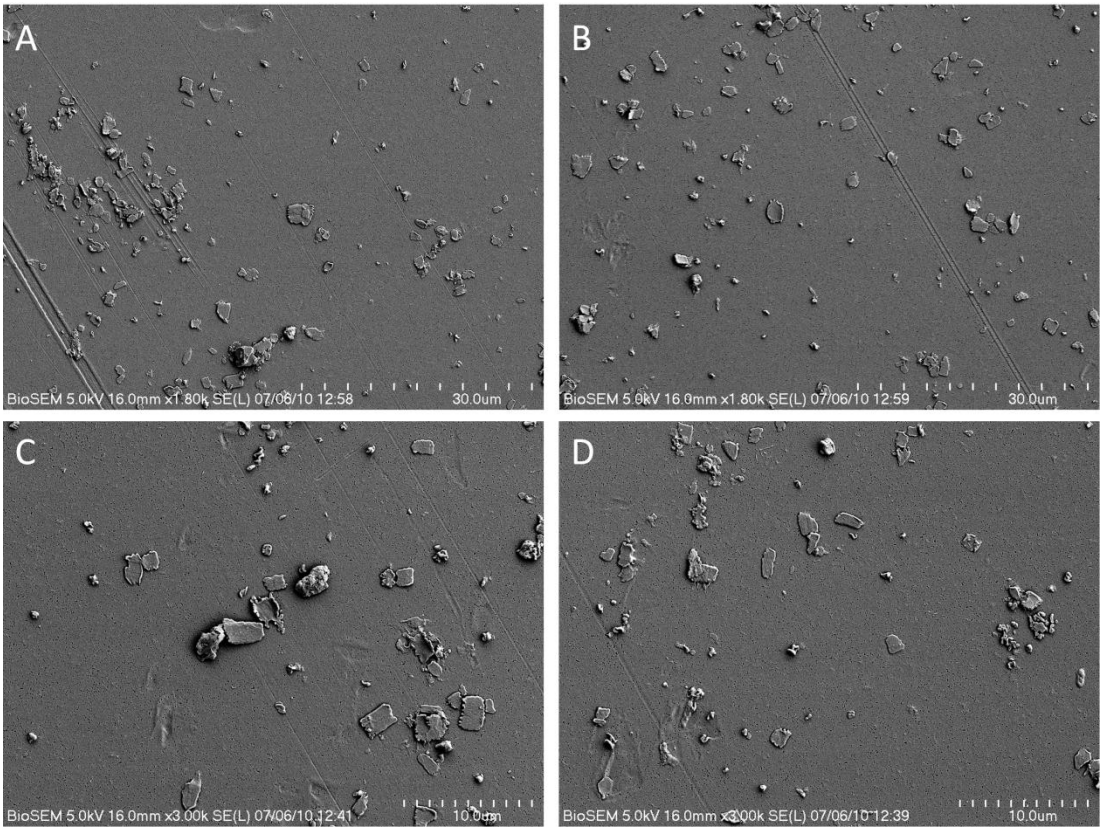

Figure 55 Wear debris from a linearly oscillating pin-on-plate simulator. A and B. show 1800× magnification images whilst C and D. show 3000× magnification images.

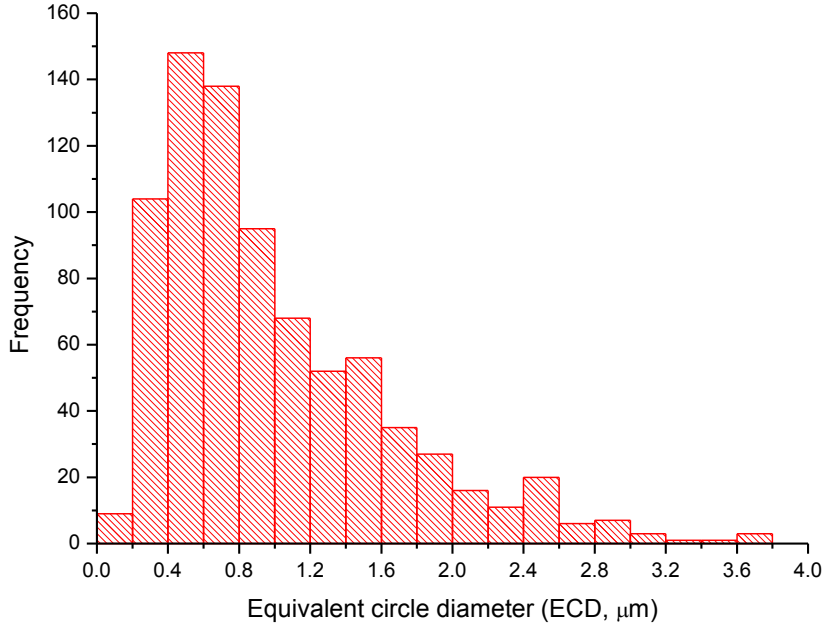

Figure 56 Histogram representing the distribution of polyethylene particles found on 0.1 µm polycarbonate filters from a linearly oscillating pin-on-plate wear simulator. The data was taken over an area 23,800 µm^2.

5.3.2 Elliptical wear debris

As with the linear wear debris, very few elliptical wear particles were found on the 10 μm filters. The particles found included more needle like particles and included particles up to 200 μm in length. (See Figure 54 A and B for example). So few particles were found it would be hard to draw any conclusions from this.

The 0.1 μm filters were found to be covered with particles and random searches were used to find areas to record images from for further analysis. At a magnification of 1,100×, the elliptical filters contained chunk like, angular particles a few microns in length scattered throughout the image as shown in Figure 57 A. At higher magnifications, as shown in Figure 57 B and C, it can be seen that hundreds of submicron sized particles covered the filter which were not possible to visualise with accuracy in the lower magnification images. Unlike the micron sized particles these sub-micron particles were often more rounded and smoother in nature which can be more clearly seen in the high magnification image in Figure 57 D. Particle sizes were measured from a total of eight fields of view split between four high (5000×) and four low (1100×) magnifications. In the four low magnification images only particles of over 1 μm in size were considered in the low magnification images due to the difficulties of visualising the smaller particles. However these images help to confirm that the particle distribution is not unevenly weighted with larger particles.

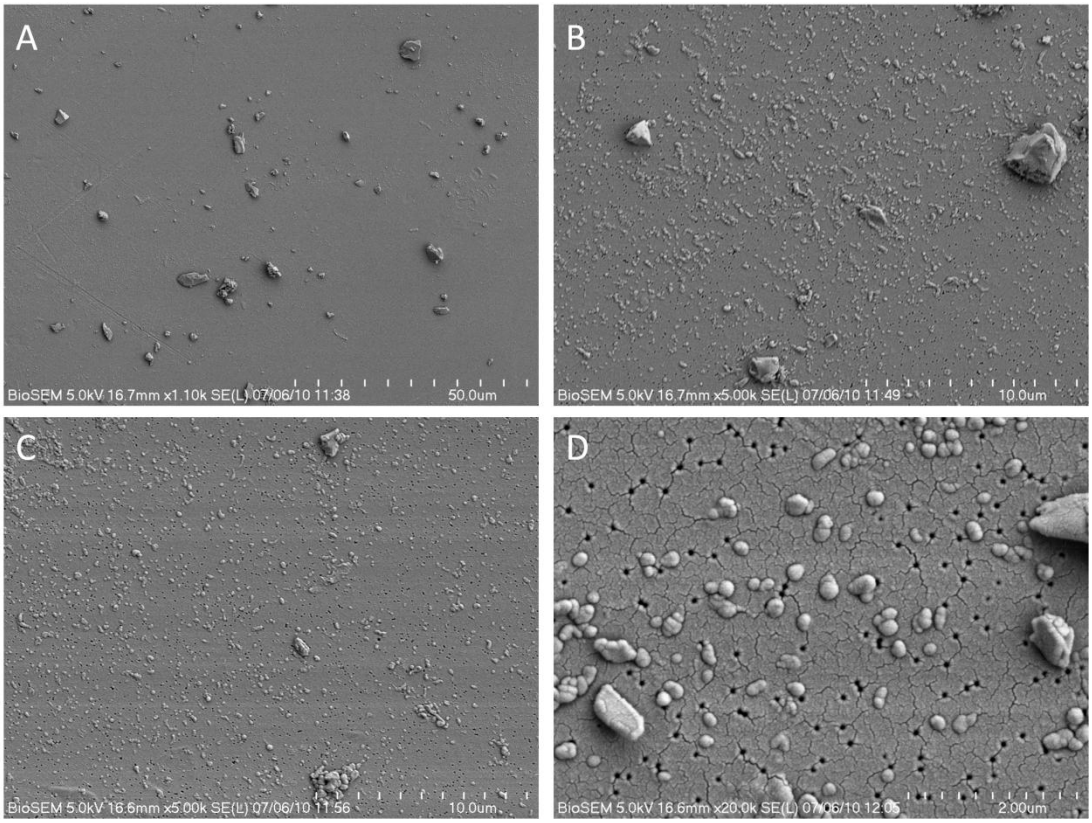

Figure 57 Elliptical 10 MRad UHMWPE on 0.1 μm polycarbonate filter. A. 1100× magnification. B and C. 5000× magnification. D. 20,000× magnification.

Over 2000 particles were taken into account for measurement purposes. Particle size was defined using the ECD. For the higher magnification views as shown in Figure 58 A the particles were found to be distributed in a positively skewed normal distribution with a mean size of 0.289 μm ± 0.211 μm (c.f. 0.995 μm ± 0.649 μm for linear wear debris). Over 90% of particles were found to be under 0.5 μm in length. The histogram from the low magnification images where particles below 1 μm in size were not included is shown in Figure 58 B. The distribution of particles follows the tail end of a positively skewed normal distribution as well. It is important to bear in mind that the high magnification data is taken over an area 20× smaller than the low magnification when comparing the data. From the high magnification data an average of 1.17 particles were found per μm^2 (c.f. 0.0336 particles for linear wear debris). This indicates that the wear rate was greater than linear wear debris, which again which would agree with the gravimetric analysis.[165]

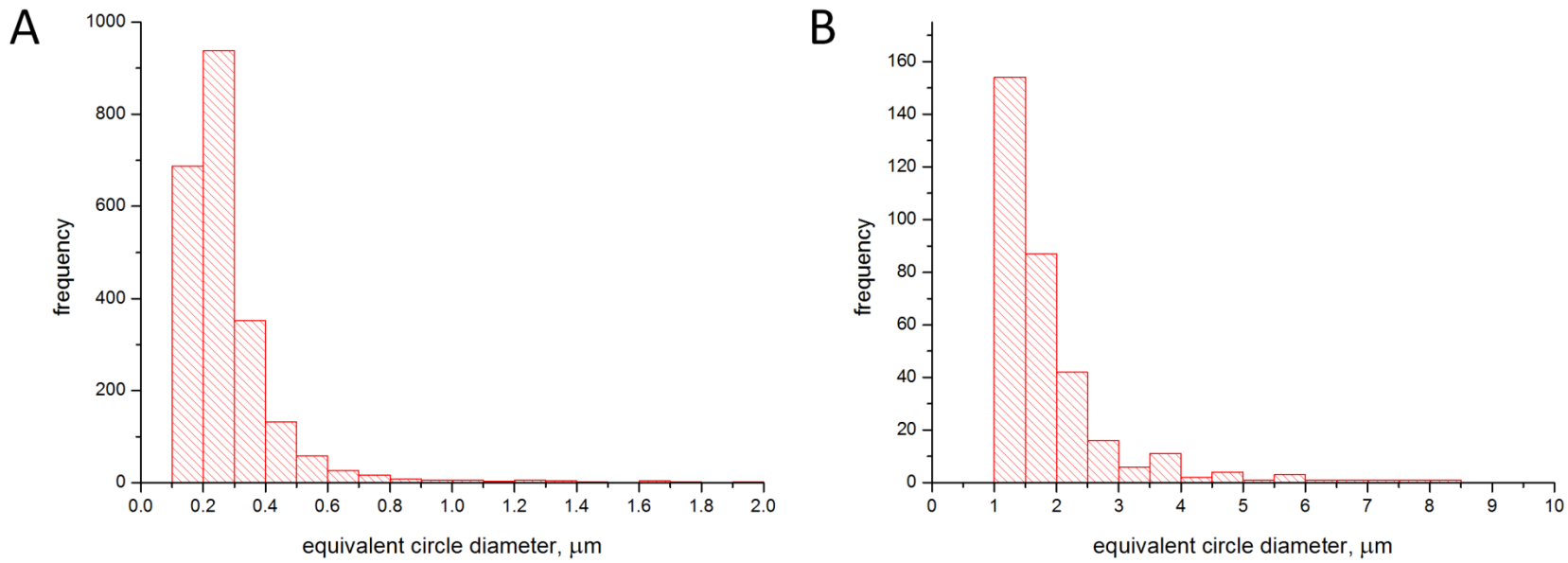

Figure 58 Histograms representing particle distribution. A. Represents all the particles found from 4 randomly chosen fields of view at a 5k magnification. Data taken over an area of 1,927 µm^2. B. Represents only particles over 1 µm in size found in 4 randomly chosen fields of view at a 1.1k magnification. Data taken over an area of 40,600 µm^2

5.3.3 Identification of wear particles.

The identity of the wear particles on the filters was confirmed as polyethylene using Raman spectroscopy. Filters were placed into the Raman microscope and measured at locations which when viewed by a 50× objective lens which appeared to have particles on them. A background taken from an untreated polycarbonate filter was then subtracted manually by aligning the peak intensities of the filter peaks from both spectra. This left a spectrum that resembled that of polyethylene (see chapter 4.1.1) signal as shown in Figure 59.

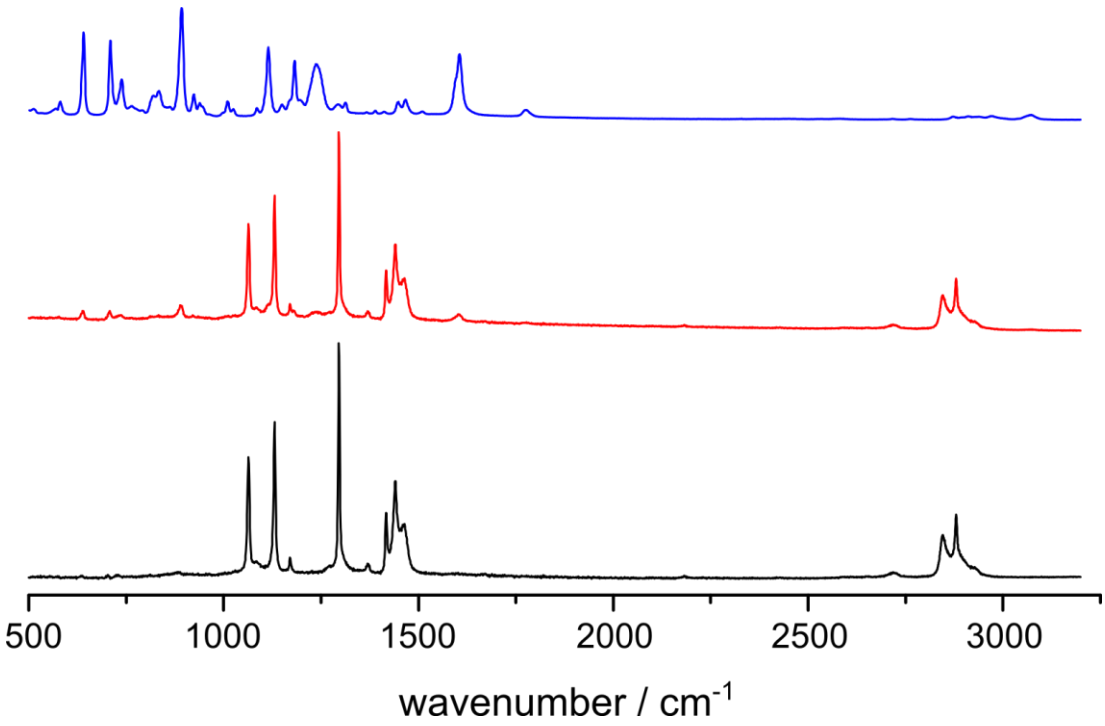

Figure 59 Raman spectra of polyethylene particles on polycarbonate filters. Polycarbonate filter on its own (blue). Polyethylene particles on the polycarbonate filter (red). Subtraction of the polycarbonate filter spectrum from the wear particles (black). Spectra are offset for clarity

5.4 Conclusions

We have demonstrated that particles from the pin on plate simulator when running with an elliptical loading pattern contain a majority of particles that are sub-micron in size. They fall into a size range that is similar to the values quoted in the literature in retrieval studies[65,67,73] as well as falling into the critical size range of 0.1 < 1 μm

that elicit the biggest *in vitro* responses.[74] This would make them a more suitable test sample when evaluating the use of CARS.

The smallest filter size that we used had pores measuring 0.1 μm in diameter. However, it has been reported that particles as small as 10 nm can be produced and have been isolated from *in vivo* and *in vitro* wear studies. Further characterisation of the particles using a smaller pore size membrane filter may reveal more information about sub 100 nm sized particles.

6 Two-photon excited fluorescence

Summary

A multiphoton microscope is a versatile tool capable of different imaging modalities to study specimens. In this chapter we explore the use of a more commonly used multiphoton technique: two photon excitation fluorescence (TPEF).

TPEF was used to image cells that had been treated with commercial fluorescently labelled nanoparticles. Fluorescent signals that indicated the presence of nanoparticles could be seen within the cell cytoplasm in all the cells tested. The nuclear region of cells contained very little fluorescence signal indicating that these nanoparticles were not able to cross the nuclear membrane. Non professional phagocytes, such as fibroblast cells, showed a more uniform level of fluorescence across the cell with a few bright spots indicating clustered nanoparticles. Professional phagocytes such as macrophage cells showed more compartmentalisation of the fluorescent signal within the cytoplasm compared to fibroblast cells.

The 3D sectioning ability of multiphoton microscopy was also demonstrated with images taken at different depths within a cell, as well as through 3D reconstructions of the images giving a volumetric view of the particles in the cell.

6.1 Control cells

Control cells were imaged with a laser tuned to 817 nm and a laser power of 21 mW measured after the objective. The gain was set to 6.5 in the Nikon C1 software and the pixel dwell time was 13.20 μs.

TPEF images of untreated cells at the settings used for our fluorescently tagged nanoparticles as shown in Figure 60 show a very low level of background signal. This gives an idea of how much brighter the fluorescent particles are than the naturally present fluorescent proteins such as flavins and porphorins that contribute to the background signal.[166]

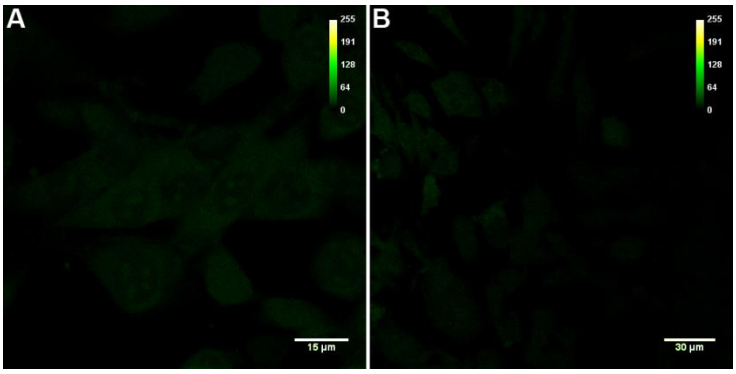

Figure 60 TPEF images of untreated cells. A. NIH 3T3 cells B. RAW 264.7 cells.

6.2 Fluorescent polystyrene nanoparticles

All cells were treated with 4 μl/ml of commercially sourced fluorescent polystyrene nanoparticles in growth media for 24 hours. Like the control cells, the treated cells were imaged with a laser tuned to 817 nm and a laser power of 21 mW as measured after the objective. The gain was set to 6.5 in the Nikon C1 software and the pixel dwell time was 13.20 μs.

A comparison to a visible light image, as shown in Figure 61, illustrates the advantages of fluorescent tagging. In the visible light image, contrast is generated through changes in refractive index, absorption and pigmentation. An added complication is that material outside the plane of focus is still visible and interferes with the image. It is not possible to directly identify the presence of the polystyrene nanoparticles in the visible light image. With a fluorescent tag added, the areas containing polystyrene particles are clearly visible. The more particles present, the

greater the TPEF signal. This helps to show areas of the cells were particles are found clustered together in greater concentrations.

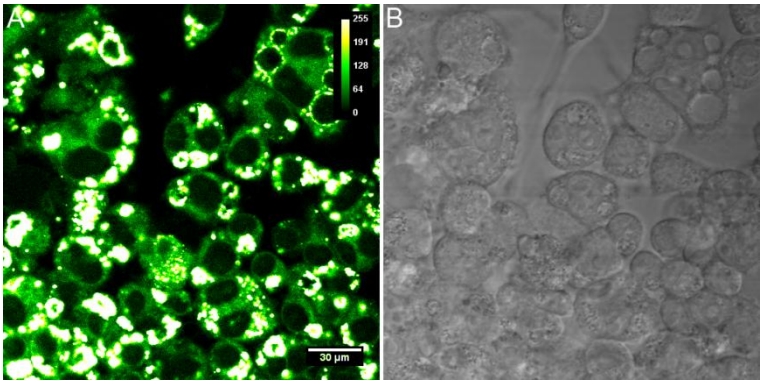

Figure 61 Images of RAW 264.7 macrophage cells treated with fluorescent nanoparticles. A. TPEF image. B. Transmitted light image.

The distribution of particles in different cell types are demonstrated in Figure 62. Each of the three cell types shares some similarities and some differences in the levels of fluorescent signals in the cell. A common feature across all three cell types was the very low signal in the nuclear area which suggests that the polystyrene nanoparticles do not easily cross the nuclear membrane once inside the cell. The non professional phagocytes, such as the NIH 3T3 fibroblast cells, showed an even fluorescence across the cell cytoplasm with only a few bright spots per cell. This suggests that the small particles are distributed throughout the cell as well as concentrated in a few areas. The monocyte derived macrophages and HL-60 cells showed more compartmentalised fluorescence in discrete areas.

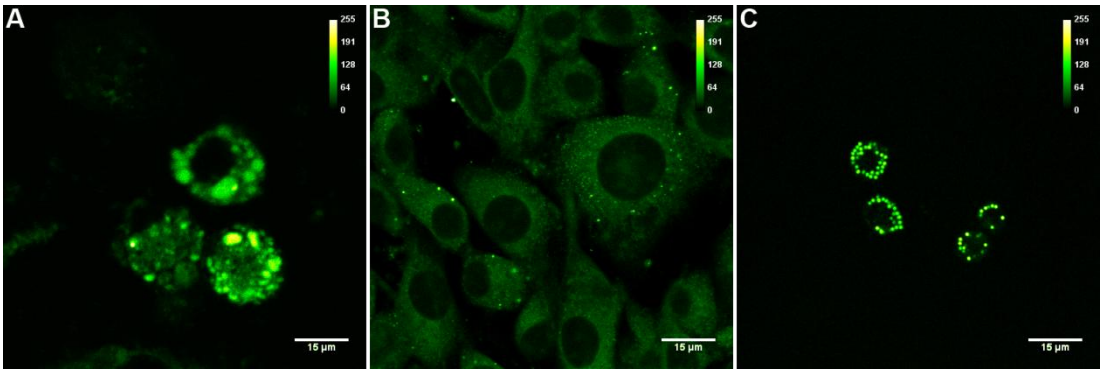

Figure 62 TPEF images of cells incubated with fluorescent polystyrene nanoparticles. A. Monocyte derived macrophages. B. NIH 3T3 fibroblasts. C. HL-60 cells differentiated with TPA.

One of the key advantages of multiphoton techniques is the optical sectioning capability due to the increased probability of absorption in the focal area compared to the rest of the incident beam. Figure 63 shows a series of images taken from an image stack showing how the distribution of particles can be tracked within the cell. These images can also be analysed using the program ImageJ to give volume and slice images for complete 2D and 3D projections of the data as shown in Figure 64.

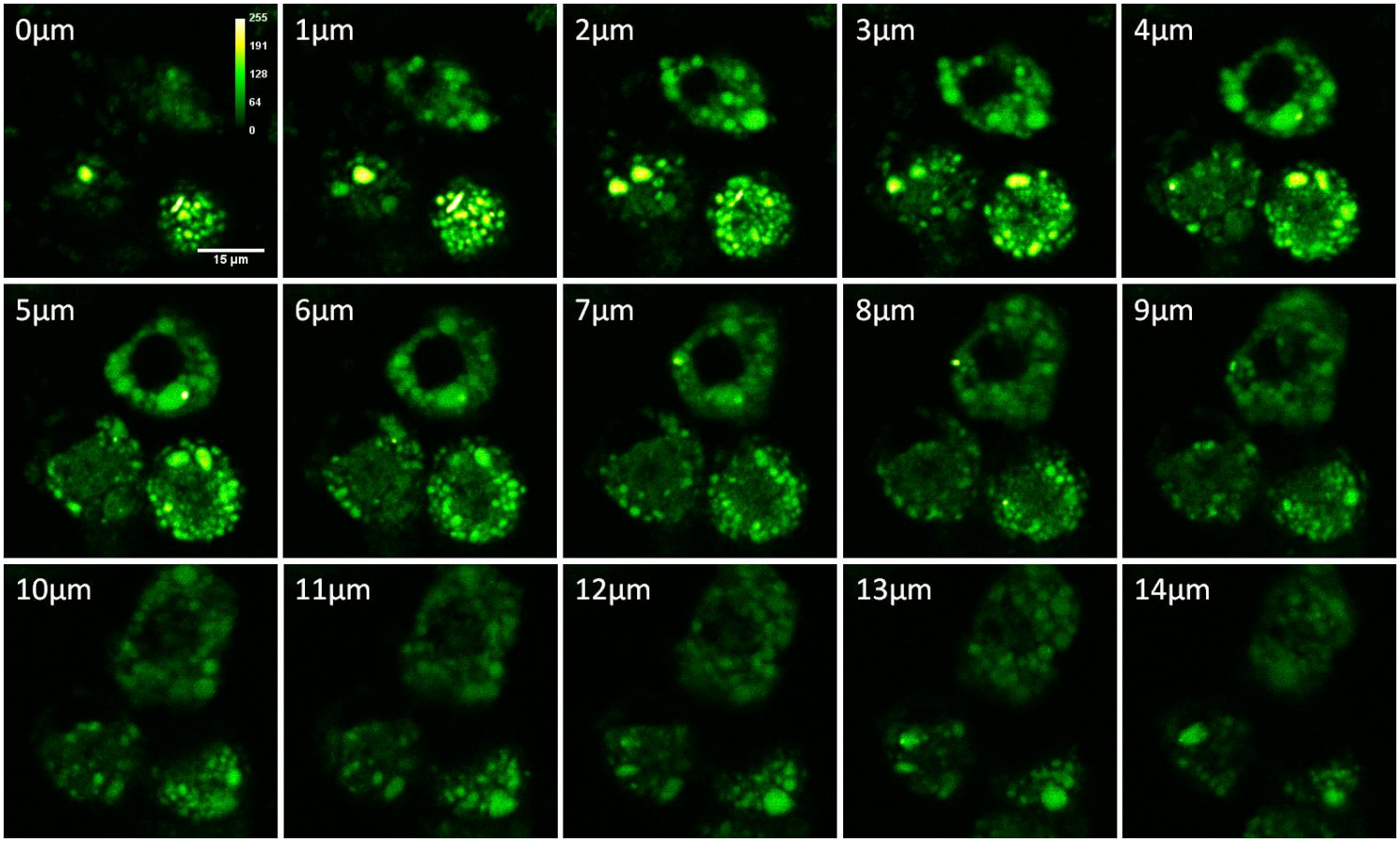

Figure 63 TPEF images of monocyte derived macrophages treated with fluorescent polystyrene nanoparticles. Each image is taken from a *z*-stack with a 1 µm vertical spacing.

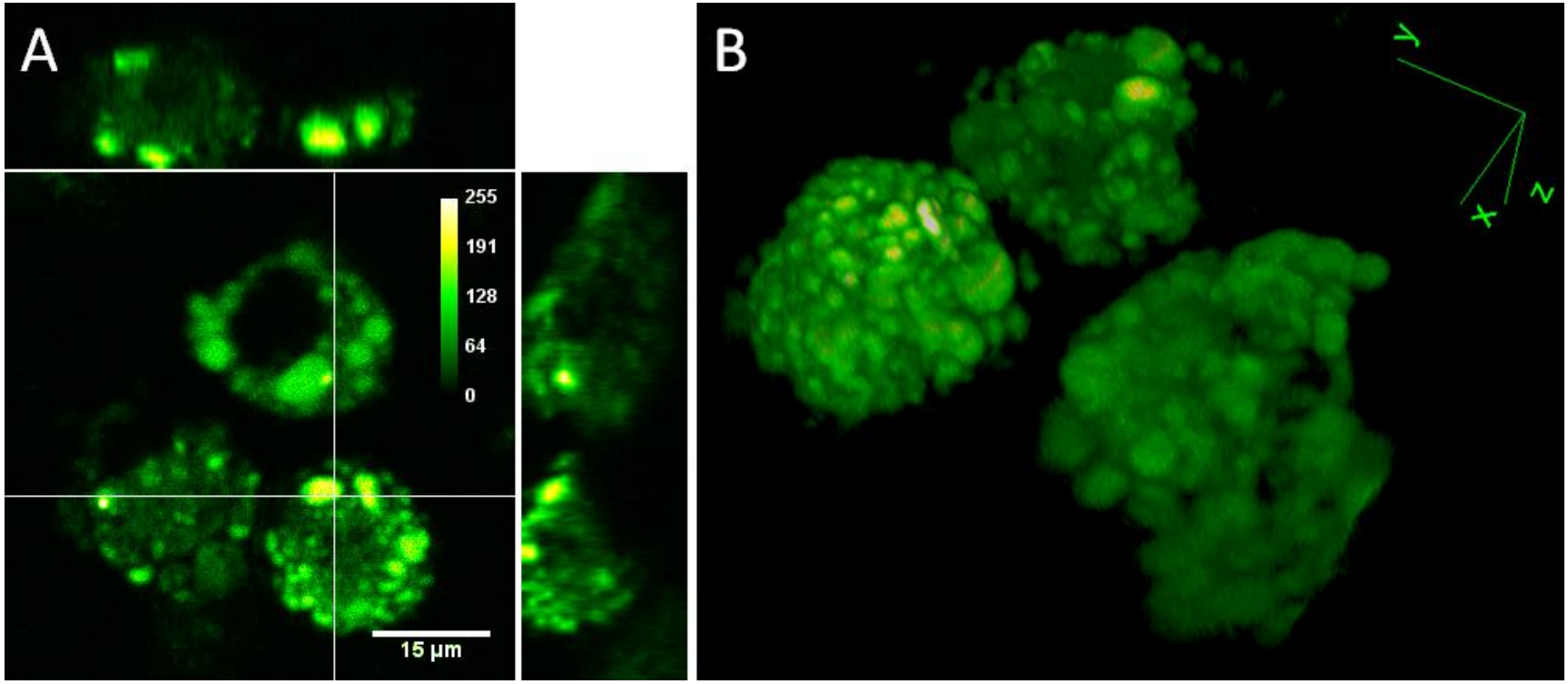

Figure 64 TPEF images of monocyte derived macrophages. A. Shows sections taken both along the *xy* and then *yz* and *yz* planes. B. Shows a 3d reconstruction of the data.

6.3 Photobleaching

TPEF relies on an electronic transition in the fluorophore to absorb the incoming photons, that energy is then emitted as a single photon. When the fluorophore is in the excited state it can undergo an irreversible chemical change which alters the fluorescent molecule causing it to lose the ability to fluoresce. This leads to a reduction in the number of fluorophores present and a fading of the fluorescent signal. The loss in signal can cause problems when multiple images are needed, and can also limit the useful laser powers that can be used on the sample as high laser powers lead to increased photobleaching.[167] Figure 65 shows an image containing an area that had been previously scanned for 5 minutes that led to photobleaching indicated by the decreased signal compared to the surrounding area. Photobleaching is not always an unwanted effect as it can be used to monitor the movement of tagged proteins of interest.[168]

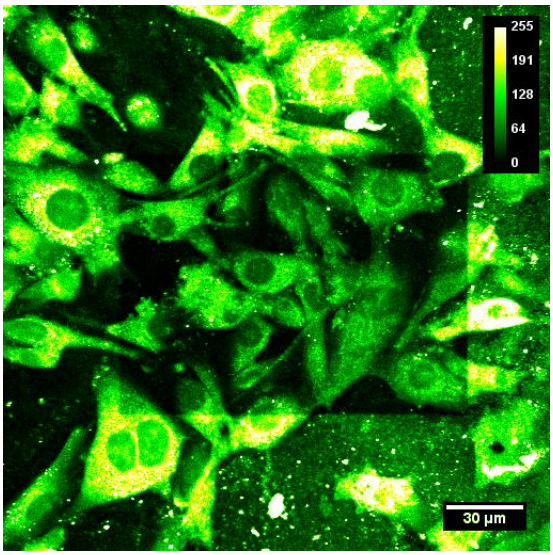

Figure 65 TPEF image of NIH 3T3 cells. The central area had been previously scanned for 5 minutes which has led to photobleaching.

6.4 Conclusions

When it is possible to add a fluorescent tag molecule to a protein or structure of interest, TPEF is able to generate detailed high resolution maps in 3D showing the presence of the fluorophore and the attached point of interest. The need to attach a fluorescent tag of interest in most cases, rather than relying on the presence of an

already existing chemical moiety to generate contrast highlights one of the problems in the use of TPEF to measure wear particles. Polyethylene itself is not fluorescent and adding a fluorescent tag to polyethylene would drastically alter the chemical and mechanical properties of the polymer.

Having a multimode microscope however, allows other regions of interest to be imaged whether through intrinsic fluorescent (flavins, etc) or the ability to stain specific cellular structures. Staining DNA, microtubules, transport proteins and membrane structures could be used to help build a more complete picture of the lifecycle of wear debris in the cell as well as biological changes to the cell that occur whilst ingesting these particles. However, when recording multiple images it should be remembered that the fluorescence signal can be reduced due to photobleaching; sequential imaging using different microscopy modes should take this into account and take TPEF images first.

7 CARS setup and validation

Summary

As our CARS setup had been custom designed and built at The University of Edinburgh, it was important to test that it functioned as expected and consistently with the background literature on the subject. This involved insuring that the setup was capable of generating a signal due to four wave mixing. We tested this using metal oxide particles which are particularly susceptible to generating light this way. Further tests examined the resonant enhancement of CARS signal generating by comparing CARS and Raman spectra and ensuring that the signal generated behaved as expected with respect to the power levels of the pump and Stokes lasers.

We also characterised the signal uniformity of our system, finding that over the full imaging field of view that the signal was not uniform. We also showed that the lasers used were capable of inducing photodamage in our samples, including membrane blebbing and breakdown, as well as ablative damage. This damage did not appear to be caused by mixing of the two beams, but by the lower wavelength, higher energy pump laser.

7.1 Four-wave mixing

To establish that the two laser beams were temporally and spatially overlapped we used metal oxide nano particles as a test sample. Metal oxides such as TiO_2 have much higher third order non-linear susceptibilities ($\chi^{(3)}$) than biological samples.[131,132] Much of this difference is in the non-resonant contributions such as the two-photon enhanced electronic resonance due to the nature of TiO_2 as a wide band gap semiconductor.[169] This makes them an attractive test samples to use before a system is fully optimised as they will generate high signals and should be easy to detect.

TiO_2 nanoparticles were imaged with a pump laser tuned to 780 nm and a Stokes laser at 1064 nm. The laser power was 13.8 mW for the pump laser and 5 mW for the Stokes laser. The gain was set to 6.0 in the Nikon C1 software and the pixel dwell time was 1.68 µs. The image taken with this setup is shown in Figure 66. The TiO_2 nanoparticles showed up as saturating bright points of light even at the fastest scan times indicating that the beams were aligned correctly allowing four wave mixing to occur.

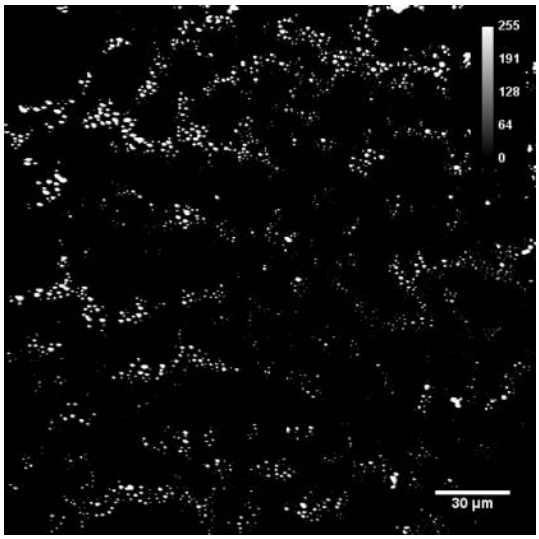

Figure 66 Forward CARS image of TiO_2 nanoparticles on a glass cover slip.

A further test to prove that the signal was generated by four wave mixing was to cover one of the laser beams, or adjust the delay stage to move the laser pulses out of alignment temporally. Both of these tests should eliminate any CARS signal. An

example of the results from this test is shown in Figure 67, below. RAW264.7 cells were imaged with a pump laser tuned to 817 nm and a Stokes laser at 1064 nm. The laser powers were 13.4 mW for the pump laser and 30 mW for the Stokes laser. The gain was set to 6.9 in the Nikon C1 software and the pixel dwell time was 61.44 µs.

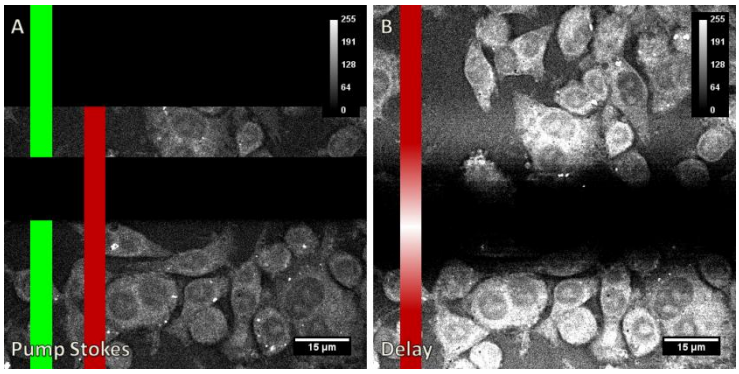

Figure 67 F-CARS images of RAW264.7 macrophage cells. A. The pump and Stokes beams have been switched on or off according to the green and red lines respectively as the image is scanned. B. The time delay between the two beams is altered. Red indicates the beams are aligned temporally, whilst white indicates they are out of alignment.

Cutting either of the beams or adjusting the delay stage to move the beams out of temporal alignment eliminated the signal coming from the sample.

7.2 Power measurements.

The intensity of the CARS signal should be linearly related to the intensity of the Stokes beam, whilst quadratically related to the intensity of the pump beam as shown in the following equation (see chapter 2.7.1):

$$P^{(3)} = \chi^{(3)} E_p^2 E_s$$

To measure the effect of changing the Stokes power, we used paraffin wax on a glass slide as the sample. The pump laser was set to 817 nm and measured at 24.8 mW. The intensity of the 1064 nm Stokes laser was controlled by adjusting the attenuator between 600 and 925 to give a power ranging from 1.6 to 20.5 mW. The gain was set to 6.5 in the Nikon C1 software and the pixel dwell time was 1.68 µs. Each image was averaged 5 times using a Kalman filter before recording. For each data point, the area in the resultant image considered to contain the sample was averaged. The

results are shown in Figure 68. The line was fitted with an equation of y = 0 + 33.3x. The adjusted R-value of the line of best fit is 0.998 demonstrating a good linear fit.

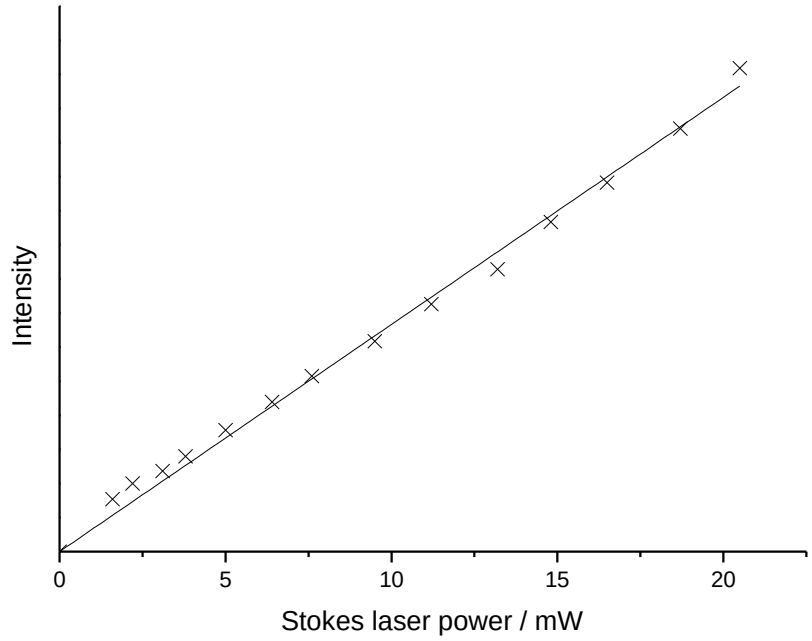

Figure 68 Graph showing the relationship between the CARS signal intensity and the Stokes laser power. A line of best fit is shown in black.

The effect of the pump laser power was measured using 5 μm polystyrene beads on a glass slide as a sample. The 1064 nm Stokes beam was set at 31 mW. The pump laser was set to 803.5 nm and adjusted between 4.5 to 20.3 mW using a half-wave plate. The gain was set to 6.45 in the Nikon C1 software and the pixel dwell time was 1.68 μs. Each image was averaged 3 times before recording. For each data point, the area in the resultant image considered to contain the sample being imaged was averaged. The results are shown in Figure 69. The line was fitted with an equation of $y = 0 + 15.3x + 2.9x^2$. The adjusted R-value of our second order line of best fit is 0.999 demonstrating a good quadratic fit.

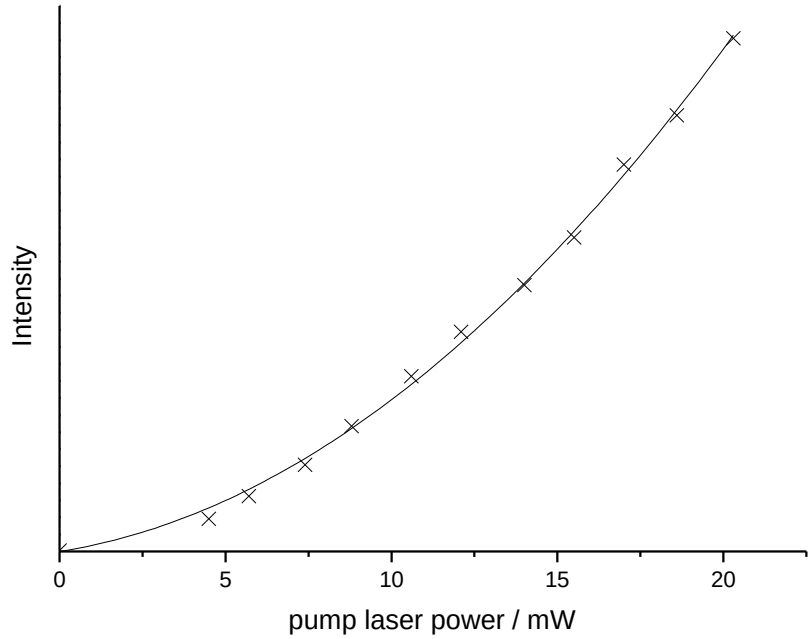

Figure 69 Graph showing the relationship between the CARS signal intensity and the pump laser power. A line of best fit is shown in black.

Modulating the power of either the pump or Stokes lasers affects the intensity of the CARS output as expected indicating that the resultant image is due to a four wave mixing process.

7.3 Vibrational resonances and CARS spectra

To test the effect of vibrational resonance on the CARS signal we used a mix of 1 μm PMMA microspheres and 3 μm polystyrene microspheres in air. Taking images with the pump and Stokes lasers set to wavelengths where a Raman signal would be generated in both compounds, and then only in polystyrene shows that the CARS signal we see is in part due to a vibrationally resonant component. The microspheres were imaged with a pump laser tuned to 815.3 nm and then 803.3 nm with laser power at 18.6 mW for both wavelengths. The 1064 nm Stokes laser was set at 30.2 mW. The gain was set to 6.0 in the Nikon C1 software and the pixel dwell time was 11.04 μs. Each image was averaged 5 times before recording.

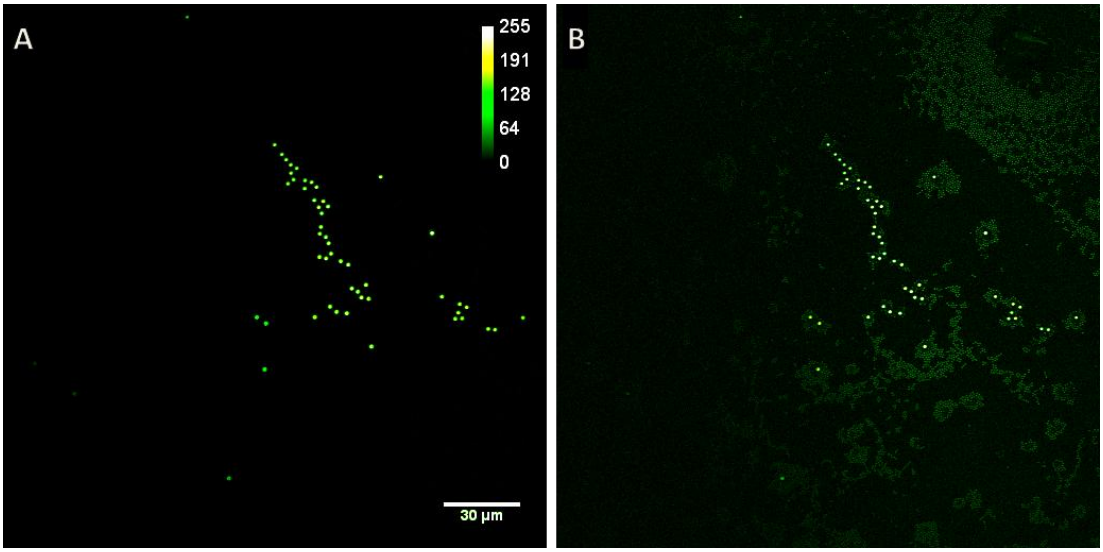

Figure 70 F-CARS images of polystyrene and PMMA microspheres. A. At an effective Raman frequency of 3060 cm^{-1} only polystyrene microspheres are visible. B. When the pump wavelength is altered to give an effective Raman frequency of 2870 cm^{-1} both the polystyrene and PMMA microspheres are visible.

CARS spectra can be obtained by adjusting the pump wavelength in small steps between whilst keeping the power and other settings constant. We examined the CARS spectra of polystyrene, polyethylene and PMMA in the C-H stretching region and compared the results to the Raman spectra. An example of the data required to generate a CARS spectrum is shown in Figure 71.

For polyethylene, we used 2 µm commercial polyethylene particles on a glass slide as our sample. The 1064 nm Stokes beam was set at 31 mW. The pump laser was set altered from 810.8 to 819.6 nm whilst kept at a power of 8 mW. The gain was set to 6.2 in the Nikon C1 software and the pixel dwell time was 4.56 µs. Each image was averaged 3 times before recording. For each data point, the signal for the area in the resultant image containing the sample was summed up and then averaged. Each data point was then plotted alongside the Raman spectrum of the compound as shown in Figure 72. The Raman spectrum of polyethylene in the C-H stretch region includes peaks at both 2845 and 2880 cm^{-1} due to symmetric and asymmetric C-H stretches.[137] These features are repeated in the CARS spectrum at the same wavenumbers.

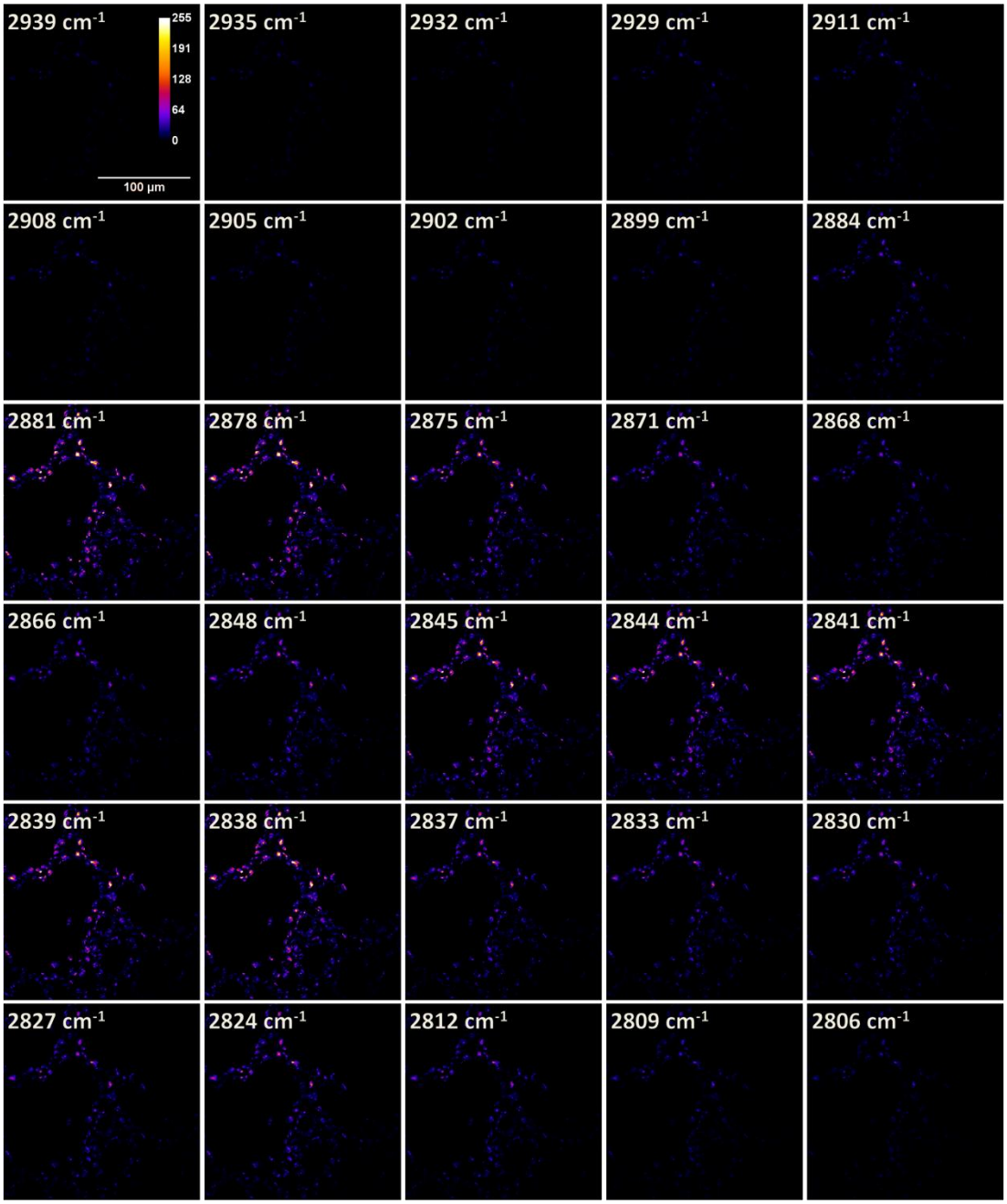

Figure 71 F-CARS images of polyethylene particles taken at different wavelengths. The intensity data from these images can be used to construct a CARS spectrum.

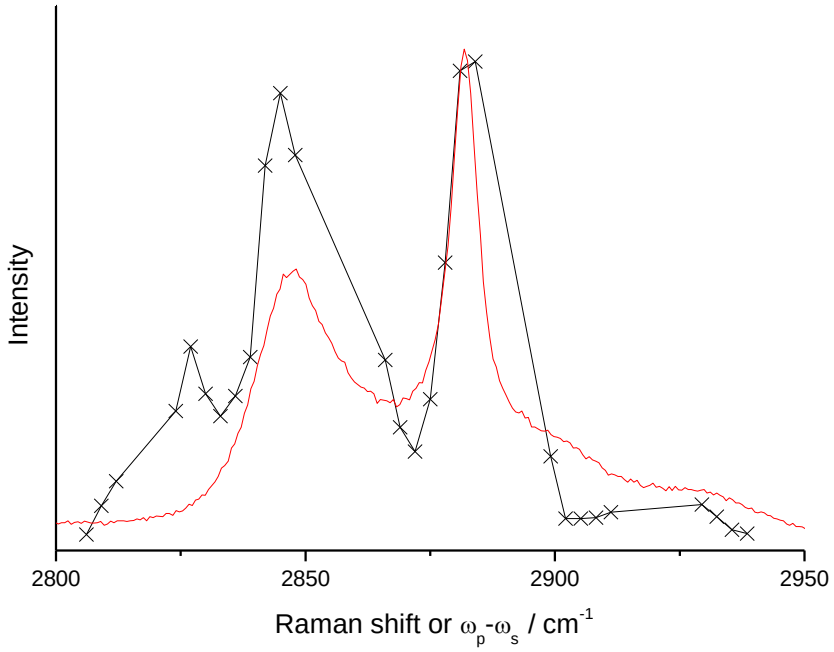

Figure 72 Raman spectrum (red line) and CARS spectrum (black line and crosses) of polyethylene.

For polystyrene, 5 μm polystyrene particles were placed on glass cover slips as a sample for measuring the CARS spectrum. As the C-H ring breathing stretch at 3060 cm^{-1} was of interest the pump wavelength was varied between 801.2 and 821 nm whilst keeping a laser power of 6.8 mW. Two separate band pass filters were needed to cover this region to ensure a 90% or better transmittance rate for the CARS signal through the filter. One was used between the 801-805 nm and another was used between 810-821 nm. The 1064 nm Stokes beam was set at 6.3 mW. The gain was set to 6.25 in the Nikon C1 software and the pixel dwell time was 61.44 μs. For each data point, the signal from the area in the resultant image that contained the sample was summed up and then averaged. Results are shown in Figure 73.

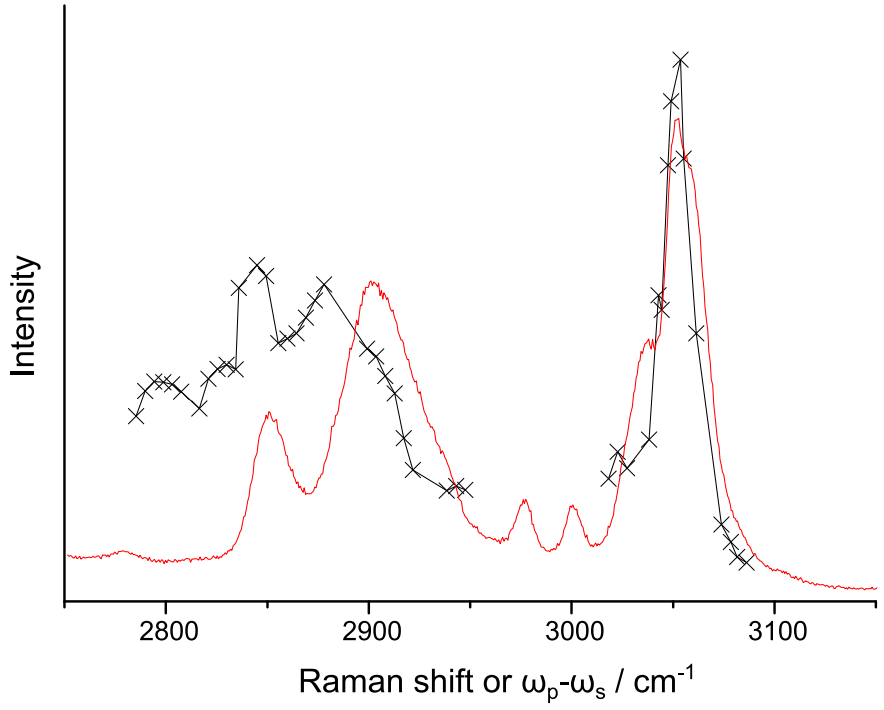

Figure 73 Raman spectrum (red line) and CARS spectrum (black line and crosses) of polystyrene.

The peak at 3060 cm^{-1} in polystyrene due to C-H bonds in the phenyl ring stretching is repeated in CARS spectrum at the same wavenumber. The chain C-H stretching appears to be blue shifted slightly compared to the Raman spectra peaks. It has been suggested that the interaction of the non-resonant and resonant terms leads to a red shift in the spectrum to lower wavenumbers and interference with other resonant peaks can lead to unpredictable spectra (see Figure 12 for more details).[95]

For PMMA, 1 μm PMMA beads were placed on glass cover slips as a sample for measuring the CARS spectrum. The 1064 nm Stokes beam was set at 26 mW. The pump laser was altered from 808 to 819.9 nm whilst it was kept at a power of 8 mW. The gain was set to 6.5 in the Nikon C1 software and the pixel dwell time was 61.44 μs. For each data point, the area in the resultant image considered to contain the signal was summed up and then averaged. Each data point was then plotted alongside the Raman spectrum of the compound as shown in Figure 74.

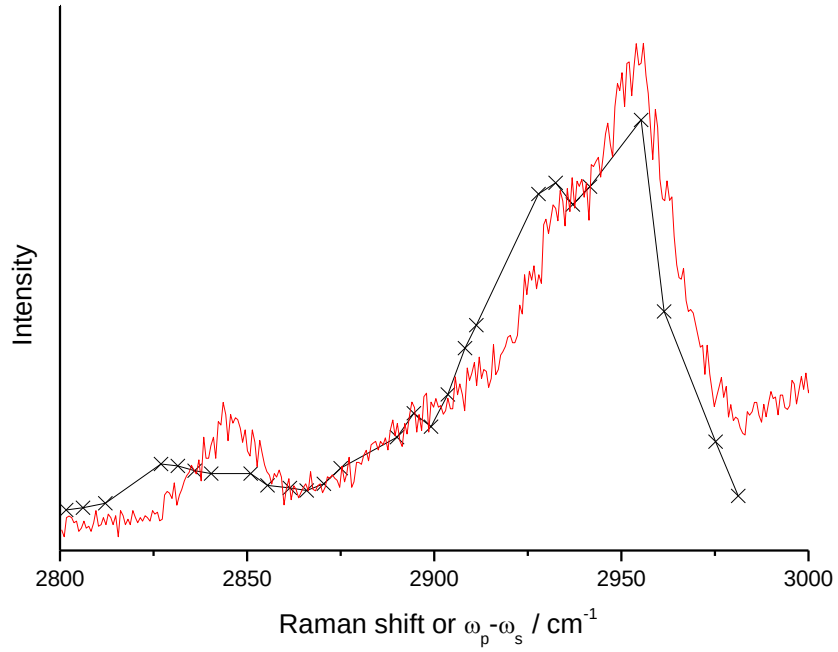

Figure 74 Raman spectrum (red line) and CARS spectrum (black line and crosses) of PMMA.

The PMMA Raman peaks are again repeated in the CARS spectrum, the 2953 cm^{-1} peak appears at the same wavenumber whilst the 2843 cm^{-1} peak appears red shifted slightly.

The similarity between the Raman spectra and CARS spectra of these compounds suggests that there is a large resonant component to the images acquired. This in turn will allow identification of different compounds based around the signal levels at their resonant wavelengths.

We tried using our setup to detect Raman resonances around 1600 cm^{-1}, which would produce CARS photons around 794 nm. The detectors used in our CARS setup have a limited quantum efficiency range, dropping to less than 14% with incoming photons above 640 nm in wavelength (CARS photon wavelength when measuring a Raman resonance at 3060 cm^{-1}), and less than 7% above 794nm (CARS photon wavelength when measuring a Raman resonance at 1600 cm^{-1}).[170] We were able to record an image from polystyrene at a Raman shift of 1600 cm^{-1} as shown in Figure 75. This image was recorded with the 1064 nm Stokes beam set to 28.4 mW. The pump laser was tuned to 909.6 nm and the power measured after the objective was 18.2 mW. The gain was set to 7 in the Nikon C1 software and the pixel dwell time

was 410 μs. The image took 107 seconds to record, noticeably slower than the typical times used when the Stokes and pump lasers were set to vibrationally resonant with Raman wavelengths in the C-H stretch region which typically took less than 10 seconds to record an image.

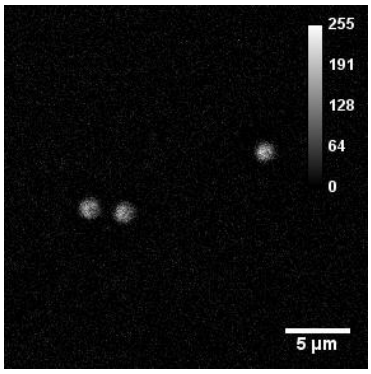

Figure 75 Forward CARS image of three polystyrene beads recorded with an effective Raman wavelength of 1600 cm^{-1}.

7.4 Optical Sectioning

We used a phantom consisting of polystyrene beads in a 3% agarose gel to test the optical sectioning capability of our CARS setup. The 1064 nm Stokes beam was set at 16.4 mW. The pump laser was set at 803.5 nm and the power measured was 22.4 mW. The gain was set to 6.35 in the Nikon C1 software and the pixel dwell time was 15.36 μs. A stack of 81 images were recorded with the *z*-plane increasing by a height of 0.25 μm on each image recorded which was close to 4× the calculated z-resolution (see section 3.3.1 on CARS resolution). The images were then resliced in ImageJ as required and displayed as projections of the highest detector count in the image stack. The result is shown in Figure 76. The images collected clearly showed that polystyrene beads embedded at different depths are visible although there does appear to be some distortion to the spherical bead shapes. The images taken in the agar phantom also show a background signal, highlighting the contribution of unwanted resonant and non-resonant signals to the image.

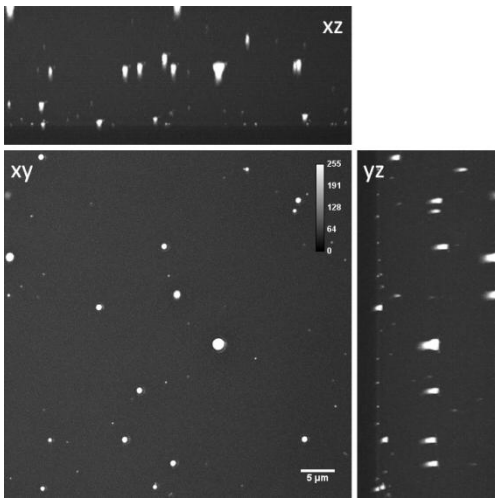

Figure 76 F-CARS images of polystyrene beads in agar. *z*-projections showing the maximum collected signal are shown along the *xy*, *xz* and *yz* planes. For the *xz* and *yz* images, upwards and rightwards is upwards from the inverted objective. This is the same for all planar visualisations in the this thesis.

7.5 Beam scanning uniformity

CARS images produced using the maximum 212 µm field of view from our setup produced a noticeably non-uniform level of CARS signal. This effect is shown in Figure 77 A. To overcome this problem many of the images taken were scanned with a reduced field of view, typically 100 µm on smaller where the image appeared more uniform as shown in Figure 77 B and these settings were used for the majority of images taken.

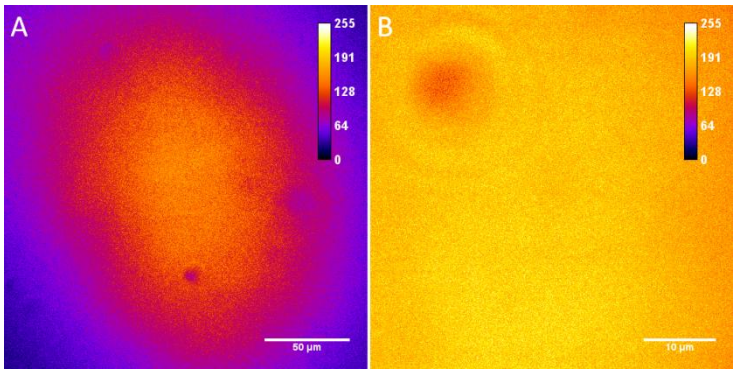

Figure 77 F-CARS images of a 50% methanol solution. A. The full field of view available with the 60× oil immersion objective with a noticeable drop in signal at the peripheries of the image. B. The field of view is reduced giving a more uniform signal over the scanned area.

Fine adjustment on the mirrors in the collecting lens had a large effect on signal levels across the image, as did adjusting the angle of entry for the lasers into the scanning unit. It is also possible that the two different wavelengths used were not superimposed on each other before entering the focal unit, or they diverged from each other whilst going through the scan unit and objective.

7.6 Photodamage and photobleaching

The CARS process does not involve an electronic transition but a virtual one. Because of this there are no excited states to depopulate and no photobleaching effect occurs. However, photodamage can occur due to both linear absorption and to multiphoton effects from one or both of the lasers used.

The main types of photodamage that we observed were ablation of samples, this was possibly due to previously reported plasma formation.[171,172] Examples of this are shown in Figure 78. This photodamage occurred whilst using the lasers in both temporally aligned and unaligned configurations suggesting that this photodamage was not dependent on any vibrational absorption occurring. Membrane blebbing and breakdown were also observed as shown in Figure 79. This photodamage also occurred when just the 817 nm pump beam was used to scan the sample, but not when the 1064 nm Stokes beam was used in isolation.

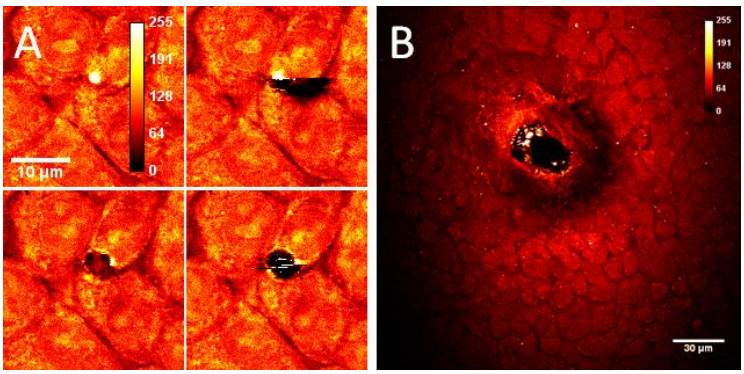

Figure 78 A. Clockwise from top left showing consecutively scanned F-CARS images of HEK 293 cells and the ablative photodamage that results. B. The central area had been scanned previously for 5 minutes with the CARS setup although a delay was introduced between the two beam pulses to prevent four-wave mixing.

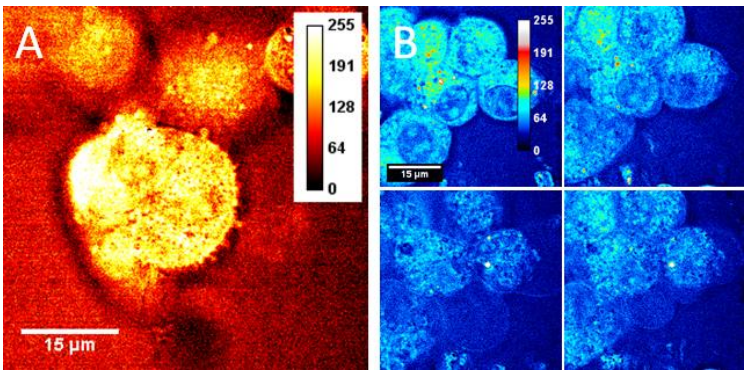

Figure 79 A. F-CARS image of membrane blebbing in NIH3T3 fibroblast cells. B. Clockwise from top left. CARS images of membrane breakdown in cells.

We imaged 5 µm polystyrene spheres within a near index matching oil with a variety of beam setups to investigate the source of the photodamage. Imaging with only the 1064 nm Stokes laser on the sample did not produced any visible photodamage on the polystyrene spheres whilst imaging with only an 803.5 nm pump beam completely ablated the sample within 50 consecutive scans. We noticed that consecutive scans and discontinuous scans separated by 60 seconds both produced visible photodamage at similar rates. Discontinuous scanning seemed to produce many small sites of damage, whilst the continuous scanning produced fewer, but larger sites of damage as shown in Figure 80.

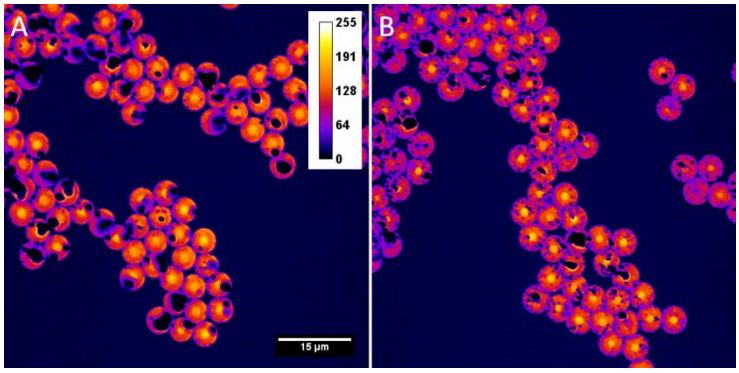

Figure 80 F-CARS images of 5 µm polystyrene microspheres after 33 scans. A. Shows the results from a continuously scanned sample of latex spheres B. Shows the result of latex sphere scanned the same number of times as A. but with a 60 second delay between each scan.

7.7 Conclusions

We have demonstrated that our multiphoton setup could record CARS signals. The system was able to record CARS images from a variety of different wavelengths

although performed the best when the CARS photons were closest to the optimal detection efficiency of the photomultiplier tubes. Our setup produced sufficient resonant signals to reproduce Raman spectra from samples which will help to identify different compounds whilst being imaged.

Prolonged exposure of biological samples to the laser beams used in the CARS process does produce photodamage, and so careful consideration will need to be made when choosing excitation powers and wavelengths to study.

8 Model Particles

Summary

Although much theoretical work has been undertaken to resolve the nature of the CARS signal, there are few experimental results demonstrating how changes in size of the particle and refractive index of the bulk surroundings affect the measured CARS signal. We examine single particles under both forward and epi-detection conditions.

Model particles made of polystyrene were relied upon due to their availability in a number of defined size ranges. We show that as the particle size increases, so does the forward CARS signal generated, although much of this effect appears to be related to refractive index changes between the particle and the surroundings. Small particles of 100 nm diameter were shown to be difficult to make out from the non-resonant background.

Epi-detected CARS signals in our setup were found to be much weaker than the forward CARS signals. Contrary to the theoretical calculations we found that smaller particles (<1 μm) did not have a greater E-CARS signal than large particles (> 1 μm). We attribute this to the majority of the epi-detected CARS signal being made up of a reflection of the forward CARS signal.

8.1 Forward CARS on model particles in air

We used a set of polystyrene beads with diameters measuring 0.5, 0.75, 1, 2, 3 and 5 μm to measure the CARS signal generated in the forward direction. Beads were deposited on glass cover slips and then measured at the 3060 cm^{-1} peak. The Stokes beam set to 1064 nm and pump beam set to 803.5 nm, both beams were set to 8 mW of power. The gain was set to 6.6 in the Nikon C1 software and the pixel dwell time was 5.04 μs. The field of view was limited to 75 μm and *z*-stacks were taken with a 0.1 μm spacing. Averages of 6 traces through the centre of each bead were plotted as shown in Figure 81. It was noticeable that the larger the bead size, the greater the CARS signal that was detected. This effect seemed to lessen as the beads approached 5 μm in size. The other effect noticed is that the generated CARS signal extended beyond the actual bead diameter.

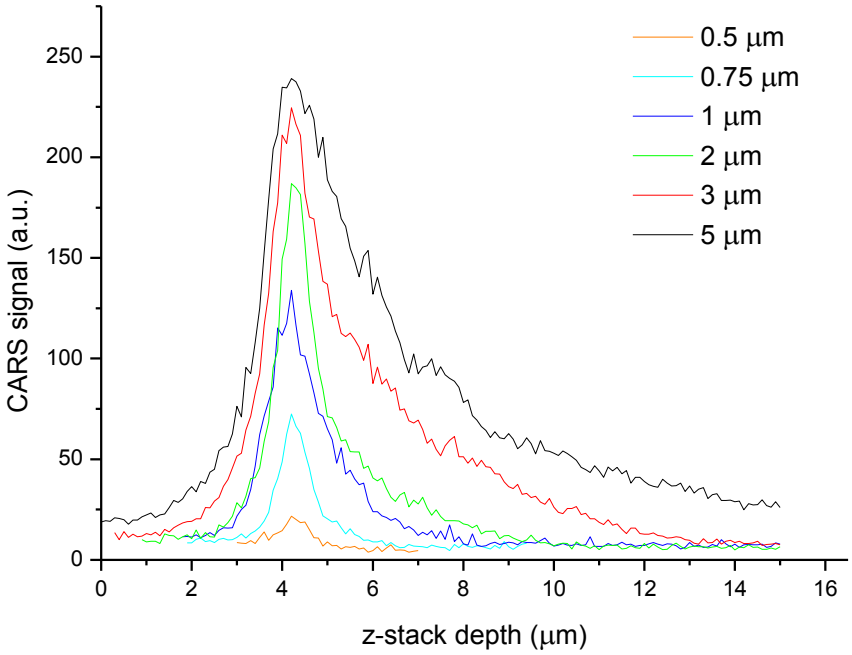

Figure 81 Graph showing the CARS signal intensity of polystyrene beads taking through the *z*-axis. Particles were imaged air with traces showing the average of n = 6 beads.

It is well reported that the CARS signal is related to the square of the number of vibrational oscillators[95] and so we would expect that the larger beads, would generate larger CARS signals as seen. However, this effect should be limited by the focal excitation volume.[173] It is possible that our beams are not focussed perfectly due to

chromatic aberrations in the lens. This leads to focal spots separated on the z-axis. We have shown that the z-axis resolution is around 1 μm which would help to explain the lengthening effect. This is also enhanced by refractive index mismatches between a sample and its surroundings generates distortions in the CARS image (see Figure 17).[99]

8.2 Forward CARS on model particles in water and oil

To further investigate the effects of refractive index mismatches between our polystyrene samples (n = 1.57-1.58 between 800 and 1064 nm) and its surroundings, we took CARS image stacks in water (n = 1.33) and immersion oil (n = 1.52). The CARS setup was the same as the previous experiment, including the same gain value set in the software so the images were comparable. Image projections of the 3 μm beads are shown in Figure 82. The images show that as the refractive index of the surroundings increases to match that of the sample, the image of the bead becomes more uniform and less distorted. The signal levels recorded decrease as the refractive index of the surroundings increases. There is also a larger non-resonant background signal present in the water and oil images.

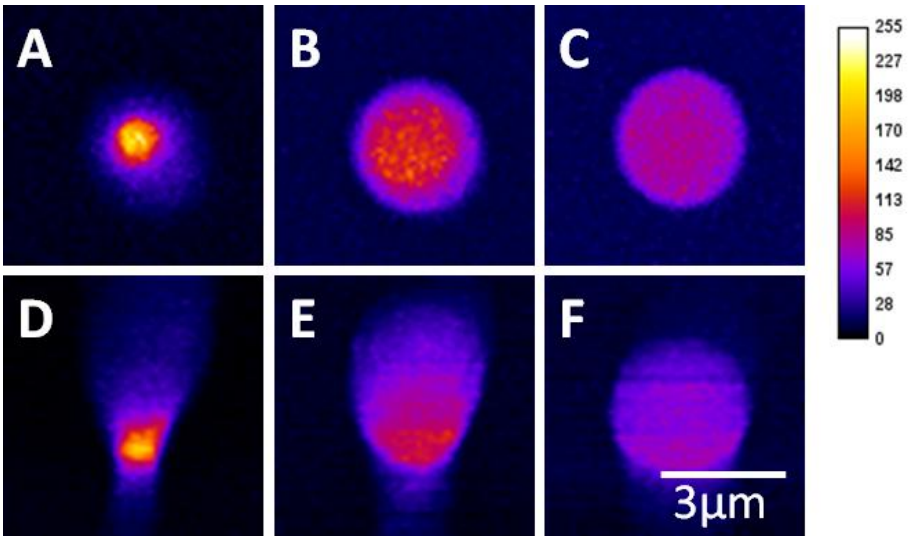

Figure 82 F-CARS images of 3μm polystyrene beads in different surrounding media. A-C show *xy* projections whilst D-F show *yz* projections of the beads. A and D are taken in air, B and E are taken in water and, C and F are taken in immersion oil.

Average traces through the centres of the beads in the near index matching oil are shown in Figure 83. The CARS signal through the bead is shown to be more uniform, and there is less apparent deformation in the shape of the bead through the *z*-axis. There appears to be a drop in the signal level for the 3 μm bead as shown by the red line in Figure 83, this may be due to power fluctuations which sometimes occurred when the cooling system was not functioning optimally. It can also be seen that the maximum signal of the 5, 3 and 1 μm beads are closer to each other than in air.

Plotting the maximum collected signal from the beads shown in Figure 84 shows that when immersed in the near index matching oil the maximum collected signal is achieved around 1 μm diameter, which is close to the theoretical predictions where the maximum signal should come from any bead larger than the focal point of the laser beams. The background level was around the levels shown in Figure 81 and Figure 83, respectively for air and oil.

The increased signal in the air is likely due to the focal point becoming trapped in the polystyrene bead due to the large refractive index mismatch as explained by Djaker, et al.[99] The apparent laser focal point and the actual focal point differ due to the refractive index mismatch. As the focal point moves through the bead's *z*-plane, the excitation intensity may increase as the focal point is compressed into a smaller area at the bottom surface of the bead. This also explains why the CARS signal is generated outside of the confines of the bead. The beams actual focal point is trapped within the bead even if the apparent focal point should be outside (see Figure 17 and related text for details).

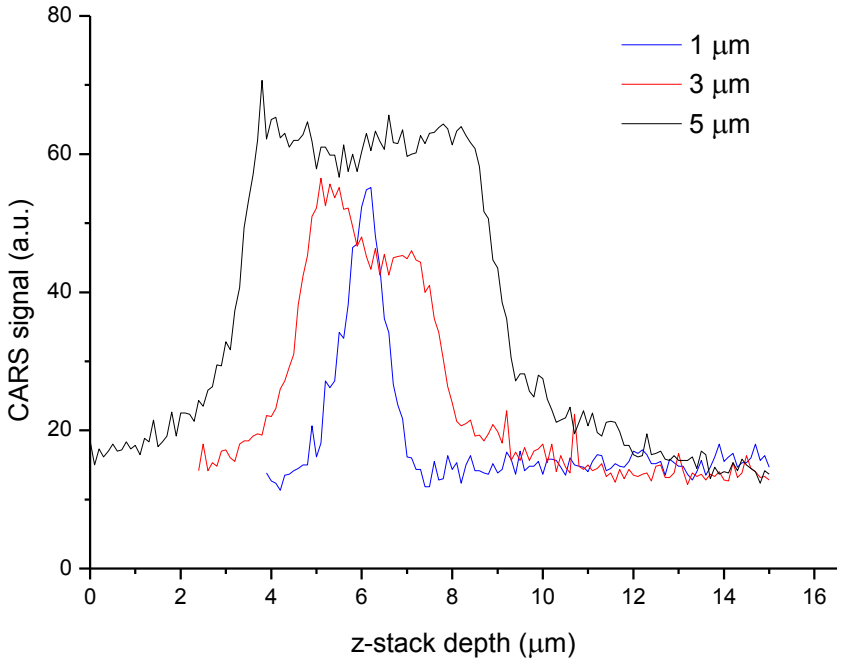

Figure 83 Graph showing the signal intensity taking through the *z*-axis of polystyrene beads of increasing diameters imaged in near index matched oil (n = 1.52). Graphs show the average of n = 6 beads.

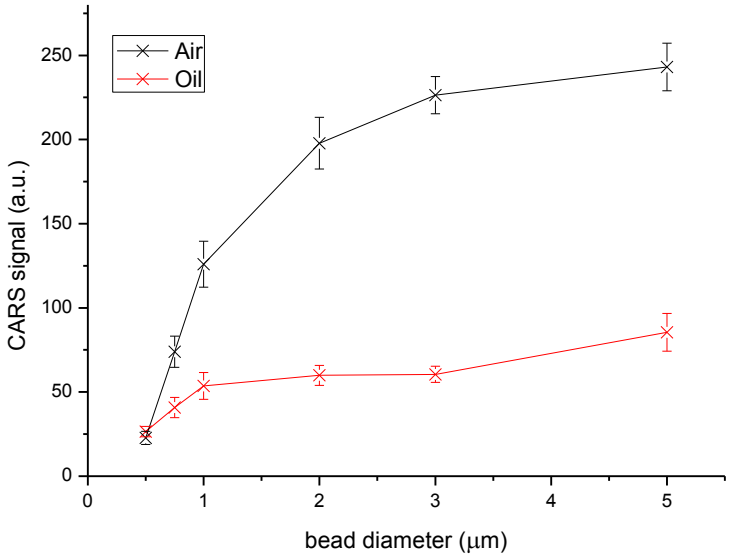

Figure 84 Graph showing the maximum collected forward CARS signals from polystyrene beads of increasing diameter. The graph shows beads in air (black) and red (oil) ± standard deviation n ≥ 6.

8.3 100 nm sized polystyrene particles

The smallest model particles that we were able to image using CARS were 100nm in diameter. We used the highest laser power possible without burning the samples, and took an average of 3 readings to obtain the best possible image. The Stokes beam was set to 1064 nm and 30 mW of power whilst the pump beam set to 803.5 nm and 25 mW of power. The gain was set to 7 in the Nikon C1 software and the pixel dwell time was 61.44 μs. The field of view was limited to 30 μm. The resulting image is shown in Figure 85. Due to the very low signal levels it is hard to make out whether individual particles are visible, rather than smaller clusters of particles. The coherent nature of the process means the CARS signal generated in the excitation volume is proportional to the square of the concentration of vibrational oscillators. Individual particles may not be noticeable but multiple particles will add together to produce a visible signal.[90]

If particles do not cluster together in cells, sub micron sized particles may not be visible in our system. However, if the particles do agglomerate together, then even nanometre particles may be detected as clusters of particles within a cell.

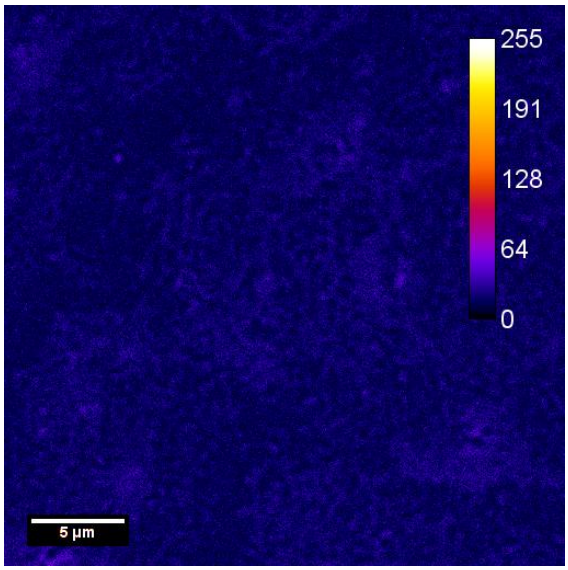

Figure 85 Forward CARS image of 100 nm polystyrene beads in water.

8.4 Epi-detected CARS on model particles

In the epi-detected setup the back scattered light is collected by the objective lens. In theoretical calculations, it has been shown that a similar forward and backward signal is generated from scatterers that are smaller than the excitation beams, whilst larger scattering objects (such as the solvent) should be confined to the forward direction. [91,97,173] However, it has also been suggested that the majority of the epi-detected signal is a backward scattered reflection of the forward CARS signal.[99]

As with the forward detected experiments, polystyrene beads were deposited on glass cover slips and then measured at the 3060 cm^{-1} peak. The Stokes beam was set to 1064 nm and 35 mW of power whilst the pump beam set to 803.5 nm and 32 mW of power. The gain was set to 6.3 in the Nikon C1 software and the pixel dwell time was 61.44 μs. The field of view was limited to 100 μm and *z*-stacks were taken with a 0.15 μm spacing. The CARS power needed to generate comparable images to our F-CARS was much higher. Our epi-detected setup had the collection of the backwards scattered light going through both the objective lens and the scan unit. The efficiency of this detection path, coupled with a fibre connection to the detector are other possible explanations of the low CARS signal detected.

One of the first noticeable results was that despite using the same set of filters, we were unable to completely remove all unwanted laser light. Figure 86 shows what we considered to be a reflection from the glass cover slip of the pump laser. Although covering one of the lasers or changing the time delay seemed to eliminate the CARS signal generated by the polystyrene beads, we still had a background present that only disappeared when the pump laser was turned off.

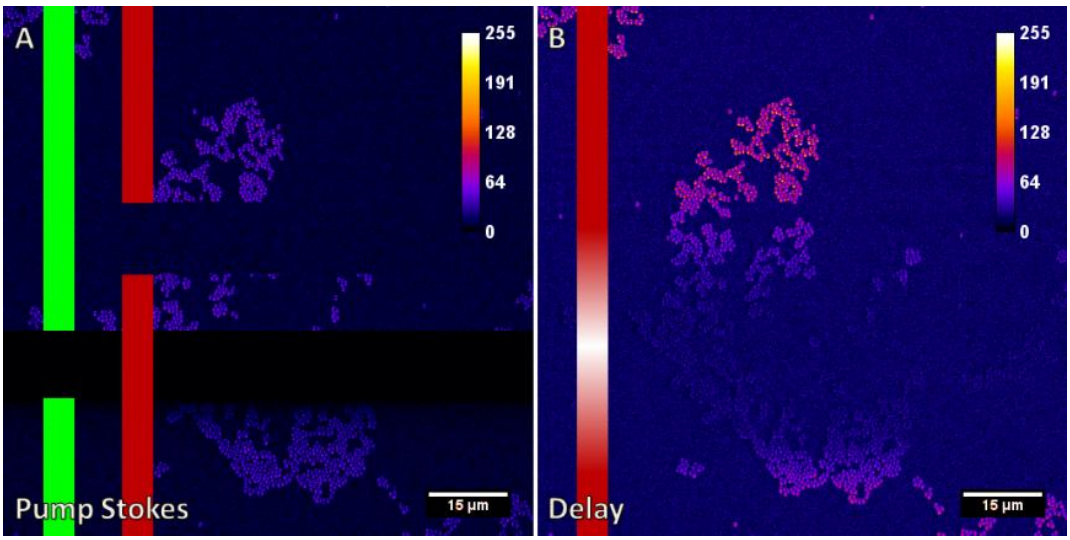

Figure 86 Epi-detected CARS images of polystyrene microspheres. A. The pump and Stokes beams have been switched on or off according to the green and red lines respectively as the image is scanned. B. The time delay between the two beams is altered. Red indicates the beams are aligned temporally, whilst white indicates they are out of alignment

In Figure 87 we show the projected view of a typical single bead taken under the epi-detected conditions described previously. We were unable to see any CARS signal detected from a polystyrene bead in the near index matching oil. The signal from the bead generally looked quite even when viewed from the *xy* plane in both air and water. The *yz* projected views are very different to those found in the F-CARS images shown in Figure 82. In air, there is a large signal visible where the bead sits on the glass cover slip (the glass cover slip is also visible due to the reflection of the pump beam being detected) and then a large column above that extending almost 10 µm above the plane of the glass surface. In contrast, the *yz* image of the bead in water does not show a signal from the glass cover slip, and the signal seems to be contained within a rough 3 µm sphere. Again, the signal level is not uniform across the bead but appears concentrated around the upper surface.

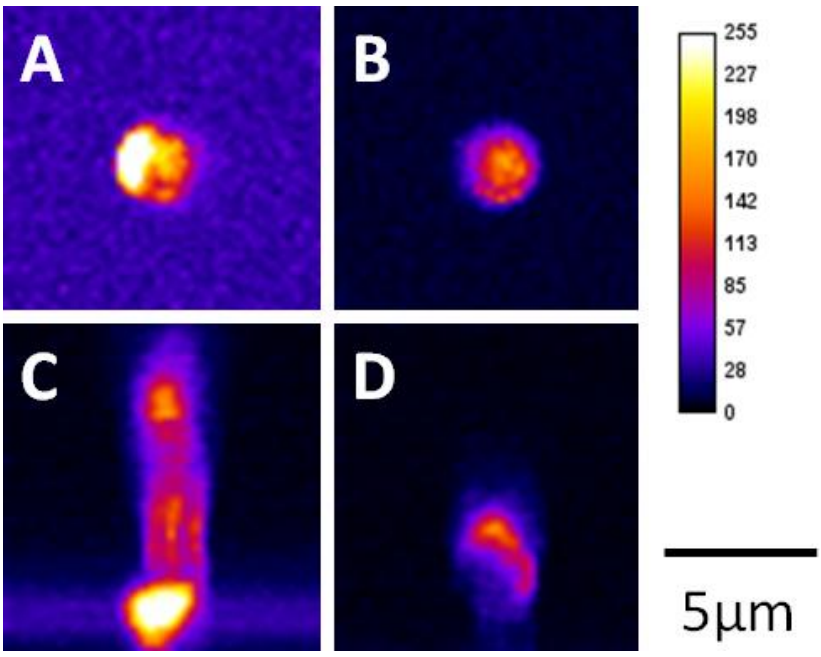

Figure 87 E-CARS images of 3µm polystyrene beads in different surroundings. A and B show *xy* projections whilst C and D show *yz* projections of the beads. A and C are taken in air whilst B and D are taken in water. No signal was detected from beads in immersion oil.

As we were not able to see any CARS signal when the beads were immersed in the oil it seems likely that the results from air and water were the results from a backwards reflected forward CARS signal rather than any backwards generated CARS signal. The *yz* projected images of all the beads imaged in water (shown in Figure 88) shared the same characteristic of a larger CARS signal emanating from the top surface of the bead.

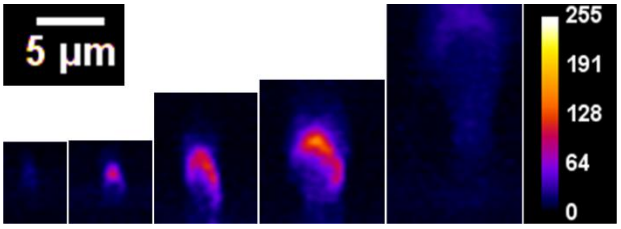

Figure 88 Epi-detected *yz* image projections of polystyrene beads. Left to right 0.75, 1 , 2, 3 and 5 µm.

The overall signal levels from the beads did not behave in the manner that had been calculated by Cheng et al.,[92] who predicted a maximum signal achieved when the scattering sphere diameter was around 0.3 to 0.8 times the size of the pump

wavelength and a 10^4 times smaller signal when the diameter was five times the size of the pump wavelength. In Figure 89 we show the maximum collected signal from our epi-detected tests in air and in water. In air, we found that our detector was saturated by the signal from the 1 μm beads, but we did see larger signals coming from beads with a larger diameter than the pump wavelength, rather than the smaller diameter beads as might be expected. Although the overall signal level was much smaller for the beads measured in water, the resulting pattern was similar to that attained in air, with the beads larger than the pump wavelength generating a stronger signal than those larger than the pump wavelength.

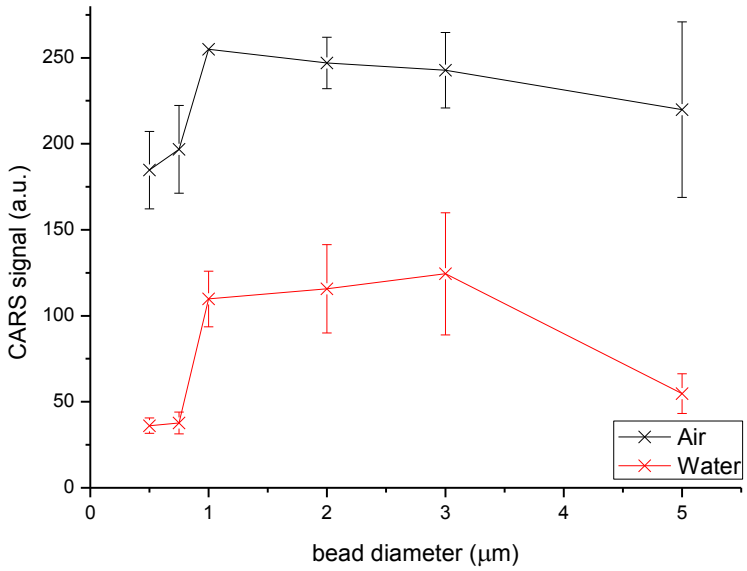

Figure 89 Graph showing the maximum collected epi-detected CARS signals from polystyrene beads of increasing diameter. The graph shows beads in air (black) and water (red) ± standard deviation n ≥ 6.

8.5 Conclusions

The behaviour of polystyrene beads gives us a good idea on what to expect when imaging particles within cells and any limitations we may encounter. We can see from the forward CARS images that the signal levels for individual particles behaves similarly to the theoretical calculations, although the refractive index of the surroundings can alter the signal levels to a large extent. This is especially important

given the variety of different micro-environments within a cell where particles could reside which vary from $n = 1.3$ in water filled vacuoles to $n = 1.7$ in melanocytes.[99] However, we found that viewing very small particles on a single plane was still a challenge even when we used long acquisition times and averaged multiple images.

Our work on the epi-detected CARS setup has shown a number of problems that need to be considered when interpreting results. The main issue is the inability to completely filter out all of the non-CARS signals, particularly the reflection of the pump beam. Even using the same set of filters as used in the F-CARS setup there still appeared spurious signals. We were also not able to see any signal from CARS beads in a near index matching oil. The images of the beads in water also looked like a strong CARS signal was coming from the upper surface of the bead. When these results are taken in conjunction it suggests that we may not be able to detect any backwards generated CARS signal with our setup, and we are just looking at a back reflected forward CARS signal. This may not be that surprising considering the phase matching requirements that show that the resonant CARS signal is generated in the same direction as the pump and Stoke lasers (see Figure 10). We also found that we needed to use high laser powers and long acquisition times to generate comparable images to our CARS setup which risks damaging both cells and particles.

9 Cellular imaging

Summary

In this chapter we explore the use of our CARS microscope to image a number of different cell types with and without added micro particles. We show that on resonance images taken in the C-H stretch region allow cells to be identified against the background solvent. Features that indicate lipid droplets and the nuclear membrane are often clearly visible due to high CARS signals from these regions. The nucleus is visible as a dip in signal levels at the centre of a cell. Off-resonant images provide only faint outlines of cells and some features, with most of the cell appearing similar to the background solvent.

We imaged both organic and inorganic micron and sub micron sized particles. Larger particles were visible in cells as individual beads, whereas the smaller sub micron sized particles were visible as regions of more intense CARS signal. By probing different Raman resonances we were able to isolate the added particles from broad resonant and non-resonant signals. Live cell imaging could be performed as well as 3D imaging to help explore the spatial and temporal relationships between particles and cells. These methods were used to estimate the volume of wear particles within the cells.

9.1 Imaging cells

We imaged a variety of cell types with the following setup: the Stokes laser was set at 1064 nm and the pump set between 817.1 and 817.3 nm to probe a Raman resonance around 2840 cm^{-1} in the lipid stretching region. The power of the laser was set approximately 30 mW for the Stokes laser and 20 mW for the pump laser. The gain was set between 6 and 7 in the Nikon C1 software, whilst the pixel dwell time was set between 30 and 61.44 μs. Unless otherwise stated, these settings are used in all the images measured throughout this chapter. The images obtained from cells are shown in Figure 90 and demonstrate a number of differences and similarities in CARS signals within these cells. In Figure 90 A, the HL-60 cells (a human promyelocytic leukemic cell line) have been differentiated into macrophage like cells using TPA. It has been reported that differentiation of these cells results in the formation of large lipid droplets[174] and these are clearly visible in the CARS image. The other cell types all contained lipid droplets but these were smaller and far less numerous than the HL-60 cells. In all cells it was clear that the signal from the nuclear region was lower than the rest of the cell, indicating that this region contains fewer lipid molecules than the cytoplasm of a cell. In Figure 90 C, it can be seen that many of the RAW 264.7 cells (a mouse leukaemic monocyte macrophage cell line) appear multi-nucleated, belying their osteoclast like nature.[175] Encircling the nucleus in many of the cell types (particularly noticeable in Figure 90 D and E) is a ring of higher intensity signal which may be the nuclear membrane. Inside the nuclear region there is some variability in signal. DNA and proteins produce Raman signals in the C-H stretch region as well as lipids and these may be contributing to the CARS signal in this region. It has also been hypothesized that larger CARS signals in the nuclear region may represent the presence of signalling lipids.[115]

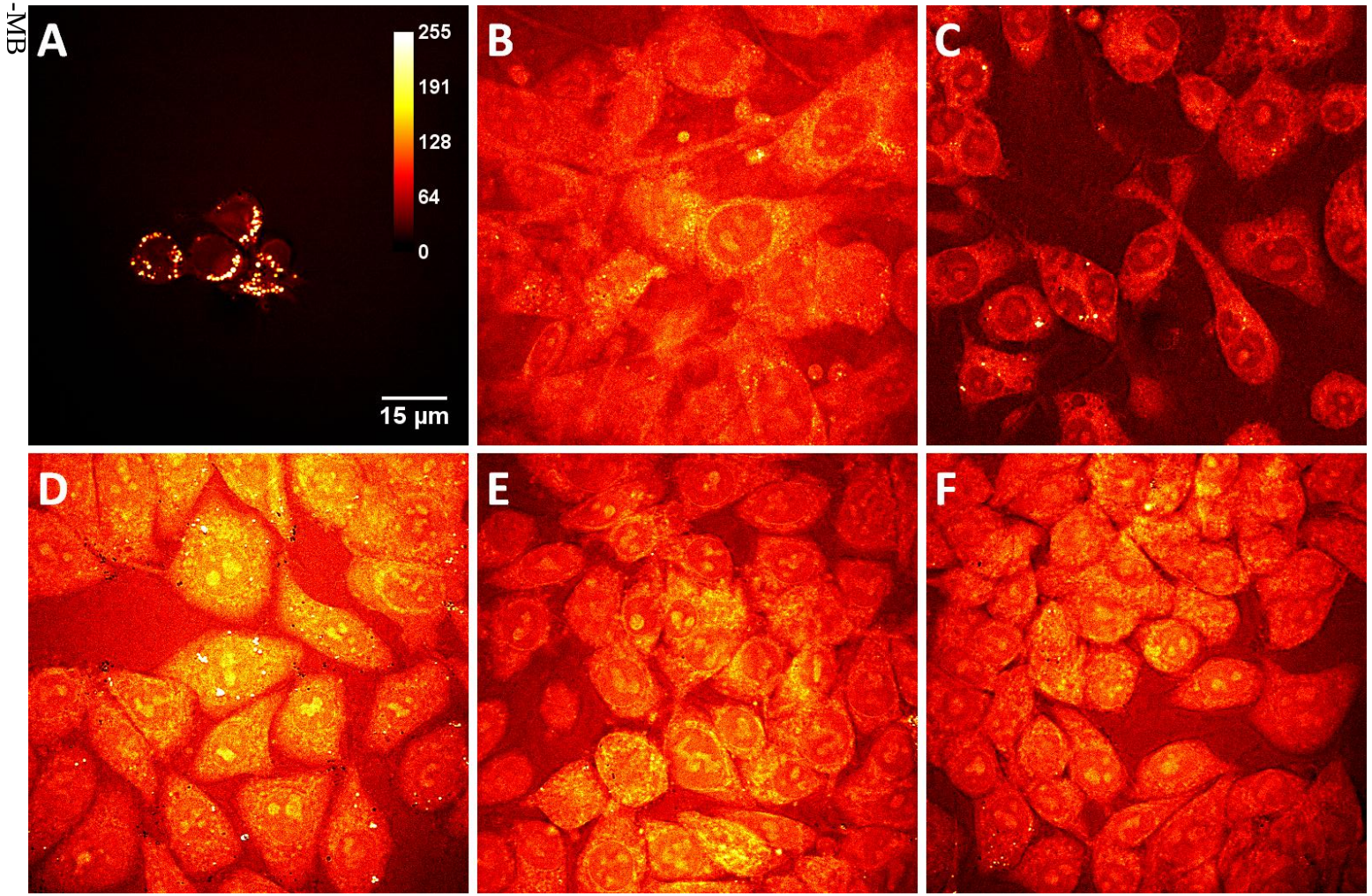

Figure 90 Forward CARS images of cells A. HL-60, B. NIH 3T3, C. RAW 264,.7 D. MCF 7, E. HEK 293 and F. MDA-MB 231 cells.

The images in Figure 91 have been taken at an off resonance frequency by adjusting the pump wavelength to 803.4 nm to probe a Raman resonance of 3060 cm^{-1}. At this wavelength the CARS image appears mostly uniform across the image with only faint outlines of the cell and some cellular components visible. The non-resonant background seems to be mostly uniform across the cell and the background solvent. This low level of signal in non-resonant images make them a good background to image particles against that contain a Raman peak that lies outside of the normal biological range.

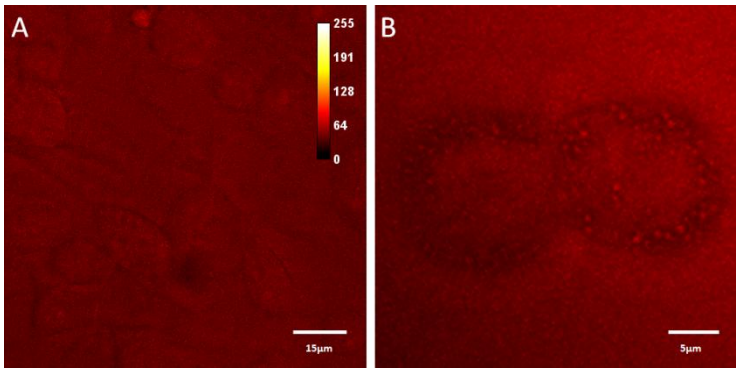

Figure 91 Forward CARS images of cells taken at an off resonance wavelength (3060 cm^{-1}), A. RAW 264.7 cells, B. HL-60 cells.

9.2 Z-stacks of cells

One of the most promising aspects of taking images of cells by CARS microscopy is that each image is optically sectioned due to the tight focussing constraints for four wave mixing to occur. By focusing the lasers at different depths through the cell, images can be recorded at different depths as shown in Figure 92. A full image stack can reveal information about the size, shape and structure of a cell.

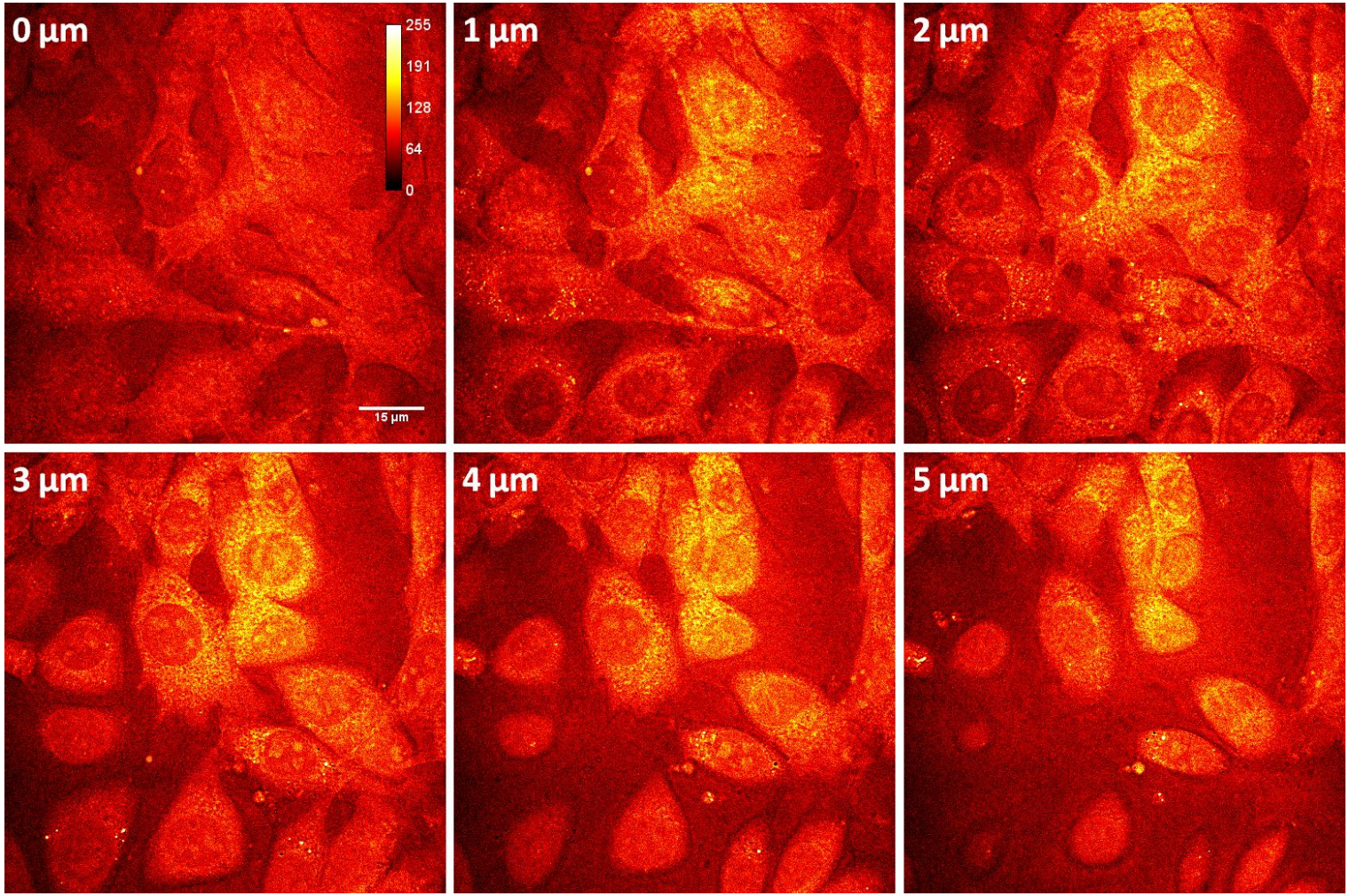

Figure 92 Forward CARS images of NIH 3T3 cells taken at increasing depths.

9.3 Imaging metal oxide particles in cells

It has previously been established that CARS is a useful tool to image metal oxide particles due to their broad four wave mixing response which allow them to be imaged at non-resonant wavelengths to aid visibility.[130,131,176] Cells that had been incubated with TiO_2 particles for 24 hours were imaged at two different wavelengths, 3060 cm^{-1} where only the TiO_2 particles are visible, and at 2850 cm^{-1} where cellular components rich in lipids are visible as well as the TiO_2 particles. Figure 93 shows *z*-projections of HL-60 cells taken at both wavelengths and the combined image where the areas that contain signals in both measured wavelengths show up in yellow. The inherent optical cross-sectioning of the CARS microscope also allows for the 3D localisation of particles in cells. Figure 94 shows TiO_2 particles in RAW 264.7 cells. The *xy* image is a *z*-projection whilst the *xz* and *yz* are images taken from a reslice of the image stack across the white dashed line.

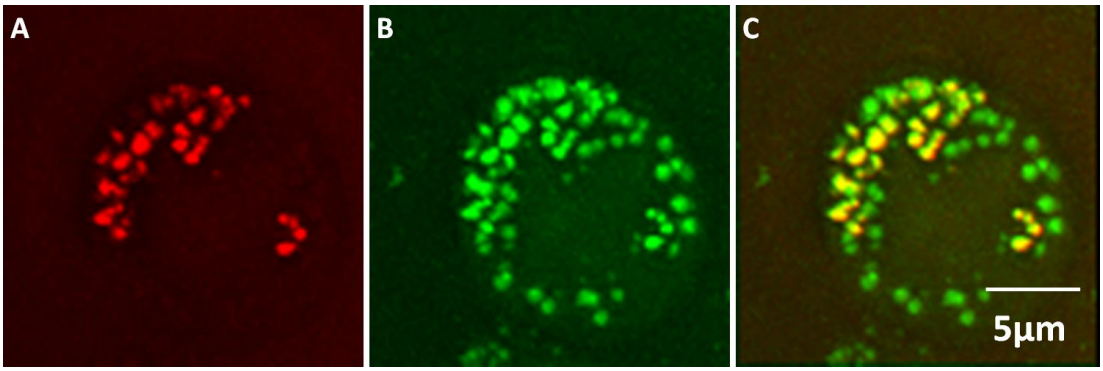

Figure 93 Forward CARS images of an HL-60 cell with TiO_2 particles. A. The red graded image is taken at 3060 cm^{-1}, showing only the TiO_2 particles in the cell. B. The green graded image is taken at 2850 cm^{-1} showing both lipid rich cell compartments as well as TiO_2 particles. C. Merged image of A and B, TiO_2 particles show up in both images so appear yellow whilst the cell components remain green.

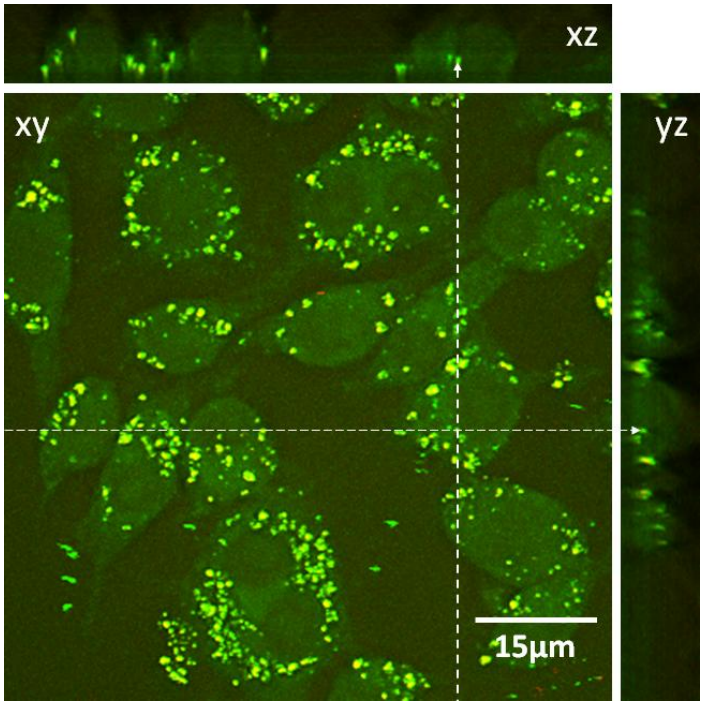

Figure 94 Multi-planar visualisation of F-CARS images of TiO_2 particles in RAW 264 cells. A red image (representing a CARS image take at 3060 cm^{-1}) and green image (representing a CARS image taken at 2850 cm^{-1}) have been overlaid on top of each other. Slices are taken from the recombined image stack along the white dotted lines. Arrows points to the particle found at the intersection of the two slices.

9.4 Imaging polystyrene particles in cells

Polystyrene particles of known sizes were incubated with RAW 264.7 or HL-60 cells macrophage cells. Working with polystyrene particles has many advantages to favour its use as a model particle with which to challenge cells, particularly when compared with polyethylene. The density of polystyrene is 1.05 g cm^{-1} which is heavier than water. This allows particles to sediment when mixed with growth media in tissue culture and enables interaction of cells with particles. Generating the same interactions with cells and polyethylene particles is not a trivial challenge; polyethylene has a density of only 0.97 g cm^{-1} so particles float away from cells in culture. Culture systems that encourage polyethylene-cell interactions usually require either an inverted culture setup,[48,77] or that particles are fixed to the surface of the culture vessel, usually in a gel, to help maintain particle-cell interactions.[177] Polystyrene also contains a strong Raman peak centred around 3060 cm^{-1}, (due to the C-H ring breathing – see chapter 4.1.2) that is not found in cells. This Raman peak

makes it easier to pick out the resonant polystyrene signals in CARS images. Polystyrene is also available in a number of micron and sub-micron size ranges which will allow us to assess the capabilities of our CARS system.

CARS images of RAW 264.7 cells treated for 24 hours with polystyrene beads were taken at the C-H stretch (ω_p-ω_s = 3052 cm^{-1}). The sensitivity of the detector was varied between samples giving rise to variable background intensities. Due to the length of time the cell was examined with the laser, fixed cells were used instead of live cells to prevent cell movement during imaging. Figure 95 shows *z*-projections of the imaging data taken through the *xy* plane. Larger polystyrene particles (1 μm and larger) as shown in Figure 95 A and B are individually recognizable in cells and found throughout the cell cytoplasm. Smaller polystyrene particles (less than 0.5 μm) as shown in Figure 95 C are no longer distinct as individual particles but found clustered in or around spherical regions inside of the cell. The 100 nm particles shown in Figure 95 D are only visible as discrete areas in the cell exhibiting a strong CARS signal. The variable signal intensity is likely due to a number of factors including depth in the stack at which the particle is imaged, the cellular environment it is located within, and interference with other scattering objects.

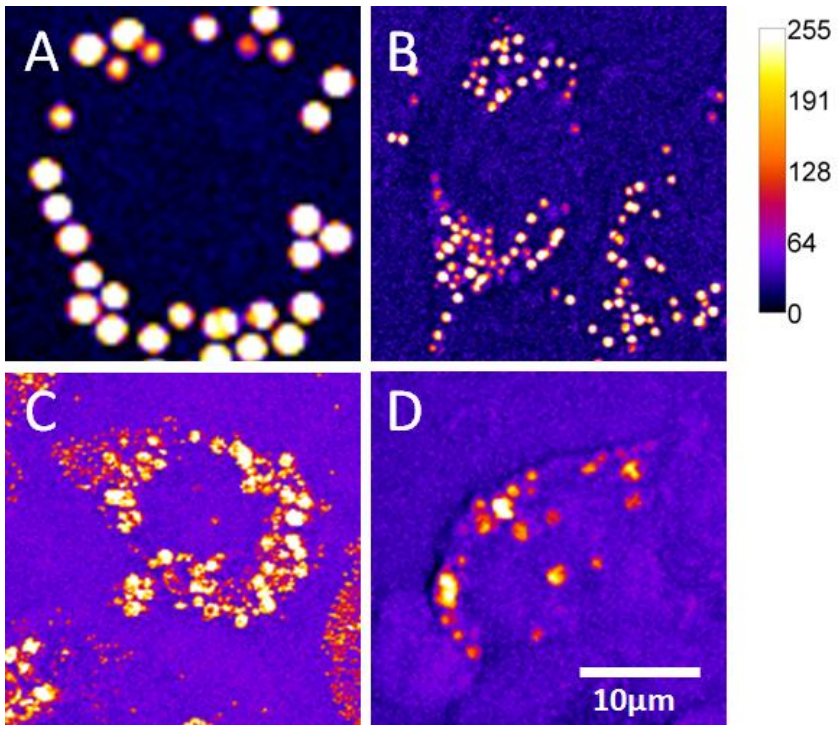

Figure 95 Forward CARS images of cells incubated with polystyrene particles. A. 3 µm, B. 1 µm, C. 0.5 µm, and D 100 nm polystyrene spheres.

Changes in the rate of phagocytosis as well as the location of the particles within cells can be tracked over time. We can achieve this either by monitoring a single field of cells over an extended time period to create a time lapse image of the process, or image cells from a batch treated the same way at different time periods. Both methods have their own advantages and drawbacks. Continually imaging a single sample will lead to a build up of photodamage within the cell as the laser light is continuously scanned over the cell. This will affect the normal physiological responses of the cell and eventually lead to cell death. Due to the slow rate of image acquisition, sequentially scanning will prevent taking image stacks at different depths due to the rate of cell movement. Cells from a batch all treated the same way can have a representative sample taken at different time points. This has the advantage that cells can be fixed and a full image stack can be acquired, although this means that each image stack is of different cells from a different batch.

Figure 96 shows some images captured from a time-lapse recording of a RAW 264.7 cell incubated with 1 µm polystyerene particles. The images were recorded with the pump and Stokes lasers tuned to the image the 2850 cm^{-1} vibration, to allow

visualisation of both the cell and the particle. The images were recorded at a rate of 1 image per 2 minutes. A single particle can be seen being phagocytosed by the cell.

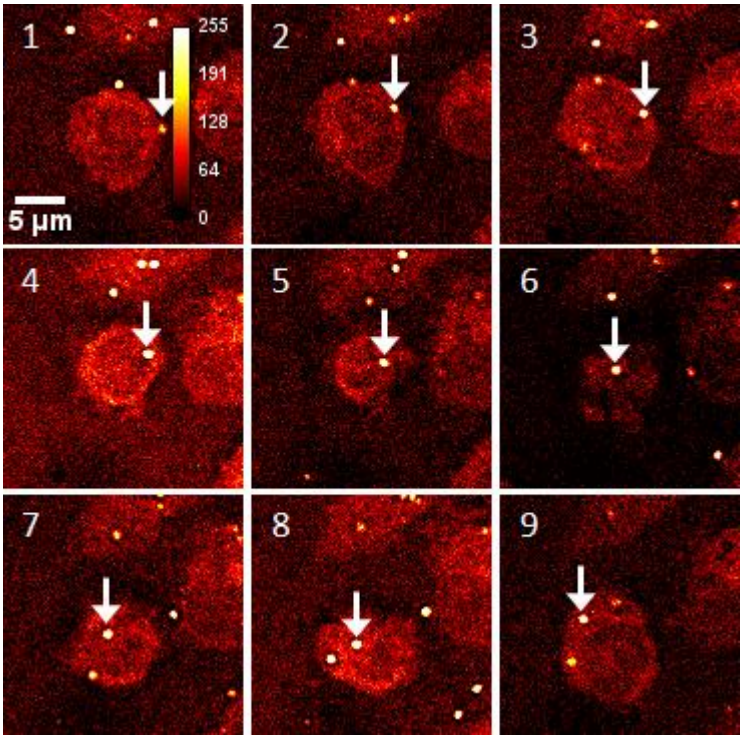

Figure 96 Forward CARS images of a single RAW 264.7 cell phagocytosing a 1 µm polystyrene bead indicated by the arrow. Taken from a time lapse recording lasting 4 hours.

Figure 97 shows images taken from RAW 264.7 cells that had been incubated with polystyrene. At the time points noted a batch of cells was removed, washed and then fixed before imaging in the CARS microscope. Images were recorded at both 2850 and 3060 cm^{-1}. Although individual cells could not be tracked over time, this method does give an idea as to the rate at which particle ingestion is occurring, and where the particles end up in the cell as image stacks can be recorded. It can be seen that even after 1 hour, some particles have already been phagocytosed into the cells. At 3 hours it is clear that small clusters of particles are forming in the cytoplasm. As time progresses, the CARS signal from these regions increases suggesting more particles are being stored there. No particles are found in the nuclear region.

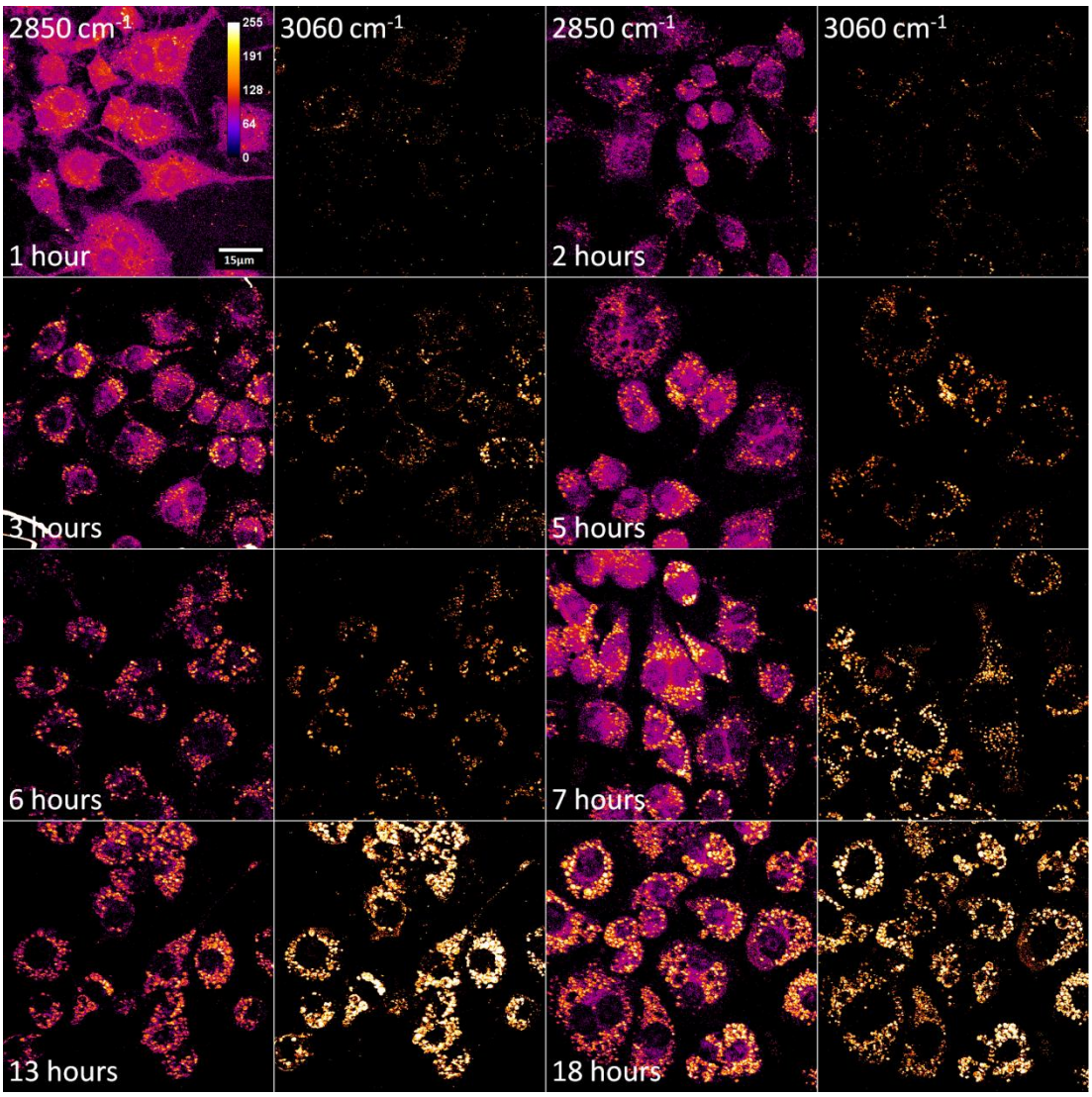

Figure 97 Forward CARS images of RAW 264.7 cells incubated with 0.3 µm polystyrene particles. Image intensities below a manually defined threshold were removed. Number of hours after incubation with particles is listed on the left of the two images, one taken with ω_p-ω_s tuned to 2850 cm^{-1} and one at 3060 cm^{-1}. All images are matched pairs except for those taken at 7 hours.

9.5 Forward vs epi-detected CARS in particle imaging

The results obtained in (Figure 89) showed that epi-detected CARS setup showed some suppression of CARS signal from large scattering objects. However, it required longer exposure times and more laser power to generate CARS signals of a similar level to a F-CARS image. Investigating the use of epi-detected CARS as the detection setup for imaging particles within cells was still worth investigating as it

was still possible that the suppression of large scattering objects could help generate better contrast for the particles in cells.

We used HL-60 cells that had been differentiated with 1 nM TPA for 24 hours and then incubated with polystyrene particles for 24 hours as our model cell. Images were taken with both forward and epi-detected geometries and shown as *z*-projections in Figure 98. Although the laser power was kept constant between the two imaging geometries, the pixel dwell time was doubled for the epi-detected CARS images and the gain setting was set higher.

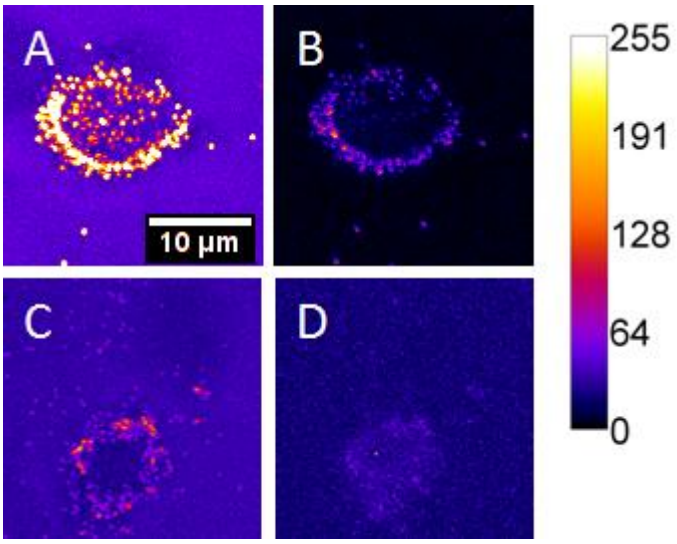

Figure 98 Projections of forward and epi-detected CARS images of HL-60 cells incubated with polystyrene particles taken at 3060 cm^{-1}. With 0.75 µm particles: A. Forward CARS, B. Epi CARS. With 0.5 µm particles: C. Forward CARS. D. Epi-detected.

The E-CARS signals for the 0.75 µm particles were much lower than for the forward scattered detection, although they were still visible. It is hard to directly compare these two images due to both a different background and signal level levels. For the 0.5 µm particles however, the situation is clearer. The E-CARS images showed almost no signal above the background levels, whilst the F-CARS images showed clearly visible CARS signals in the same cells.

It should also be noted that whilst many particles clustering together help generate a stronger signal in the forward CARS image due to constructive interference. This same interference is destructive in the epi-detected CARS signal. Although epi

detected CARS may be a more suitable technique for viewing individual particles, as some authors have suggested[133] this may not be true when particles cluster together.

9.6 CARS images of polyethylene in RAW 264.7 cells.

Incubating polyethylene with cells poses a number of challenges, the most notable of which is that the density of UHMWPE is lower than water. Although some groups have incubated cells with polyethylene with only simple mixing,[46] we found that using this method we could not find polyethylene in cells when imaged. We found that the easiest way to ensure cells were kept in contact with polyethylene was to coat the culture surface in a sonicated mixture of polyethylene particles and distilled water, wait for the solvent to evaporate off, and then gently lay a cell suspension over the top. Although this is not ideal for an even distribution of particles due to hydrophobic interactions and capillary force effects during drying encouraging agglomeration of polyethylene particles, it will still allow us to test our CARS microscope.

RAW 264.7 cells were plated onto glass bottomed dishes that contained polyethylene particles from either commercial polyethylene powder or polyethylene from a pin-on-plate wear simulator. After a 24 hour incubation period, CARS images were taken at the 2850 cm^{-1} CH_2 vibrational mode. Figure 99 shows *z*-projections of the cells. The commercial polyethylene powder appeared as large, regular shaped particles within cells with a very high CARS signal compared to the rest of the cell as shown in Figure 99 A. Cells treated with submicron sized debris from a wear simulator are shown in Figure 99 B. This image shows many discrete areas of high CARS signal ranging up to almost 6 μm in diameter that we attributed to the phagocytosed polyethylene. They were mostly spherical in shape with slightly irregular borders, similar to what we have previously observed with model particles of polystyrene.[178]

A current limitation of our system is that we are only able to record images from cells in the C-H stretching region rather than the full biological range of the Raman spectra. Within this C-H region the Raman spectra of lipids and polyethylene are very similar (see results in chapter 4.1.1 and 4.2 to compare). At the present moment we cannot say with certainty that the larger CARS signals are definitely caused be

polyethylene rather than other CH_2 containing structures such as lipids. Expanding the usable range in the biological Raman region should allow clearer differentiation between these compounds within the cell.

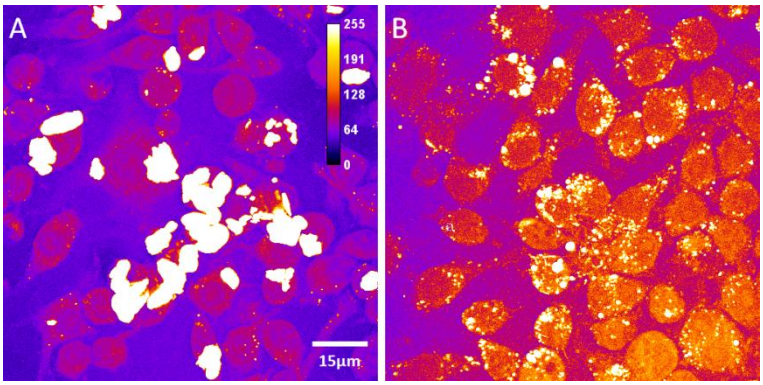

Figure 99 Forward CARS images of RAW 264.7 cells with: A. Polyethylene powder. B. Polyethylene from a pin-on-plate wear simulator.

As the polyethylene signal is so much larger compared to the CARS signal from the cell, it is possible to adjust the gain or the pixel dwell time to highlight the polyethylene particles. In Figure 100 the gain has been lowered from the images recorded in Figure 99. This helps remove the signal from the solvent and cells and highlight the details in the polyethylene particles.

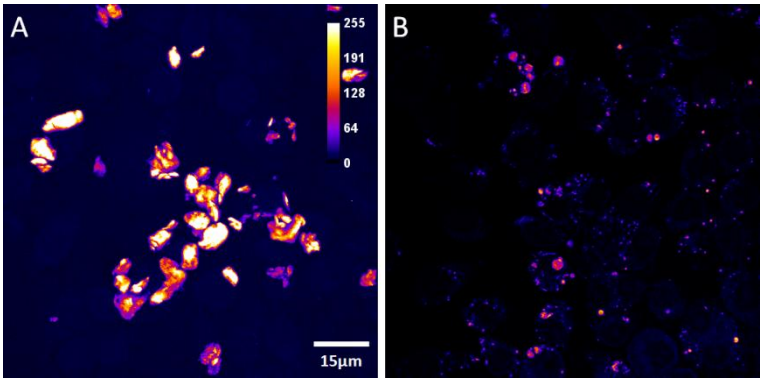

Figure 100 Forward CARS images of RAW 264.7 cells, same as Figure 99 but with a lower gain setting in the recording software.

9.7 Using CARS to estimate wear debris volumes

As CARS has inherent 3D optical sectioning properties due to its multiphoton nature we were able to estimate the volume of particles found inside of a cell from image stacks. The process involves isolating single cells from an image stacks using a

manually drawn mask around the outline of the cell to isolate it from the rest of the image. The signal levels in the single cells are then thresholded into three different bins indicating: low, medium and high CARS signal. An example of this is shown in Figure 101. The threshold for the low signal was adjusted to only include areas of the background. The medium threshold included the cell, whilst the high threshold was adjusted to represent areas of high CARS signal that indicate polyethylene. This is done for all images in the stack, and the number of pixels in each bin for each cell is counted. A volume for each pixel is calculated using the inter-stack image spacing as well as the pixel area.

It should be noted that as CARS is a coherent process the standard deconvolution process which help to correct the image produced due to focal spot sizes in a confocal microscope[179] system are not valid for a coherent process.[92] It is likely that we are over estimating the volumes measured due to this.

We measured 10 cells and found a mean measured volume of the entire cell (red and white pixels in Figure 101) to be 519 μm^3 ± 107 μm^3. The volume of particles inside the cell (white pixels in Figure 101) ranged from 10 μm^3 to 101 μm^3. The most particle heavy cell consisted of over 25% ingested particles compared to cell volume.

Although we tested only a limited number of cells and the variation in our case is likely due to the culture conditions with many particles pre-agglomerated. It does demonstrate that CARS could be used to assess particle loads in cells. This information could be used to improve *in vitro* culture conditions by measuring the evenness of particle distributions as well as identifying sub populations of macrophages that are more active. This could also be applied to *ex vivo* samples or, given the sufficient development of fibre launched CARS systems,[180,181] may be used to directly measure the wear load in patient tissue around prosthetic joints.

Figure 101 Thresholding of a single cell. This is shown as a projected image for clarity. The thresholds are coloured as follows: low-signal is coloured black and represents the non-cell areas; medium-signal is coloured red, and represents the normal cell contents; high-signal is coloured white and shows the areas of the cell that are thought to contain ingested polyethylene particles.

9.8 Improving CARS image quality

The sharp peaks in the polyethylene spectrum suggest another possible method to improve imaging contrast by removing unwanted resonant and non-resonant signals from the image. Taking two images that lie on and off the polyethylene resonance peak but are separated by only a few tens of wavenumbers and subtracting them from each other removes the broader resonant responses (from proteins, lipids etc) as well as the non-resonant solvent signals. Figure 102 shows CARS images collected from cells treated with polyethylene taken on a resonance peak at 2850 cm^{-1} and off resonance at 2870 cm^{-1}. Subtracting the off resonance image from the on resonance image, as shown in Figure 102 C, gives greatly improved contrast due to the removal of the broader unwanted signals, although it is likely that some sharp resonant features from the cell will remain.

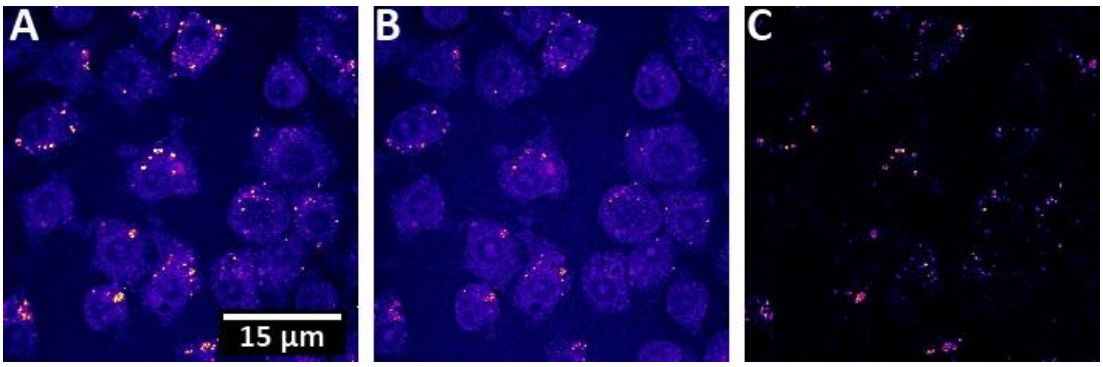

Figure 102 F-CARS images of RAW 264.7 cells treated with polystyrene. A and B. On and off polyethylene resonant peak images taken at 2850 and 2870 cm^{-1} respectively. C. Difference of the two images which removes the broad resonant and non-resonant signals from unwanted compounds within the cell and surrounding solvent.

9.9 Using CARS to image multiple compounds

The ability of CARS to distinguish between specific chemical compounds due to the unique vibrational resonances will be key in completely isolating the chemical signal of interest from similar compounds. We demonstrate the ability of CARS to distinguish between three separate polymeric compounds added to a cell. Cells were incubated for 24 hours with a mixture of PMMA, polyethylene and polystyrene and then imaged at 2950 cm^{-1}, 2850 cm^{-1} and 3060 cm^{-1}. These three wavenumbers corresponded to vibrational peaks in the three compounds respectively. We also imaged and then subsequently subtracted an off resonance image taken by adjusting the pump laser a few nanometres away from resonance for each image to remove unwanted background signals. Figure 103 A, B and C shows the separate images of each wavelength in the field of view. A zoomed in image from the white boxed region is shown in Figure 103 D. This combined image of single cell shows clear identification of individual particles and compounds in the cell in 3D.

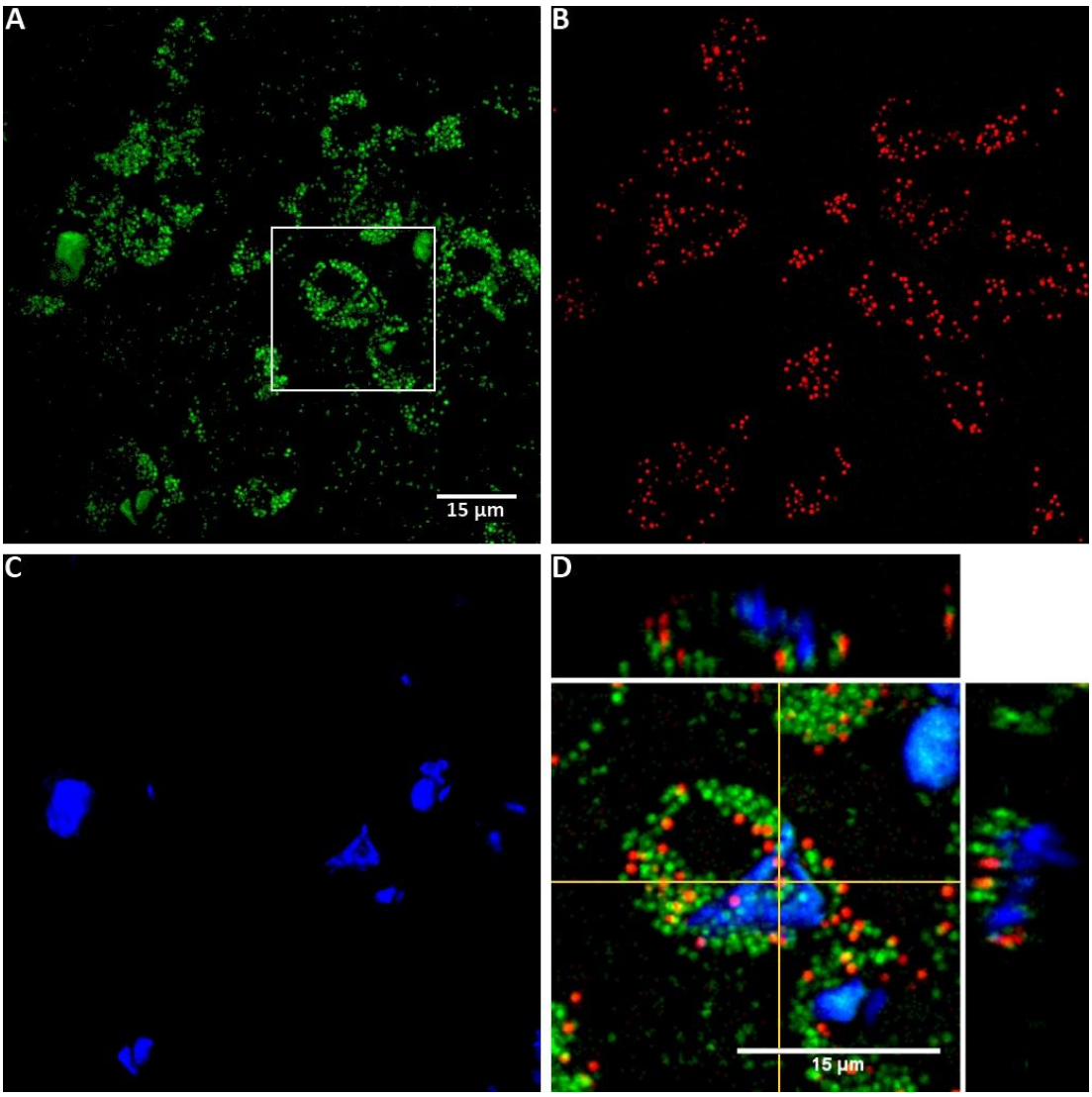

Figure 103 F-CARS images of RAW 264.7 cells treated with PMMA, polystyrene, and polyethylene. A. Image taken at 2950 cm^{-1} showing mainly PMMA particles but also some faint traces of the polyethylene. (Image D. is taken from the area in the white box). B. Image taken at 3060cm^{-1} the ring breathing mode of polystyrene. C. Image taken at 2850 cm^{-1} showing the location of polyethylene. D. Multi-planar visualization of the combined wavelengths in a single cell. Slices are taken from the recombined image stack along the yellow lines.

9.10 Conclusions

We have demonstrated that CARS microscopy can be used to examine cells by imaging in the C-H stretch region that occurs in lipid molecules. This allows the identification of cellular features against the non-resonant solvent background and can provide a cell outline to image other features against. We imaged a number of

different micro particles, including the metal oxide TiO_2 as well as polymeric compounds such as polystyrene, PMMA and polyethylene.

TiO_2 particles incubated with cells could clearly be seen at off-resonant frequencies due to the broad nature of the two-photon electronic excitation. Combining on and off resonant images graded in different colours allowed metal oxide particles to be highlighted by the mixed colour against the cell contents, aiding identification.

Polystyrene was used as a model non-metallic particle due to the 3060 cm^{-1} vibration that did not occur in cells. This allowed for identification of particles against a non-resonant background. Large particles were visible individually, whilst those smaller than 0.5 μm were no longer seen as individual particles. We were able to see CARS signals from discrete areas of the cell even when using 100 nm polystyrene particles.

CARS is a particularly suitable choice when dealing with polyethylene materials from surgical components whose function and performance could be altered by introducing a labelled tag, or where an alternative material would require approval by regulating bodies. We were able to image both commercial polyethylene particles, as well as those generated by our wear simulator. Using images taken at different vibrational resonances we were able to construct a chemical map of the contents of a cell as well as quantifying the amount of material found in a cell.

10 Conclusions and further work

We demonstrated that with our pin-on-plate wear simulator, the pattern of motion of the pins against the plate was responsible for changes in the size and shape of wear particles produced. A linear pattern of motion produced wear particles that were larger than those isolated from revision tissue. Particles produced using an elliptical pattern of wear were a closer match, and were subsequently used to challenge macrophage cells.

It is clear from the sizes of wear particles we found and their abrupt cut off at the size of the pore filter used (0.1 μm) that there could be smaller wear particles contained in the samples. Tipper, et al[182] reported that the found particles as small as 10 nm in simulator studies. Using a 0.015 μm filter would help identify if these smaller particles are present. We also had samples from many different points in the wear life cycle, and measuring how these particles change in size and morphology as the joint ages could indicate when the more active, smaller particles are produced.

We started building up a library of Raman data for cells and cellular components. These were used to identify Raman resonances that could be used as a CARS imaging mode. Improving this data using proper spectroscopic standards to calibrate the results both in terms of magnitude and wavelength would improve the accuracy of this library and allow it to be compared with the results from other instruments.[183,184]

Measuring the Raman spectra of the more commonly occurring lipids such as phosphatidyl serine, phosphatidyl choline, sphingomyelin, phosphatidyl inositol may also help to provide Raman vibrations in other regions that could be used to distinguish these molecules from polyethylene, allowing for a more accurate assessment of where these particles are found within cells.

The versatility of our CARS microscopy setup was also shown by using another multiphoton approach, TPEF, to image fluorescently tagged particles. Future studies on revision tissue will benefit from using other modes of imaging to increase the amount of information that can be extracted from each tissue sample. SHG has been used to image collagen fibres, elastin and microtubules,[86,185-188] whilst TPEF can be

used to image both auto fluorescent molecules as well as targeting proteins of interest with tags.[85,189,190]

The model particle work showed that the F-CARS signal for all sizes of particle was much larger than the E-CARS signal. Although some of this difference is expected from theoretical calculations, the placement of the detectors may also have a large effect on the collected signal. By moving the detectors closer to the sample, instead of using fibre optic couplings it is possible we will see larger collected signals from both E- and F-CARS setups. It may also alter the results and show that using E-CARS results in a better background rejection which enables high contrast imaging. However, as we have shown particles in cells are usually found aggregated together rather than as uniformly distributed single particles. Repeating our particle work with multiple particles collected in a gel matrix will help show how the E-CARS and F-CARS signals change in a model that more closely represents how particles are packed in cells.

CARS microscopy has been used to examine cells treated with micron and sub micron particles from both commercial polystyrene particles as well as polyethylene particles from a pin-on-plate wear simulator. Using CARS spectroscopy to generate contrast based on vibrational resonances negates the need for using external tag molecules when examining samples. This makes CARS a suitable choice when dealing with materials whose function and performance could be altered by introducing a labelled tag, or where an alternative joint material would require approval by regulating bodies. Both of these factors are particularly relevant when studying surgical implants.

Using the inherent properties of a multiphoton technique to allow good optical sectioning, we acquired high-quality three-dimensional images at different vibrational resonances, allowing us to construct a chemical map of the contents of a cell as well as quantifying the amount of material found in a cell.

Deuterated compounds which contain Raman resonances in the silent region of the Raman spectrum between 2000 – 2400 cm^{-1} have been used to help minimise unwanted resonant contributions to CARS images and isolate a particular compound

against other vibrational resonances.[163] A deuterium labelled polyethylene could help to further validate the results generated.

Optimising the system to take CARS images over the entire range of the biological Raman spectra will help identify more cellular components and provide better characterisation of materials in a cell. Combining this with imaging of periprosthetic tissue taken from revision surgery will yield valuable data on the spatial localisation of wear debris and its distribution in the cells and stroma.

Polymeric compounds can also be used to tag structures in the cell, or as a carrier for drugs. Encapsulated melamine and polystyrene microspheres within targeted liposomes have been used as a CARS label for monitoring endocytosis.[191] Similarly, drug delivery has been examined by using polymeric particles, that physically encapsulate the drug, which can be tracked by CARS.[163] Although this still leaves a question of how to monitor the actual drug release or transfer.[192]

CARS could also be used to monitor a number of other toxic particles, especially those where the size and possible mechanisms of action would be altered by adding tag molecules. As well as metal oxides, carbon nanotubes have been shown to damage DNA.[193] The Raman band at 1590 cm^{-1} could be a target.[194]

Interest in label free vibrational imaging and the promising results from CARS has also led to development of a related technique called Stimulated Raman Scattering (SRS). Like CARS, SRS uses two lasers (referred to as pump and Stokes for continuity) where the difference is tuned to a vibrational mode of interest. However, in SRS either the pump or Stokes beam is either amplitude or frequency modulated. The change in intensity of the unmodulated beam is then measured to give a SRS image.[195] The advantage of SRS is that it is free of the unwanted non-resonant background that affects CARS images. Furthermore, rather than a quadratic relationship to the number of oscillators within the focal point, the SRS is linearly proportional to the concentration of the oscillators. This could allow more accurate quantification of the chemical concentrations responsible for the signal.[195] SRS has also been reported to be a more sensitive than CARS and has shown promise in imaging nucleic acids,[196] as well as drugs in-vivo.[197]

11 References

1. Kleinfeld D, Mitra PP, Helmchen F, Denk W. Fluctuations and stimulus-induced changes in blood flow observed in individual capillaries in layers 2 through 4 of rat neocortex (vol 95, pg 15741, 1998). Proceedings of the National Academy of Sciences of the United States of America 1999;96(14):8307-8307.
2. Narvani AA, Tsiridis E, Tai CC, Thomas P. Acetabular labrum and its tears. Br J Sports Med 2003;37(3):207-11.
3. Tan CK, Wong WC. Absence of the ligament of head of femur in the human hip joint. Singapore Med J 1990;31(4):360-3.
4. Anderson K, Strickland SM, Warren R. Hip and groin injuries in athletes. Am J Sports Med 2001;29(4):521-33.
5. Hewitt J, Guilak F, Glisson R, Vail TP. Regional material properties of the human hip joint capsule ligaments. Journal of Orthopaedic Research 2001;19(3):359-64.
6. Bergmann G, Graichen F, Rohlmann A. Hip joint loading during walking and running, measured in two patients. J Biomech 1993;26(8):969-90.
7. Croft P, Coggon D, Cruddas M, Cooper C. Osteoarthritis of the hip: an occupational disease in farmers. BMJ 1992;304(6837):1269-72.
8. Wieland HA, Michaelis M, Kirschbaum BJ, Rudolphi KA. Osteoarthritis - an untreatable disease? Nat Rev Drug Discov 2005;4(4):331-44.
9. Sibanda N, Copley LP, Lewsey JD, Borroff M, Gregg P, MacGregor AJ, Pickford M, Porter M, Tucker K, van der Meulen JH and others. Revision Rates after Primary Hip and Knee Replacement in England between 2003 and 2006. Plos Medicine 2008;5(9):1398-1408.
10. Centre N. National Joint Registry for England and Wales 8th Annual Report (2010).
11. Cooper C, Campion G, Melton LJ, 3rd. Hip fractures in the elderly: a world-wide projection. Osteoporos Int 1992;2(6):285-9.
12. Excellence NIfHaC. The management of hip fracture in adults. 2011.
13. Center JR, Nguyen TV, Schneider D, Sambrook PN, Eisman JA. Mortality after all major types of osteoporotic fracture in men and women: an observational study. Lancet 1999;353(9156):878-82.
14. De Laet CE, van Hout BA, Burger H, Hofman A, Pols HA. Bone density and risk of hip fracture in men and women: cross sectional analysis. BMJ 1997;315(7102):221-5.
15. Lewinnek GE, Kelsey J, White AA, 3rd, Kreiger NJ. The significance and a comparative analysis of the epidemiology of hip fractures. Clin Orthop Relat Res 1980(152):35-43.

16. Berry DJ, Harmsen WS, Cabanela ME, Morrey BF. Twenty-five-year survivorship of two thousand consecutive primary Charnley total hip replacements: factors affecting survivorship of acetabular and femoral components. Journal of Bone & Joint Surgery - American Volume 2002;84-A(2):171-7.

17. Wessinghage D. [Themistocles Gluck. 100 years artificial joint replacement]. Z Orthop Ihre Grenzgeb 1991;129(5):383-8.

18. Amstutz HC. Hip Arthroplasty; 1991.

19. Heisel C, Silva M, Schmalzried TP. Bearing surface options for total hip replacement in young patients. Instructional Course Lectures 2004;53:49-65.

20. Nercessian OA, Wu WH, Sarkissian H. Clinical and radiographic results of cementless AML total hip arthroplasty in young patients. J Arthroplasty 2001;16(3):312-6.

21. Jacobsen S, Jensen FK, Poulsen K, Sturup J, Retpen JB. Good performance of a titanium femoral component in cementless hip arthroplasty in younger patients: 97 arthroplasties followed for 5-11 years. Acta Orthop Scand 2003;74(4):375-9.

22. Smith AJ, Dieppe P, Vernon K, Porter M, Blom AW, Wales NJRE. Failure rates of stemmed metal-on-metal hip replacements: analysis of data from the National Joint Registry of England and Wales. Lancet 2012;379(9822):1199-1204.

23. NJR Centre. National Joint Registry for England and Wales 8th Annual Report (2010).

24. Kurtz S, Ong K, Lau E, Mowat F, Halpern M. Projections of primary and revision hip and knee arthroplasty in the United States from 2005 to 2030. J Bone Joint Surg Am 2007;89(4):780-5.

25. Giori NJ. Unexpected finding of a fractured metal prosthetic femoral head in a nonmodular implant during revision total hip arthroplasty. J Arthroplasty 2010;25(4):659 e13-5.

26. Jaffe WL, Manley MT. Late fatigue fracture of a modern cemented forged cobalt chrome stem for total hip arthroplasty: a report of 10 cases. J Arthroplasty 2006;21(7):1080; author reply 1080-1.

27. Garvin KL, Hanssen AD. Current Concepts Review Infection after Total Hip-Arthroplasty Past, Present, and Future. Journal of Bone and Joint Surgery-American Volume 1995;77(10):1576-1588.

28. Herberts P, Malchau H. Long-term registration has improved the quality of hip replacement: a review of the Swedish THR Register comparing 160,000 cases. Acta Orthop Scand 2000;71(2):111-21.

29. Ulrich SD, Seyler TM, Bennett D, Delanois RE, Saleh KJ, Thongtrangan I, Kuskowski M, Cheng EY, Sharkey PF, Parvizi J and others. Total hip arthroplasties: what are the reasons for revision? Int Orthop 2008;32(5):597-604.

30. Gomez PF, Morcuende JA. Early attempts at hip arthroplasty--1700s to 1950s. Iowa Orthop J 2005;25:25-9.

31. Hornbogen E, Karsch UA. Frictional Wear of Polytetrafluoroethylene (Ptfe). Journal of Materials Science Letters 1983;2(12):777-780.

32. Charnley J. Tissue Reactions to Polytetrafluorethylene. The Lancet 1963;282(7322):1379-1379.

33. Gomez PF, Morcuende JA. A historical and economic perspective on Sir John Charnley, Chas F. Thackray Limited, and the early arthoplasty industry. Iowa Orthop J 2005;25:30-7.

34. Sundfeldt M, Carlsson LV, Johansson CB, Thomsen P, Gretzer C. Aseptic loosening, not only a question of wear: a review of different theories. Acta Orthop 2006;77(2):177-97.

35. Abu-Amer Y, Darwech I, Clohisy JC. Aseptic loosening of total joint replacements: mechanisms underlying osteolysis and potential therapies. Arthritis Res Ther 2007;9 Suppl 1:S6.

36. Ingham E, Fisher J. The role of macrophages in osteolysis of total joint replacement. Biomaterials 2005;26(11):1271-86.

37. Archibeck MJ, Jacobs JJ, Roebuck KA, Glant TT. The basic science of periprosthetic osteolysis. Instructional Course Lectures 2001;50:185-95.

38. Ingham E, Fisher J. Biological reactions to wear debris in total joint replacement. Proceedings of the Institution of Mechanical Engineers. Part H - Journal of Engineering in Medicine 2000;214(1):21-37.

39. Santerre JP, Labow RS, Boynton EL. The role of the macrophage in periprosthetic bone loss. Canadian Journal of Surgery 2000;43(3):173-9.

40. Clohisy D. Cellular mechanisms of osteolysis. J Bone Joint Surg Am 2003;85-A Suppl 1:S4-6.

41. Adamopoulos IE, Sabokbar A, Wordsworth BP, Carr A, Ferguson DJ, Athanasou NA. Synovial fluid macrophages are capable of osteoclast formation and resorption. Journal of Pathology 2006;208(1):35-43.

42. Pederson L, Ruan M, Westendorf JJ, Khosla S, Oursler MJ. Regulation of bone formation by osteoclasts involves Wnt/BMP signaling and the chemokine sphingosine-1-phosphate. Proc Natl Acad Sci U S A 2008;105(52):20764-9.

43. Silva M, Shepherd EF, Jackson WO, Dorey FJ, Schmalzried TP. Average patient walking activity approaches 2 million cycles per year: pedometers under-record walking activity. J Arthroplasty 2002;17(6):693-7.

44. Urban RM, Jacobs JJ, Tomlinson MJ, Gavrilovic J, Black J, Peoc'h M. Dissemination of wear particles to the liver, spleen, and abdominal lymph nodes of patients with hip or knee replacement. J Bone Joint Surg Am 2000;82(4):457-76.

45. Neale SD, Sabokbar A, Howie DW, Murray DW, Athanasou NA. Macrophage colony-stimulating factor and interleukin-6 release by periprosthetic cells stimulates osteoclast formation and bone resorption. Journal of Orthopaedic Research 1999;17(5):686-94.

46. Smith RA, Hallab NJ. In vitro macrophage response to polyethylene and polycarbonate-urethane particles. J Biomed Mater Res A 2010;93(1):347-55.

47. Shanbhag AS, Kaufman AM, Alabre CI, Rubash HE. Human macrophage response to UHMWPE, TiAlV, CoCr, and alumina particles: Analysis of multiple cytokines using protein arrays. Journal of Biomedical Materials Research Part A 2008;84A(2):464-474.

48. Fang HW, Ho YC, Yang CB, Liu HL, Ho FY, Lu YC, Ma HM, Huang CH. Preparation of UHMWPE particles and establishment of inverted macrophage cell model to investigate wear particles induced bioactivites. Journal of Biochemical & Biophysical Methods 2006;68(3):175-87.

49. Ingram JH, Stone M, Fisher J, Ingham E. The influence of molecular weight, crosslinking and counterface roughness on TNF-alpha production by macrophages in response to ultra high molecular weight polyethylene particles. Biomaterials 2004;25(17):3511-22.

50. Huk OL, Zukor DJ, Antoniou J, Petit A. Effect of pamidronate on the stimulation of macrophage TNF-alpha release by ultra-high-molecular-weight polyethylene particles: a role for apoptosis. Journal of Orthopaedic Research 2003;21(1):81-7.

51. Petit A, Catelas I, Antoniou J, Zukor DJ, Huk OL. Differential apoptotic response of J774 macrophages to alumina and ultra-high-molecular-weight polyethylene particles. Journal of Orthopaedic Research 2002;20(1):9-15.

52. Matthews JB, Besong AA, Green TR, Stone MH, Wroblewski BM, Fisher J, Ingham E. Evaluation of the response of primary human peripheral blood mononuclear phagocytes to challenge with in vitro generated clinically relevant UHMWPE particles of known size and dose. J Biomed Mater Res 2000;52(2):296-307.

53. Voronov I, Santerre JP, Hinek A, Callahan JW, Sandhu J, Boynton EL. Macrophage phagocytosis of polyethylene particulate in vitro. Journal of Biomedical Materials Research 1998;39(1):40-51.

54. Murray DW, Rushton N. Macrophages stimulate bone resorption when they phagocytose particles. Journal of Bone & Joint Surgery - British Volume 1990;72(6):988-92.

55. Wooley PH, Morren R, Andary J, Sud S, Yang SY, Mayton L, Markel D, Sieving A, Nasser S. Inflammatory responses to orthopaedic biomaterials in the murine air pouch. Biomaterials 2002;23(2):517-26.

56. Yang SY, Ren W, Park Y, Sieving A, Hsu S, Nasser S, Wooley PH. Diverse cellular and apoptotic responses to variant shapes of UHMWPE particles in a murine model of inflammation. Biomaterials 2002;23(17):3535-43.

57. Wedemeyer C, Neuerburg C, Pfeiffer A, Heckelei A, von Knoch F, Hilken G, Brankamp J, Henschke F, von Knoch M, Loëe F and others. Polyethylene Particle-Induced Bone Resorption in Substance P-Deficient Mice. Calcified Tissue International 2007;80(4):268-274.

58. Hansen T, Otto M, Buchhorn GH, Scharnweber D, Gaumann A, Delank KS, Eckardt A, Willert HG, Kriegsmann J, Kirkpatrick CJ. New aspects in the histological examination of polyethylene wear particles in failed total joint replacements. Acta Histochem 2002;104(3):263-9.

59. Lee JM, Salvati EA, Betts F, DiCarlo EF, Doty SB, Bullough PG. Size of metallic and polyethylene debris particles in failed cemented total hip replacements. J Bone Joint Surg. Br. 1992;74(3):380-4.

60. Pazzaglia UE, Dell'Orbo C, Wilkinson MJ. The foreign body reaction in total hip arthroplasties. A correlated light-microscopy, SEM, and TEM study. Arch Orthop Trauma Surg. 1987;106(4):209-19.

61. Bos I. Histological investigation of polyethylene particles in total hip replacement: ceramic versus metal heads. Hip International 2000;10(3):151-160.

62. Morawietz L, Classen RA, Schroder JH, Dynybil C, Perka C, Skwara A, Neidel J, Gehrke T, Frommelt L, Hansen T and others. Proposal for a histopathological consensus classification of the periprosthetic interface membrane. J Clin Pathol 2006;59(6):591-7.

63. Koopman R, Schaart G, Hesselink MK. Optimisation of oil red O staining permits combination with immunofluorescence and automated quantification of lipids. Histochem Cell Biol 2001;116(1):63-8.

64. Zaloudek C, Treseler PA, Powell CB. Postarthroplasty histiocytic lymphadenopathy in gynecologic oncology patients - A benign reactive process that clinically may be mistaken for cancer. Cancer 1996;78(4):834-844.

65. Elfick AP, Green SM, Krikler S, Unsworth A. The nature and dissemination of UHMWPE wear debris retrieved from periprosthetic tissue of THR. J Biomed Mater Res A 2003;65(1):95-108.

66. Affatato S, Fernandes B, Tucci A, Esposito L, Toni A. Isolation and morphological characterisation of UHMWPE wear debris generated in vitro. Biomaterials 2001;22(17):2325-31.

67. Richards L, Brown C, Stone MH, Fisher J, Ingham E, Tipper JL. Identification of nanometre-sized ultra-high molecular weight polyethylene wear particles in samples retrieved in vivo. J Bone Joint Surg Br 2008;90(8):1106-13.

68. Shanbhag AS, Jacobs JJ, Glant TT, Gilbert JL, Black J, Galante JO. Composition and Morphology of Wear Debris in Failed Uncemented Total Hip-Replacement. Journal of Bone and Joint Surgery-British Volume 1994;76B(1):60-67.

69. Visentin M, Stea S, Squarzoni S, Antonietti B, Reggiani M, Toni A. A new method for isolation of polyethylene wear debris from tissue and synovial fluid. Biomaterials 2004;25(24):5531-7.

70. Zolotarevova E, Entlicher G, Pavlova E, Slouf M, Pokorny D, Vesely F, Gallo J, Sosna A. Distribution of polyethylene wear particles and bone fragments in periprosthetic tissue around total hip joint replacements. Acta Biomaterialia;In Press, Corrected Proof.

71. Tipper JL, Ingham E, Hailey JL, Besong AA, Fisher J. Quantitative analysis of polyethylene wear debris, wear rate and head damage in retrieved Charnley hip prostheses. Journal of Materials Science: Materials in Medicine 2000;11:117-124.

72. Elfick AP, Green SM, Pinder IM, Unsworth A. A novel technique for the detailed size characterization of wear debris. J Mater Sci Mater Med 2000;11(5):267-71.

73. Zolotarevova E, Fejfarkova Z, Entlicher G, Lapcikova M, Slouf M, Pokorny D, Sosna A. Can centrifugation affect the morphology of polyethylene wear debris? Wear 2008;265(11-12):1914-1917.

74. Fisher J, Bell J, Barbour PSM, Tipper JL, Matthews JB, Besong AA, Stone MH, Ingham E. A novel method for the prediction of functional biological activity of polyethylene wear debris. Proc Inst Mech Eng H 2001;215(H2):127-132.

75. Green TR, Fisher J, Stone M, Wroblewski BM, Ingham E. Polyethylene particles of a 'critical size' are necessary for the induction of cytokines by macrophages in vitro. Biomaterials 1998;19(24):2297-302.

76. Shanbhag AS, Jacobs JJ, Black J, Galante JO, Glant TT. Macrophage/particle interactions: Effect of size, composition and surface area. Journal of Biomedical Materials Research 1994;28(1):81-90.

77. Matthews JB, Green TR, Stone MH, Wroblewski BM, Fisher J, Ingham E. Comparison of the response of primary human peripheral blood mononuclear phagocytes from different donors to challenge with model polyethylene particles of known size and dose. Biomaterials 2000;21(20):2033-44.

78. Brunette DM, Refai AK, Textor M, Waterfield JD. Effect of titanium surface topography on macrophage activation and secretion of proinflammatory cytokines and chemokines. Journal of Biomedical Materials Research Part A 2004;70A(2):194-205.

79. Grandjean-Laquerriere A, Laquerriere P, Guenounou M, Laurent-Maquin D, Phillips TM. Importance of the surface area ratio on cytokines production by human monocytes in vitro induced by various hydroxyapatite particles. Biomaterials 2005;26(15):2361-2369.

80. von Knoch M, Sprecher C, Barden B, Saxler G, Loer F, Wimmer M. Size and shape description of commercially available polyethylene particles for in vitro and in vivo experiments. Zeitschrift Fur Orthopadie Und Ihre Grenzgebiete 2004;142(3):366-370.

81. Matthaus C, Bergner G, Krafft C, Dietzek B, Lorkowski S, Popp J. Monitoring Intra-cellular Lipid Metabolism in Macrophages by Raman- and CARS-Microscopy. Proc SPIE 2010;7715:644.

82. van Manen HJ, Kraan YM, Roos D, Otto C. Single-cell Raman and fluorescence microscopy reveal the association of lipid bodies with phagosomes in leukocytes. Proc Natl Acad Sci U S A 2005;102(29):10159-64.

83. van Manen HJ, van Apeldoorn AA, Verrijk R, van Blitterswijk CA, Otto C. Intracellular degradation of microspheres based on cross-linked dextran hydrogels or amphiphilic block copolymers: a comparative raman microscopy study. Int J Nanomedicine 2007;2(2):241-52.

84. Chernenko T, Matthaus C, Milane L, Quintero L, Amiji M, Diem M. Label-free Raman spectral imaging of intracellular delivery and degradation of polymeric nanoparticle systems. ACS Nano 2009;3(11):3552-9.

85. Oheim M, Michael DJ, Geisbauer M, Madsen D, Chow RH. Principles of two-photon excitation fluorescence microscopy and other nonlinear imaging approaches. Advanced Drug Delivery Reviews 2006;58(7):788-808.

86. Mohler W, Millard AC, Campagnola PJ. Second harmonic generation imaging of endogenous structural proteins. Methods 2003;29(1):97-109.

87. Squier J, Muller M. High resolution nonlinear microscopy: A review of sources and methods for achieving optimal imaging. Review of Scientific Instruments 2001;72(7):2855-2867.

88. Beyond the diffraction limit. Nature Photonics 2009;3(7):361-361.

89. Eckbreth AC. BOXCARS: Crossed-beam phase-matched CARS generation in gases. Applied Physics Letters 1978;32(7):421-423.

90. Zumbusch A, Holtom GR, Xie XS. Three-Dimensional Vibrational Imaging by Coherent Anti-Stokes Raman Scattering. Physical Review Letters 1999;82(20):4142-4145.

91. Cheng J-X, Volkmer A, Xie XS. Theoretical and experimental characterization of coherent anti-Stokes Raman scattering microscopy. J. Opt. Soc. Am. B 2002;19(6):1363-1375.

92. Cheng J-X, Xie XS. Coherent Anti-Stokes Raman Scattering Microscopy: Instrumentation, Theory, and Applications. The Journal of Physical Chemistry B 2003;108(3):827-840.

93. Lotem H, Lynch RT, Bloembergen N. Interference between Raman resonances in four-wave difference mixing. Physical Review A 1976;14(Copyright (C) 2010 The American Physical Society):1748.

94. Evans CL, Xie XS. Coherent Anti-Stokes Raman Scattering Microscopy: Chemical Imaging for Biology and Medicine. Annual Review of Analytical Chemistry 2008;1(1):883-909.

95. Evans CL, Xie XS. Coherent anti-stokes Raman scattering microscopy: chemical imaging for biology and medicine. Annu Rev Anal Chem (Palo Alto Calif) 2008;1:883-909.

96. Begley RF, Harvey AB, Byer RL. Coherent anti-Stokes Raman spectroscopy. Applied Physics Letters 1974;25(7):387-390.

97. Cheng J-X, Volkmer A, Book LD, Xie XS. An Epi-Detected Coherent Anti-Stokes Raman Scattering (E-CARS) Microscope with High Spectral Resolution and High Sensitivity. The Journal of Physical Chemistry B 2001;105(7):1277-1280.

98. Volkmer A, Cheng J-X, Xie S. Vibrational Imaging with High Sensitivity via Epidetected Coherent Anti-Stokes Raman Scattering Microscopy. Physical Review Letters 2001;87:023901.

99. Djaker N, Gachet D, Sandeau N, Lenne P-F, Rigneault H. Refractive effects in coherent anti-Stokes Raman scattering microscopy. Appl. Opt. 2006;45(27):7005-7011.

100. Meier RJ, van der Pol A. A versatile aid in spectrum assignment: discriminating between fundamental and non-fundamental vibrational bands in Raman spectra. Vibrational Spectroscopy 2000;23(1):95-101.

101. Joshi J, Lehman R, Hall GS. Insight into the Molecular Arrangement of High-Density Polyethylene Polymer Chains in Blends of Polystyrene/HighDensity Polyethylene from Differential Scanning Calorimetry and Raman Techniques. Appl. Spectrosc. 2006;60(5):483-489.

102. Jang I, Sung J, Choi H, Chin I. Synthesis and characterization of TiO2/polystyrene hybrid nanoparticles via admicellar polymerization. Journal of Materials Science 2005;40(11):3021-3024.

103. Edwards HGM, Brown DR, Dale JA, Plant S. Raman spectroscopy of sulfonated polystyrene resins. Vibrational Spectroscopy 2000;24(2):213-224.

104. Gachet D, Billard F, Sandeau N, Rigneault H. Coherent anti-Stokes Raman scattering (CARS) microscopy imaging at interfaces: evidence of interference effects. Opt. Express 2007;15(16):10408-10420.

105. Cheng J-X, Jia YK, Zheng G, Xie XS. Laser-Scanning Coherent Anti-Stokes Raman Scattering Microscopy and Applications to Cell Biology. Biophysical Journal 2002;83(1):502-509.

106. Zhang W, Parsons M, McConnell G. Flexible and stable optical parametric oscillator based laser system for coherent anti-Stokes Raman scattering microscopy. Microscopy Research and Technique 2009;9999(9999):NA.

107. Schie IW, Weeks T, McNerney GP, Fore S, Sampson JK, Wachsmann-Hogiu S, Rutledge JC, Huser T. Simultaneous forward and epi-CARS microscopy with a single detector by timecorrelated single photon counting. Opt. Express 2008;16(3):2168-2175.

108. Wang H, Huff TB, Cheng J-X. Coherent anti-Stokes Raman scattering imaging with a laser source delivered by a photonic crystal fiber. Opt. Lett. 2006;31(10):1417-1419.

109. Le TT, Yue S, Cheng J-X. Shedding new light on lipid biology with coherent anti-Stokes Raman scattering microscopy. Journal of Lipid Research 2010;51(11):3091-3102.

110. Hellerer T, Axang C, Brackmann C, Hillertz P, Pilon M, Enejder A. Monitoring of lipid storage in Caenorhabditis elegans using coherent anti-Stokes Raman scattering (CARS) microscopy. Proc Natl Acad Sci U S A 2007;104(37):14658-63.

111. Choudhury RP, Fuster V, Fayad ZA. Molecular, cellular and functional imaging of atherothrombosis. Nat Rev Drug Discov 2004;3(11):913-25.

112. Lim RS, Kratzer A, Barry NP, Miyazaki-Anzai S, Miyazaki M, Mantulin WW, Levi M, Potma EO, Tromberg BJ. Multimodal CARS microscopy determination of the impact of diet on macrophage infiltration and lipid accumulation on plaque formation in ApoE-deficient mice. J Lipid Res 2010;51(7):1729-37.

113. Le TT, Langohr IM, Locker MJ, Sturek M, Cheng JX. Label-free molecular imaging of atherosclerotic lesions using multimodal nonlinear optical microscopy. Journal of Biomedical Optics 2007;12(5):054007.

114. Kim SH, Lee ES, Lee JY, Lee BS, Park JE, Moon DW. Multiplex coherent anti-stokes Raman spectroscopy images intact atheromatous lesions and concomitantly identifies distinct chemical profiles of atherosclerotic lipids. Circ Res 2010;106(8):1332-41.

115. Robinson I, Ochsenkuhn MA, Campbell CJ, Giraud G, Hossack WJ, Arlt J, Crain J. Intracellular imaging of host-pathogen interactions using combined CARS and two-photon fluorescence microscopies. Journal of Biophotonics 2010;3(3):138-146.

116. Nan X, Potma EO, Xie XS. Nonperturbative chemical imaging of organelle transport in living cells with coherent anti-stokes Raman scattering microscopy. Biophys J 2006;91(2):728-35.

117. Pliss A, Kuzmin AN, Kachynski AV, Prasad PN. Biophotonic probing of macromolecular transformations during apoptosis. Proc Natl Acad Sci U S A 2010;107(29):12771-6.

118. Cross SE, Innes B, Roberts MS, Tsuzuki T, Robertson TA, McCormick P. Human skin penetration of sunscreen nanoparticles: In-vitro assessment of a novel micronized zinc oxide formulation. Skin Pharmacology and Physiology 2007;20(3):148-154.

119. Estrin Y, Khaydarov R, Khaydarov RA, Scheper T, Endres C, Cho SY. Antimicrobial and antibacterial effects of silver nanoparticles synthesized by novel electrochemical method. 2008 International Conference on Nanoscience and Nanotechnology 2008:44-47.

120. Ammann M, Burtscher H. Characterization of Ultrafine Aerosol-Particles in Mt-Etna Emissions. Bulletin of Volcanology 1990;52(8):577-583.

121. Kittelson DB. Engines and nanoparticles: A review. Journal of Aerosol Science 1998;29(5-6):575-588.

122. Bystrzejewska-Piotrowska G, Golimowski J, Urban PL. Nanoparticles: Their potential toxicity, waste and environmental management. Waste Management 2009;29(9):2587-2595.

123. Priest S, Greenhalgh T, Kramer V. Risk perceptions starting to shift? US citizens are forming opinions about nanotechnology. Journal of Nanoparticle Research 2010;12(1):11-20.

124. Nel A, Xia T, Madler L, Li N. Toxic potential of materials at the nanolevel. Science 2006;311(5761):622-627.

125. Bermudez E, Mangum JB, Wong BA, Asgharian B, Hext PM, Warheit DB, Everitt JI. Pulmonary responses of mice, rats, and hamsters to subchronic inhalation of ultrafine titanium dioxide particles. Toxicological Sciences 2004;77(2):347-357.

126. Ward JE, Kach DJ. Marine aggregates facilitate ingestion of nanoparticles by suspension-feeding bivalves. Marine Environmental Research 2009;68(3):137-142.

127. Al-Jamal WT, Al-Jamal KT, Cakebread A, Halket JM, Kostarelos K. Blood Circulation and Tissue Biodistribution of Lipid-Quantum Dot (L-QD) Hybrid Vesicles Intravenously Administered in Mice. Bioconjugate Chemistry 2009;20(9):1696-1702.

128. Oberdorster G, Stone V, Donaldson K. Toxicology of nanoparticles: A historical perspective. Nanotoxicology 2007;1(1):2-25.

129. Unfried K, Albrecht C, Klotz LO, Von Mikecz A, Grether-Beck S, Schins RPF. Cellular responses to nanoparticles: Target structures and mechanisms. Nanotoxicology 2007;1(1):52-71.

130. Rago G, Langer CM, Brackman C, Day JP, Domke KF, Raschzok N, Schmidt C, Sauer IM, Enejder A, Mogl MT and others. CARS microscopy for the visualization of micrometer-sized iron oxide MRI contrast agents in living cells. Biomed Opt Express 2011;2(9):2470-83.

131. Zheng YG, Holtom G, Colson S. Multichannel multiphoton imaging of metal oxides nanoparticles in biological system. Multiphoton Microscopy in the Biomedical Sciences Iv 2004;5323:390-399.

132. Moger J, Johnston BD, Tyler CR. Imaging metal oxide nanoparticles in biological structures with CARS microscopy. Opt. Express 2008;16(5):3408-3419.

133. Garrett N, Whiteman M, Moger J. Imaging the uptake of gold nanoshells in live cells using plasmon resonance enhanced four wave mixing microscopy. Opt Express 2011;19(18):17563-74.

134. Rago G, Bauer B, Svedberg F, Gunnarsson L, Ericson MB, Bonn M, Enejder A. Uptake of gold nanoparticles in healthy and tumor cells visualized by nonlinear optical microscopy. J Phys Chem B 2011;115(17):5008-16.

135. Kilgour A, Elfick A. Influence of crosslinked polyethylene structure on wear of joint replacements. Tribology International 2009;42(11-12):1582-1594.

136. Downes A, Mouras R, Elfick A. A versatile CARS microscope for biological imaging. Journal of Raman Spectroscopy 2009;40(7):757-762.

137. Prokhorov KA, Nikolaeva GY, Gordeyev SA, Pashinin PP, Nikolaev DP. Raman scattering in oriented polyethylene: The C-H stretching region. Laser Physics 2001;11(1):86-93.

138. Chen JS, Lau SP, Sun Z, Tay BK, Yu GQ, Zhu FY, Zhu DZ, Xu HJ. Structural and mechanical properties of nitrogen ion implanted ultra high molecular weight polyethylene. Surface & Coatings Technology 2001;138(1):33-38.

139. Fujita K, Kimura M. Band shapes of Fermi resonance spectra. Molecular Physics 1980;41(5):1203-1210.

140. Kobayashi M, Tadokoro H, Porter RS. Polarized Raman spectra of n?alkane single crystals with orthorhombic polyethylene?journal article sublattice: AIP; 1980. 3635-3642 p.

141. Lu S, Russell AE, Hendra PJ. The Raman spectra of high modulus polyethylene fibres by Raman microscopy. Journal of Materials Science 1998;33(19):4721-4725.

142. Yamakoshi H, Dodo K, Okada M, Ando J, Palonpon A, Fujita K, Kawata S, Sodeoka M. Imaging of EdU, an Alkyne-Tagged Cell Proliferation Probe, by Raman Microscopy. Journal of the American Chemical Society 2011;133(16):6102-6105.

143. Reynolds NM, Hsu SL. A normal vibrational analysis of syndiotactic polystyrene. Macromolecules 1990;23(14):3463-3472.

144. Reynolds NM, Savage JD, Hsu SL. A spectroscopic study of syndiotactic polystyrene. Macromolecules 1989;22(6):2867-2869.

145. Sears WM, Hunt JL, Stevens JR. Raman scattering from polymerizing styrene. I. Vibrational mode analysis. The Journal of Chemical Physics 1981;75(4):1589-1598.

146. Thomas KJ, et al. Raman spectra of polymethyl methacrylate optical fibres excited by a 532 nm diode pumped solid state laser. Journal of Optics A: Pure and Applied Optics 2008;10(5):055303.

147. Ren Y, Matsushita A, Matsukawa K, Inoue H, Minami Y, Noda I, Ozaki Y. Two-dimensional Fourier-transform-Raman and near-infrared correlation spectroscopy studies of poly(methyl methacrylate) blends: 2. Partially miscible blends of poly(methyl methacrylate) and poly(4-vinylphenol). Vibrational Spectroscopy 2000;23(2):207-218.

148. Bicknell-Brown E, Brown KG, Person WB. Configuration-dependent Raman bands of phospholipid surfaces. 1. Carbonyl stretching modes at the bilayer interface. Journal of the American Chemical Society 1980;102(17):5486-5491.

149. Bicknell-Brown E, Brown KG, Person WB. Configuration-dependent Raman bands of phospholipid surfaces: 2—Head group and acyl stretching modes in the 800–900 cm−1 region. Journal of Raman Spectroscopy 1981;11(5):356-362.

150. Lee C, Bain CD. Raman spectra of planar supported lipid bilayers. Biochimica et Biophysica Acta (BBA) - Biomembranes 2005;1711(1):59-71.

151. Guo JD, Zerda TW. Raman Study on Effects of High Pressure on the Structure of DPPC−Cholesterol Multilamellar Vesicles. The Journal of Physical Chemistry B 1997;101(28):5490-5496.

152. Lippert JL, Lindsay RM, Schultz R. Laser Raman Characterization of Conformational-Changes in Sarcoplasmic-Reticulum Induced by Temperature, Ca-2+, and Mg-2+. Journal of Biological Chemistry 1981;256(23):2411-2416.

153. Otto C, Vandentweel TJJ, Demul FFM, Greve J. Surface-Enhanced Raman-Spectroscopy of DNA Bases. Journal of Raman Spectroscopy 1986;17(3):289-298.

154. Maiti NC, Apetri MM, Zagorski MG, Carey PR, Anderson VE. Raman Spectroscopic Characterization of Secondary Structure in Natively Unfolded Proteins: α-Synuclein. Journal of the American Chemical Society 2004;126(8):2399-2408.

155. Chi Z, Chen XG, Holtz JSW, Asher SA. UV Resonance Raman-Selective Amide Vibrational Enhancement: Quantitative Methodology for Determining Protein Secondary Structure†. Biochemistry 1998;37(9):2854-2864.

156. Levitt M, Greer J. Automatic identification of secondary structure in globular proteins. Journal of Molecular Biology 1977;114(2):181-239.

157. Gorga JC, Dong AC, Manning MC, Woody RW, Caughey WS, Strominger JL. Comparison of the Secondary Structures of Human Class-I and Class-Ii Major Histocompatibility Complex Antigens by Fourier-Transform Infrared and Circular-Dichroism Spectroscopy. Proceedings of the National Academy of Sciences of the United States of America 1989;86(7):2321-2325.

158. Ramakrishnan V, Rajkumar BJM. Infrared and laser Raman studies of L-phenylalanine L-phenylalaninium perchlorate and bis(DL-phenylalaninium) sulphate monohydrate. Spectrochimica Acta Part a-Molecular and Biomolecular Spectroscopy 2002;58(9):1923-1934.

159. Bolton BA, Scherer JR. Raman spectra and water absorption of bovine serum albumin. The Journal of Physical Chemistry 1989;93(22):7635-7640.

160. Hopwood D. Theoretical and Practical Aspects of Glutaraldehyde Fixation. Histochemical Journal 1972;4(4):267-&.

161. Dougherty GJ, McBride WH. Macrophage heterogeneity. J Clin Lab Immunol 1984;14(1):1-11.

162. Erfurth SC, Kiser EJ, Peticolas WL. Determination of the Backbone Structure of Nucleic Acids and Nucleic Acid Oligomers by Laser Raman Scattering. Proceedings of the National Academy of Sciences of the United States of America 1972;69(4):938-941.

163. Garrett NL, Lalatsa A, Begley D, Mihoreanu L, Uchegbu IF, Schotzlein AG, Moger J. Label-free imaging of polymeric nanomedicines using coherent anti-stokes Raman scattering microscopy. Journal of Raman Spectroscopy 2012;43(5):681-688.

164. Latex beads, polystyrene, 1.1 μm mean particle size specification sheet. Volume 2011; 2011.

165. Kilgour A, Elfick A. Design and test of novel tribometer: investigation into wear performance of materials used in total hip replacements. Tribology - Materials, Surfaces & Interfaces 2008;2(3):161-168.

166. Monici M. Cell and tissue autofluorescence research and diagnostic applications. Biotechnol Annu Rev 2005;11:227-56.

167. Patterson GH, Piston DW. Photobleaching in two-photon excitation microscopy. Biophys J 2000;78(4):2159-62.

168. Serrels A, Timpson P, Canel M, Schwarz JP, Carragher NO, Frame MC, Brunton VG, Anderson KI. Real-time study of E-cadherin and membrane dynamics in living animals: implications for disease modeling and drug development. Cancer Res 2009;69(7):2714-9.

169. Linsebigler AL, Lu GQ, Yates JT. Photocatalysis on Tio2 Surfaces - Principles, Mechanisms, and Selected Results. Chemical Reviews 1995;95(3):735-758.

170. Hamamatsu Photonics K.K. ETD. Photomultiplier Tube R3896. Volume 2011. Iwata City; 2006.

171. Vogel A, Noack J, Mittmann G, Paltauf G. Femtosecond-laser-produced low-density plasmas in transparent biological media: A tool for the creation of chemical, thermal and thermomechanical effects below the optical breakdown threshold. Commercial and Biomedical Applications of Ultrafast and Free-Electron Lasers 2002;4633:23-37.

172. Fu Y, Wang HF, Shi RY, Cheng JX. Characterization of photodamage in coherent anti-Stokes Raman scattering microscopy. Optics Express 2006;14(9):3942-3951.

173. Volkmer A. Vibrational imaging and microspectroscopies based on coherent anti-Stokes Raman scattering microscopy. Journal of Physics D-Applied Physics 2005;38(5):R59-R81.

174. Kodaira Y, Kusumoto T, Takahashi T, Matsumura Y, Miyagi Y, Okamoto K, Shidoji Y, Sagami H. Formation of lipid droplets induced by 2,3-

dihydrogeranylgeranoic acid distinct from geranylgeranoic acid. Acta Biochim Pol 2007;54(4):777-82.

175. Hirotani H, Tuohy NA, Woo JT, Stern PH, Clipstone NA. The calcineurin/nuclear factor of activated T cells signaling pathway regulates osteoclastogenesis in RAW264.7 cells. J Biol Chem 2004;279(14):13984-92.

176. Moger J, Johnston BD, Tyler CR. Imaging metal oxide nanoparticles in biological structures with CARS microscopy. Opt Express 2008;16(5):3408-19.

177. Matthews JB, Green TR, Stone MH, Wroblewski BM, Fisher J, Ingham E. Comparison of the response of three human monocytic cell lines to challenge with polyethylene particles of known size and dose. J Mater Sci Mater Med 2001;12(3):249-58.

178. Lee M, Elfick A. Imaging prosthetic implant related wear debris in macrophages using coherent anti-Stokes Raman scattering spectroscopy. Proceedings of SPIE 2011;8087(80872S).

179. Difato F, Mazzone F, Scaglione S, Fato M, Beltrame F, Kubinova L, Janacek J, Ramoino P, Vicidomini G, Diaspro A. Improvement in volume estimation from confocal sections after image deconvolution. Microscopy Research and Technique 2004;64(2):151-155.

180. Saar BG, Johnston RS, Freudiger CW, Xie XS, Seibel EJ. Coherent Raman scanning fiber endoscopy. Opt Lett 2011;36(13):2396-8.

181. Wang ZY, Yang YL, Luo PF, Gao LA, Wong KK, Wong STC. Delivery of picosecond lasers in multimode fibers for coherent anti-Stokes Raman scattering imaging. Optics Express 2010;18(12):13017-13028.

182. Tipper JL, Galvin AL, Williams S, McEwen HM, Stone MH, Ingham E, Fisher J. Isolation and characterization of UHMWPE wear particles down to ten nanometers in size from in vitro hip and knee joint simulators. Journal of Biomedical Materials Research. Part A 2006;78(3):473-80.

183. Satterfield MB, Salit ML, Choquette SJ. Use of Standard Reference Material 2242 (Relative Intensity Correction Standard for Raman Spectroscopy) for microarray scanner qualification. Biotechniques 2008;45(2):143-+.

184. Rodriguez JD, Westenberger BJ, Buhse LF, Kauffman JF. Standardization of Raman spectra for transfer of spectral libraries across different instruments. Analyst 2011;136(20):4232-4240.

185. Mansfield J, Yu J, Attenburrow D, Moger J, Tirlapur U, Urban J, Cui Z, Winlove P. The elastin network: its relationship with collagen and cells in articular cartilage as visualized by multiphoton microscopy. J Anat 2009;215(6):682-91.

186. Mansfield JC, Winlove CP, Moger J, Matcher SJ. Collagen fiber arrangement in normal and diseased cartilage studied by polarization sensitive nonlinear microscopy. Journal of Biomedical Optics 2008;13(4):044020.

187. Bianchini P, Diaspro A. Three-dimensional (3D) backward and forward second harmonic generation (SHG) microscopy of biological tissues. Journal of Biophotonics 2008;1(6):443-450.

188. Campagnola PJ, Millard AC, Terasaki M, Hoppe PE, Malone CJ, Mohler WA. Three-dimensional high-resolution second-harmonic generation imaging of endogenous structural proteins in biological tissues. Biophys J 2002;82(1 Pt 1):493-508.

189. Diaspro A, Chirico G, Collini M. Two-photon fluorescence excitation and related techniques in biological microscopy. Quarterly Reviews of Biophysics 2005;38(2):97-166.

190. Kohl T, Schwille P. Fluorescence correlation spectroscopy with autofluorescent proteins. Microscopy Techniques 2005;95:107-142.

191. Tong L, Lu Y, Lee RJ, Cheng JX. Imaging receptor-mediated endocytosis with a polymeric nanoparticle-based coherent anti-stokes raman scattering probe. Journal of Physical Chemistry B 2007;111(33):9980-9985.

192. Xu PS, Gullotti E, Tong L, Highley CB, Errabelli DR, Hasan T, Cheng JX, Kohane DS, Yeo Y. Intracellular Drug Delivery by Poly(lactic-co-glycolic acid) Nanoparticles, Revisited. Molecular Pharmaceutics 2009;6(1):190-201.

193. Karlsson HL, Cronholm P, Gustafsson J, Moller L. Copper oxide nanoparticles are highly toxic: A comparison between metal oxide nanoparticles and carbon nanotubes. Chemical Research in Toxicology 2008;21(9):1726-1732.

194. Jorio A, Souza AG, Dresselhaus G, Dresselhaus MS, Swan AK, Unlu MS, Goldberg BB, Pimenta MA, Hafner JH, Lieber CM and others. G-band resonant Raman study of 62 isolated single-wall carbon nanotubes. Physical Review B 2002;65(15).

195. Freudiger CW, Min W, Saar BG, Lu S, Holtom GR, He CW, Tsai JC, Kang JX, Xie XS. Label-Free Biomedical Imaging with High Sensitivity by Stimulated Raman Scattering Microscopy. Science 2008;322(5909):1857-1861.

196. Zhang X, Roeffaers MBJ, Basu S, Daniele JR, Fu D, Freudiger CW, Holtom GR, Xie XS. Label-Free Live-Cell Imaging of Nucleic Acids Using Stimulated Raman Scattering Microscopy. ChemPhysChem 2012;13(4):1054-1059.

197. Saar BG, Contreras-Rojas LR, Xie XS, Guy RH. Imaging Drug Delivery to Skin with Stimulated Raman Scattering Microscopy. Molecular Pharmaceutics 2011;8(3):969-975.